Metallic Thermoelectric Materials for Active Cooling Application

---

A

Dissertation

Presented to

the faculty of the School of Engineering and Applied Science

University of Virginia

---

in partial fulfillment

of the requirements for the degree

Doctor of Philosophy

by

Shuai Li

December 2024

APPROVAL SHEET

This

Dissertation

is submitted in partial fulfillment of the requirements
for the degree of

Doctor of Philosophy

Author: Shuai Li

This Dissertation has been read and approved by the examing committee:

Advisor: Mona Zebarjadi

Advisor:

Committee Member: Jerry A. Floro

Committee Member: Ji Ma

Committee Member: Joseph Poon

Committee Member: Keivan Esfarjani

Committee Member: Petra Reinke

Committee Member:

Accepted for the School of Engineering and Applied Science:

Jennifer L. West, School of Engineering and Applied Science

December 2024

Abstract

Thermal management is crucial for high-performance integrated circuits (ICs) and Li-ion battery (LIB) powered vehicles. Active thermoelectric (Peltier) cooling and passive (conductive) cooling can be combined to design active heat sinks with high effective thermal conductivity (κ_{eff}). To achieve high κ_{eff}, both a high power factor (PF) and high passive thermal conductivity are desired. This makes traditional semiconducting thermoelectric (TE) materials, which typically have low thermal conductivity, poor candidates. The proposed work examines the potential of metallic materials for active cooling applications based on their intrinsic high electrical and thermal conductivity. Here, we study selected candidates from two classes of metallic materials: metallic binary alloys and intermetallic f-orbital compounds. Binary alloys with high Seebeck coefficients, such as Cu-Ni, Ni-Fe, and Cr-Mn, are investigated with the goal of achieving high κ_{eff}. The potential of low-cost copper-nickel alloys for active cooling applications is explored, in combination with directed energy deposition additive manufacturing, which enables the production of complex geometries and large-scale manufacturing. Nickel-iron alloys with both high power factor and high κ_{eff} are also studied, and compositions with peak PF and κ_{eff} are examined, accompanied by microstructural analysis. Further trials are conducted on thermoelectrically unexplored binary systems, such as Co-Sn, Co-Al, and Ni-Sn. Additionally, Yb-based intermetallic compounds are screened based on first-principles calculations of the density of states. $YbZn_{11}$ is investigated for the first time for its thermoelectric properties and doped to improve TE performance. Other Yb-based intermetallic compounds, including Yb-Ag and Yb-Zn, are also explored. We believe our studies will expand current understanding of the thermoelectric performance of metallic

materials and their applications in active cooling systems, shedding light on innovative approaches for more efficient cooling solutions and addressing the thermal management challenges in real-world applications.

Acknowledgement

First and foremost, I would like to express my deepest gratitude to my advisor, Professor Mona Zebarjadi, for her invaluable guidance, encouragement, and unwavering support throughout my doctoral journey. Her expertise and mentorship have been instrumental in shaping both my research and academic growth.

I am profoundly thankful to my committee members for their valuable contributions and insights. Professor Jerry Floro provided invaluable advice and opportunities for collaboration, which enriched many of my projects. Professor Joseph Poon offered thoughtful guidance and collaborations that significantly enhanced the scope of my work. I am also deeply grateful to Professor Ji Ma and Professor Petra Reinke for their constructive advice and feedback during my research. Additionally, I extend my sincere thanks to Professor Keivan Esfarjani for his guidance on first-principles calculation work related to my research.

I would like to acknowledge the collaboration and support of Professor Zhifeng Ren from the University of Houston, whose input greatly strengthened my studies. Special thanks are also due to Dr. Joshi Giri for his collaborative efforts and valuable guidance.

I am immensely grateful to my peers and colleagues, who made this journey both productive and memorable. My heartfelt thanks go to Tianhui Zhu, Md Sabbir Akhanda, and Emad Rezaei, who guided and supported me during the early stages of my Ph.D. program. Special thanks to Naiming Liu for providing invaluable advice on both academia and career development. I also want to acknowledge Haobo Wang for his camaraderie, collaboration, and insightful discussions.

Additionally, I deeply appreciate the help and encouragement of Md Golam Rosul, Farjana F. Tonni, Sree Sourav Das, Bati Sujit, Yunhui Wu, Mousumi Mitra, Kyle Snyder, Shi Xin, Shaowei Song, Xixiao Hu, and Ruhul Quddus throughout my journey. Many thanks to Diane Dickie, Helge Heinrich, Joseph A. Thompson, and Richard R. White at NMCF for their exceptional training and support with characterizations.

This work would not have been possible without the financial support provided by the National Science Foundation (NSF) and the Department of Energy (DOE), whose funding made this research feasible and impactful.

Finally, I want to express my heartfelt gratitude to my family and friends for their unwavering encouragement and support throughout this challenging yet rewarding journey. My parents, Yong Li and Guizhi Huang, deserve the highest praise for their endurance, vision, and compassion in raising the first-generation university student, the first master's degree holder, and, now, the first Doctor of Philosophy in our family. I am also deeply thankful to my grandparents, who shaped me into the person I am today. To my girlfriend, Jiayi Luo, I express my sincere love and gratitude for bringing light into my life during the toughest times. Lastly, to all my friends who have brought me happiness and comfort over the years, thank you.

List of Figures

List of Terms and Symbols

TE: Thermoelectric

S: Seebeck coefficient, thermopower

T: Temperature

∇T: Temperature gradient

ΔT: Temperature difference

Q_P: Peltier heat

I: Current

π: Peltier coefficient

$\tau_{Thomson}$: Thomson coefficient

Z: Thermoelectric figure of merit

σ: Electrical conductivity

σS^2,PF: Power factor

κ, κ_{total}: Thermal conductivity

κ_L: Lattice thermal conductivity

κ_e: electron thermal conductivity

COP: coefficient of performance

T_c: Cold end temperature

T_h : Hot end temperature

η: thermoelectric efficiency

n: carrier concentration

e: charge of electron

μ: carrier mobility

m^*: effective mass of the carrier

τ: carrier relaxation time

k: wave vector

$\hbar$: Reduced Plank's constant

h: Plank's constant

k_B: Boltzmann constant

DOS: density of states of the carriers

E_F: Fermi energy

L: Lorenz factor

PGEC: Phonon-glass electron-crystal

K: Passive thermal conductance

R: Electrical resistance

ρ: Density

κ_{eff}: Effective thermal conductivity

LIB: Lithium-ion battery

IC: Integrated circuit

DED: Directed Energy Deposition

AM: Additive Manufacturing

BM: Ball-milled

HP: Hot-pressed

XRD: X-ray diffraction

SEM: Scanning electron microscopy

BSE: Backscattered electrons

EDS: Energy-dispersive X-ray spectroscopy

C_p : Heat capacity at constant pressure

α: Thermal diffusivity

RT: Room temperature

CCAM : the Commonwealth Center for Advanced Manufacturing

TTO: Thermal Transport Option

DFT: Density functional theory

SOC: Spin-orbit coupling

EBSD: Electron backscattered diffraction

Table of Contents

1. Introduction

1.1 Thermoelectric Effects

The thermoelectric effect is the foundation of thermoelectricity, characterized by the generation of an electric voltage when a temperature gradient is applied across a conductive material. Three primary thermoelectric effects describe this phenomenon:

Seebeck Effect: The Seebeck effect, discovered by Thomas Johann Seebeck in 1821, describes the generation of an electromotive force (EMF) in a closed circuit when there is a temperature difference between two different materials or junctions. This effect is quantified by the Seebeck coefficient (S), which is a material-specific property and relates the EMF (E) to the temperature gradient (∇T) across the material:

$$E = -S\nabla T \qquad (1-1)$$

The negative sign signifies that the direction of the electric current induced by the Seebeck effect depends on the temperature gradient.

Peltier Effect: The Peltier effect, first observed by Jean-Charles Peltier in 1834, is the reverse of the Seebeck effect. It describes the absorption or release of heat when an electric current flows through the junction of two dissimilar materials. The Peltier heat (Q_P) is proportional to the current (I) passing through the junction and the Peltier coefficient (π):

$$Q_P = \pi I \qquad (1-2)$$

The Peltier coefficient (π) is related to the Seebeck coefficient (S) and the electrical conductivity (σ) of the material:

$$\pi = ST \qquad (1-3)$$

Thomson Effect: The Thomson effect, or the thermoelectric heating/cooling effect, describes the heat exchange that occurs when a current flows through a conductor experiencing a temperature gradient. The Thomson coefficient (τ) characterizes this effect. The heat (Q_T) generated or absorbed is given by:

$$Q_T = -\tau_{Thomson} I \nabla T \quad (1-4)$$

The Thomson coefficient (τ) is related to the material's Seebeck coefficient (S)

$$\tau_{Thomson} = T dS/dT \quad (1-5)$$

These thermoelectric effects are the cornerstone of thermoelectric devices. The Seebeck effect enables the conversion of temperature differences into electrical voltage, the Peltier effect provides the basis for thermoelectric cooling, and the Thomson effect plays a role in the temperature change associated with current flow in conductors experiencing a thermal gradient. Understanding and optimizing these effects in thermoelectric materials are essential for improving the efficiency of thermoelectric devices and systems.

1.2 Thermoelectric Module and Device

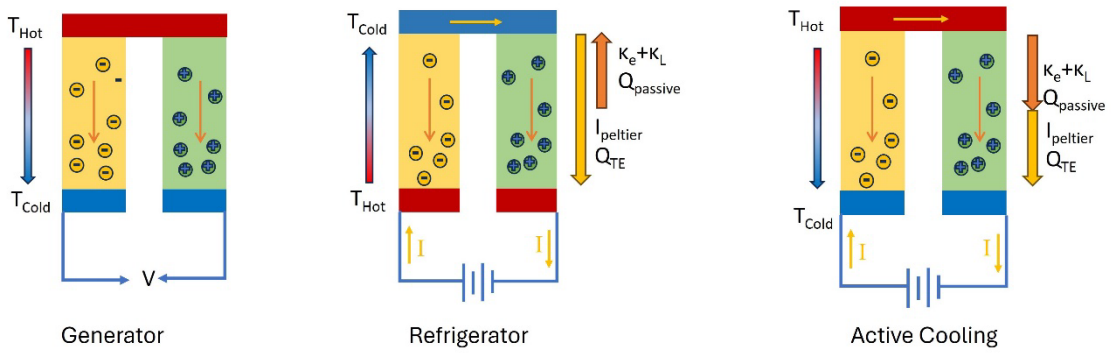

Figure 1-1 Thermoelectric module working in different modes

In Figure 1-1, a single thermoelectric module is shown. It typically consists of a pair of thermoelectric couples, each with a p-type and n-type leg. These legs are electrically

connected in series and thermally in parallel. Depending on the temperature gradient and the applied current or voltage configuration, the same thermoelectric module can operate in different modes. In generator mode, a temperature difference across the module is converted into an electrical voltage. In refrigerator mode, an applied current drives heat current from the cold side to the hot side against the natural heat flux, enabling cooling. In thermoelectric (or active cooling) mode, an applied current drives heat current from the cold side to the hot side against the natural heat flux

1.3 Thermal Management Challenges

The thermal management dilemma poses substantial challenges in two pivotal technological domains: integrated circuits (ICs) and electric vehicles (EVs). In the integrated circuits industry, the enduring validity of Moore's law has propelled the rapid increase in transistor or device density within chips. This surge is attributed to advancements in sub-10nm semiconductor manufacturing processes, the constant demand for enhanced computing power, and the ongoing miniaturization of electronics, as depicted

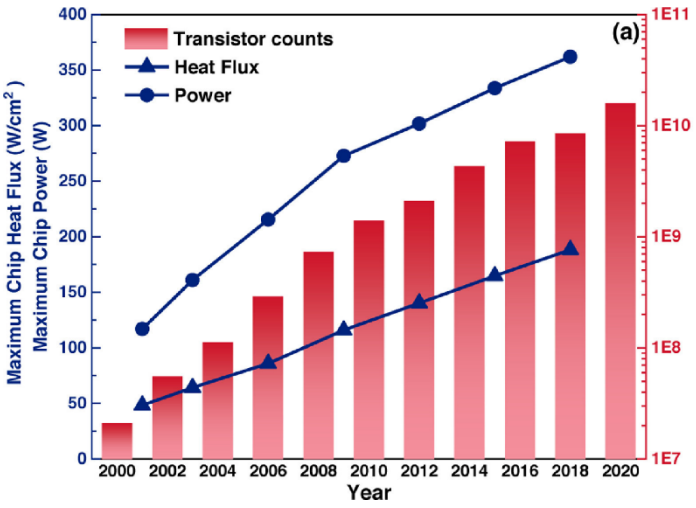

Figure 1-2 Chip maximum heat flux, power, and transistor counts versus years 2000-2020 [1]

in Fig.1. The densely packed high-frequency devices within confined spaces result in a significant elevation in power density and heat flux density. Failure to expeditiously dissipate this heat can lead to increased temperatures, subsequently compromising the reliability and performance of electronic devices.[1,2] The imperative need for effective thermal management methodologies in this context is both evident and urgent.

In the case of Li-ion batteries (LIBs), stringent temperature control is paramount, ideally within the range of 15~35°C.[3] However, the operational and charging processes of LIBs inherently generate heat. In the absence of efficient thermal management, escalating temperatures can expedite degradation, potentially culminating in a catastrophic thermal runaway.[4] As global initiatives dictate the phased discontinuation of conventional vehicles, ensuring the optimal performance and reliability of LIB-driven vehicles becomes an urgent concern.

Conventional heat dissipation methods such as passive heat sinks and water- or air-cooling exhibit limitations in aspects such as size, effectiveness, and maintenance requirements when addressing the thermal management challenges of ICs and LIBs. Addressing this new set of challenges necessitates innovative approaches in materials, designs, and methodologies.

1.4 Figure of Merit

The thermoelectric figure of merit Z is defined as

$$Z = \frac{\sigma S^2}{\kappa} \qquad (1-6)$$

σ is the electrical conductivity with the unit $(\Omega \cdot m)^{-1}$. S is the Seebeck coefficient with the unit V/K. κ is the total thermal conductivity with the unit W/m·K. The figure of merit Z

has the dimensional units of T^{-1}. When multiplied by the absolute temperature T, ZT becomes a dimensionless parameter and is usually used to evaluate the temperature-related performance of thermoelectrics. The coefficient of performance (COP) of a thermoelectric refrigerator can be expressed as.

$$COP = \frac{T_c\sqrt{1+\frac{1}{2}Z(T_h+T_c)} - T_h}{(T_h - T_c)\left(\sqrt{1+\frac{1}{2}Z(T_h+T_c)}+1\right)} \qquad (1-7)$$

where Th stands for the temperature of the hot end of the device while Tc is the cold end temperature. Similarly, for thermoelectric generators, the maximum efficiency can be defined as [5]

$$\eta = \frac{(T_h - T_c)\left(\sqrt{1+\frac{1}{2}Z(T_h+T_c)}-1\right)}{T_h\sqrt{1+\frac{1}{2}Z(T_h+T_c)}+T_c} \qquad (1-8)$$

To simplify the expressions. Let

$$\gamma = \sqrt{1+\frac{1}{2}Z(T_h+T_c)} \qquad (1-9)$$

$$\Delta T = (T_h - T_c) \qquad (1-10)$$

Then (1-7) and (1-8) becomes.

$$COP = \frac{T_c\gamma - T_h}{\Delta T(\gamma+1)} \qquad (1-11)$$

$$\eta = \frac{\Delta T(\gamma-1)}{T_h\gamma + T_c} \qquad (1-12)$$

Both efficiency and COP increase when the figure of merit increases, assuming the temperature distribution stays the same. The figure of merit Z can be enhanced in two ways, by increasing the power factor, σS^2, or lowering the total thermal conductivity, κ. The total

thermal conductivity κ is composed of two parts, κ_e , the charge-carrier thermal conductivity, and the lattice thermal conductivity, κ_L. While κ_L can be tuned separately, the three parameters, S, σ, and κ_e, are interdependent and related to the electronic band structure of the materials.

1.5 Thermoelectric Transport Parameters

According to equation (6), the parameters that determine the figure of merit ZT are: electrical conductivity σ, Seebeck coefficient (thermopower) S, and thermal conductivity κ.

Within the Drude model, the conductivity is defined as

$$\sigma = ne\mu \qquad (1-13)$$

Where n is the carrier concentration, e is the charge of electron (1.6×10^{-29} C), μ is the carrier mobility. The carrier concentration n depends on bandgap, doping level, band structure, and temperature.

Within constant relaxation time approximation, carrier mobility of a single band is

$$\mu = \frac{q\tau}{m^*} \qquad (1-14)$$

Where m^* is the effective mass of the carrier, τ is the carrier relaxation time. m^* depends on the band structure curvature.

Within a parabolic band structure model, effective mass can be obtained from the curvature of E-k relation

$$\frac{1}{m^*} = \frac{1}{\hbar^2}\left(\frac{d^2E}{dk^2}\right) \qquad (1-15)$$

Where k is the wave vector, $\hbar$ is the reduced Plank constant, E is the energy.

τ is influenced by scattering processes of carriers by many factors including defects and impurities, lattice vibration(phonon), and strains.

An approximate formula of Seebeck coefficient S can be derived from the Mott relation basing on the same assumption of degeneracy, single band conduction and energy independent of mobility.[6]

$$S = -\frac{\pi^2 {k_B}^2 T}{3e}\left[\frac{dln(DOS(E))}{dE}\right]\Bigg|_{E=E_F} \qquad (1-16)$$

Where $DOS(E)$ is the energy-dependent density of states of the carriers, and E_F is the fermi level. Equation (1-16) clearly shows the larger the density of states (DOS) near the fermi level, the higher the |S|. This guideline is also used in the following chapters.

For degenerate semiconductors and metals, assuming parabolic band, constant relaxation time approximation, and energy independent of mobility, equation (1-16) can be further simplified. Seebeck can be expressed as

$$S = \frac{8\pi^2 {k_B}^2}{3eh^2} m^* \left(\frac{\pi}{3n}\right)^{-\frac{2}{3}} \qquad (1-17)$$

Where h is the Plank constant, k_B is the Boltzmann constant. Combining equation (1-13) to (1-15), (1-17), and (1-6), a compromise must be made to tune the coupled Seebeck coefficient S and electrical conductivity σ for reaching high power factor (PF) in heavily doped degenerate semiconductor, which can be achieved by manipulating the electron

transport and band structure of the materials. The optimization of thermoelectric performance, quantified by the figure of merit ZT, starts from finding the ideal carrier concentration for maximum ZT values, as shown in Figure 1-3.

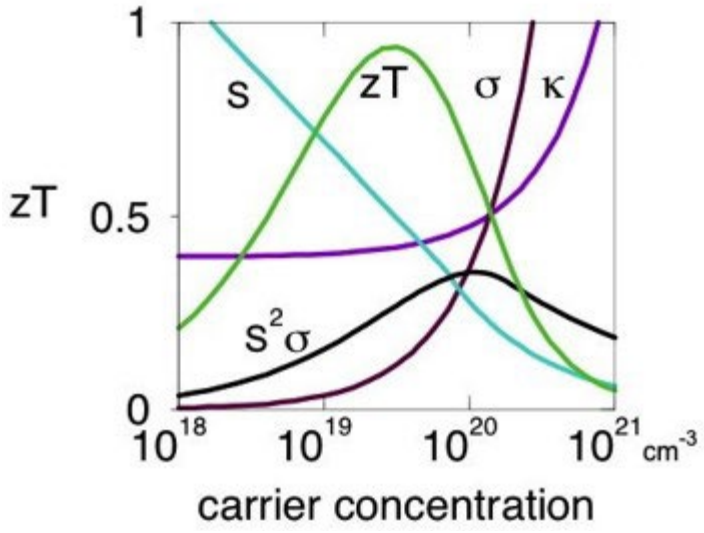

Figure 1-3 transport properties trade-off versus carrier concentration

The total thermal is composed of lattice thermal conductivity κ_L and charge-carrier thermal conductivity κ_e.

$$\kappa_{total} = \kappa_L + \kappa_e \qquad (1-18)$$

The lattice thermal conductivity depends on atomic mass and bond strength, crystal structure, and defect scatterings including point defects, dislocations, grain boundaries, interfaces, and other additional scattering mechanisms. While the charge-carrier thermal conductivity κ_e

$$\kappa_e = \mathrm{L}\sigma T = ne\mu LT \qquad (1-19)$$

Where L is the Lorenz factor, $L=L_0=2.4\times10^{-8}\ J^2K^{-2}C^{-2}$ for metals (i.e. when the Fermi level is deep within the band). For non-degenerate semiconductors with low-carrier concentration, the Lorenz factor is generally smaller than the theoretical value of L_0.

Combining (1-6), (1-19) and (1-18)

$$ZT = \frac{S^2}{L(1+\frac{\kappa_L}{\kappa_e})} \qquad (1-20)$$

shows enhancement can also be achieved by engineering the transport properties. Effective thermoelectrics require a unique "phonon-glass electron-crystal (PGEC)" configuration: a material that scatters phonons to reduce lattice thermal conductivity to approach the minimum lattice thermal conductivity, κ_{min}, like that in glasses, while maintaining a crystalline structure that preserves high electron mobility and suitable effective masses. This ideal combination is introducing mechanisms that scatter phonons effectively without disrupting the electronic structure, leading to a maximized power factor and close-to-minimum lattice thermal conductivity.

The improvement history of the figure of merit of thermoelectrics has been summarized in several articles[7–14] and books[15–17]. With novel strategies such as anharmonicity[18,19], band convergence[7,20–24], phase-transition[25–29], modulation doping[30–32], lattice strain[33–35], and interfacial preferential scattering[36–38], the ZT values above 2 have been reported in Cu_2Se[25,27,39–41], SnSe[34,42–45], Bi_2Te_3/Sb_2Te_3[46], PbTe[35,47], and GeTe[48]. The focus of this dissertation thesis is not on the traditional thermoelectric applications like generators or refrigerators which can be evaluated by ZT. Instead, it is on the under-investigated thermoelectric cooling/active cooling which is discussed in the next section.

1.6 Thermoelectric-based Active Cooling

While thermoelectric power generation and refrigeration both require high figure of merit or ZT value, there is another mode of operation a thermoelectric device can work in. Having been discussed in several papers[5,49,50], this mode utilizes the Peltier current via electron current to help the passive heat transfer via phonons from the hot end to the cold end by consuming electricity actively, therefore being named active cooling. In thermoelectric refrigeration, the active Peltier heat transfer and the passive Fourier heat transfer are in the opposite direction, while in active cooling, the two mechanisms transfer the heat in the same direction. The heat conductance at the hot side of an active thermoelectric cooling module can be expressed as

$$Q_H = SIT_h + \mathrm{K}\Delta T - \frac{RI^2}{2} \qquad (1-21)$$

K is the passive thermal conductance, T_h is the hot source temperature, ΔT is the temperature difference, R is the electrical resistance. The $-\frac{RI^2}{2}$ term is the Joule heating of the current delivered evenly to both ends of the thermoelectric legs. The optimal working current leading to maximum heat flow can be determined by optimization via differentiation.

$$I_{opt} = \frac{ST_h}{R} \qquad (1-22)$$

$$Q_{act,max} = (\mathrm{K} + \frac{(ST_h)^2}{2R\Delta T})\Delta T \qquad (1-23)$$

The concept of effective thermal conductivity, κ_{eff} can be derived from equation (1-23) written in the form of heat flux, which removes the geometrical dependence.[49,50]

$$q_{act,max} = (\kappa + \frac{\sigma S^2 {T_h}^2}{2\Delta T})\Delta T \qquad (1-24)$$

$$\kappa_{eff} = \kappa + \frac{\sigma S^2 {T_h}^2}{2\Delta T} \qquad (1-25)$$

The κ_{eff} includes contributions from the passive thermal conductivity κ and from the Peltier cooling at the optimum applied current $\frac{\sigma S^2 {T_h}^2}{2\Delta T}$. The $\frac{{T_h}^2}{\Delta T}$ part suggests that the active part can increase dramatically with increased hot side temperature and when temperature differences are small. This in turn implies that active cooling is beneficial in transient cases when the device is cooled with a large Peltier heat flux and before a large temperature difference is established. The material-dependent factor is the thermoelectric power factor (PF), σS^2. Here the figure of merit is no longer suitable for evaluating the performance of thermoelectrics for active cooling mode. A high ZT requires maximizing the power factor σS^2 and minimizing the total thermal conductivity, κ, or in other word, phonon-glass electron-crystal. While the effective thermal conductivity κ_{eff} is the summation of κ and active term that is proportional to σS^2. Materials with both high power factor and high thermal conductivity are desired for this application. To optimize the thermoelectric performance for active cooling, an intuitive approach can be proposed: starting from materials with intrinsic high thermal conductivity and tuning the transport parameters to maximize the power factor while keeping the high thermal conductivity.

1.7 Potential of Metallic Materials for Active Cooling

Metallic materials are promising for thermoelectric active cooling due to their inherently high electrical and thermal conductivities, originating from the high concentration of free

electrons n. However, the equation (1-16) and (1-17) also suggest that the fundamental assumptions of ideal metal, 'free electron sea' naturally leads to the typically low Seebeck coefficients of pure metals. Near room temperature, a large list of pure metals, including Ag, Al, Au, Cd, Cs, Cu, Dy, In, Ir, Mg, Nb, Pb, Rh, Sn, Sr, and Ru[51], shows absolute Seebeck below 5 $\mu V/K$.

Yet exceptions exist. For instance, pure metals like cobalt, iron and nickel have relatively large Seebeck coefficients[51]. Due to the inherence magnetization of these elements, part of their Seebeck coefficient has been attributed to magnon-drag. Watzman et al. [52] discussed the two magnon-drag contributions to thermopower(Seebeck coefficient): the hydrodynamic contribution and the spin-motive force contribution. They demonstrated that the Seebeck of Fe and Co can be explained by the magnon-drag, or more specifically, the magnonic heat flux dragging along the electronic charge carriers. However, the magnon-drag contribution in Ni is small. In the case of Ni, the large Seebeck coefficient can be attributed to the sharp peak of the DOS at the Fermi due to partially filled d-orbital[53], which leads to high Seebeck (See equation 1-17).

Nickel alloys were also demonstrated to have large Seebeck coefficient values, larger than pure Ni. Nickel solid-solution alloys with other transition metals including Cu and Au are shown to have high Seebeck coefficient values. This was hypothesized to be related to the inter-band scattering between s and d-orbital electrons[53]. Copper-nickel alloys have been studied in the past for traditional TE applications due to their relatively high Seebeck coefficients compared to other metals, their abundance of free electrons, their low cost, and their ease of fabrication.[54] Mao et al.[55] reported the enhancement in thermoelectric

performance of copper-nickel alloy (constantan) originating form nanoscale twin boundaries introduced by the ball-milling and hot-pressing (BM–HP) process. They obtained a 12% improvement for the Seebeck coefficient and a TE power factor of 40 μW cm^{-1} K^{-2} at 300 K and 102 μW cm^{-1} K^{-2} at 873 K. This serves as the highest power factor reported in the literature for Cu-Ni alloys. The addition of other elements such as tin and tungsten were also investigated in combination with Cu-Ni but only resulted in lower thermal conductivity and did not enhance the TE power factor.[56] Garmroundi et al.[53] observed the Seebeck of 94 $\mu V/K$ in quenched metastable single fcc Ni-Au alloy at 1000K, which leads to a ultra-high peak power factor of 340 μW cm^{-1} K^{-2} in $Ni_{0.1}Au_{0.9}$ sample at 560K. The high thermopower is explained by the steep slope of $DOS(E_F)$ arising from the unique band structure due to alloying, and therefore an electron-hole selective scattering of s-electrons into localized d-states that leads to strongly energy-dependent carrier mobility. Other alloys reported with high Seebeck include Fe-Ni[57,58], Cr-Mn[59], Cr-Fe[60],

Another class of metals that we propose to study here is the subcategory of intermetallic compounds with large Seebeck coefficient. Intermetallic compounds such as $YbAl_3$, YbPd and $CePd_3$ show large absolute Seebeck coefficient values in the sub-room temperature range. In $CePd_3$ the electron correlation effect results in a Seebeck coefficient of more than 115μV/K at 150K.[50,61,62] The Kondo resonance caused by the interaction of Yb 4f-orbital electrons and conduction bands gives $YbAl_3$ a Seebeck of -90 μV/K below room temperature.[63–65] YbPd[66] can maintain an absolute thermopower above 100μV/K from 200K to 300K. The band structure studies of these intermetallic compounds show they share a similar sharp density of states (DOS) singularity near the Fermi surface[67–69].

Here we propose to study selected candidates for active cooling from binary metallic alloys and intermetallic compounds. The candidates are selected based on their potentially large Seebeck coefficient values.

2. Experimental and characterization Methods

The synthesis and fabrication methods used in this thesis include Mechanical alloying (MA)/ball milling, sealed ampoule melting, arc-melting, direct energy deposition (DED), and hot pressing. The characterization methods include X-ray diffraction (XRD), Scanning electron microscopy (SEM)/ Energy-dispersive X-ray spectroscopy (EDS), and transport measurements including thermal/electrical measurements (Versalab and ZEM-3) and Laser flash thermal diffusivity measurements.

2.1 Synthesis and fabrication

2.1.1 Mechanical Alloying (MA)/Ball Milling

Mechanical alloying (MA)/Ball milling is a solid-state powder processing technique that involves repeated fracturing, cold welding, and rewelding of powder particles within a high-energy ball mill. The mechanism involves intense deformation and repeated collisions of powder particles in a high-energy ball mill. When impacted by milling balls, ductile particles are flattened and undergo cold welding, increasing their surface area, while brittle particles fracture and are refined. This combination of welding and fracturing produces a fine, layered structure that continues until a homogeneous microstructure is achieved. MA facilitates alloy formation through crystal defects, which enhance diffusion, leading to diverse phase formations, including solid solutions, intermetallic compounds, and amorphous phases. This process enables alloying even in systems with positive heats of mixing, expanding alloying possibilities.

For works in this dissertation thesis, the MA/ball milling process was carried out on a VQ-N high-energy vibratory ball mill from Across International. The ball mill features 1200 rpm oscillation speed, coming with an 80mL stainless steel jar with rubber-ring-sealed threaded cap. The default grinding media is stainless steel balls with 10mm and 6mm diameter.

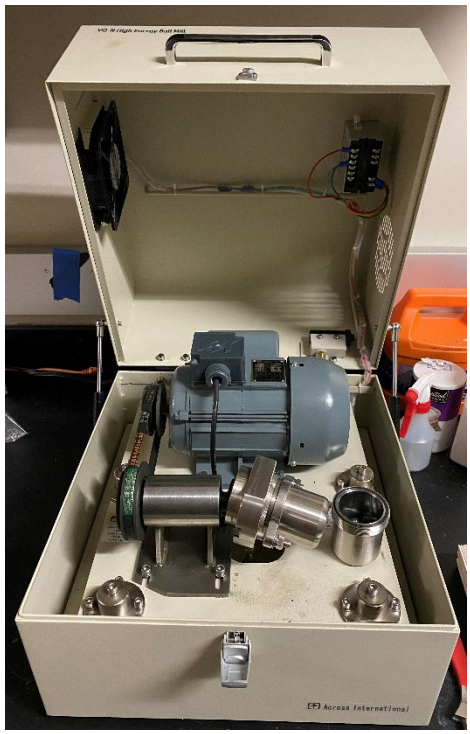

Figure 2-1 High energy vibratory ball mill

2.1.2 Sealed Ampoule Melting

Sealed ampoule melting is a technique in materials science used to prepare high-purity materials and compounds, particularly those that are sensitive to air or require specific atmospheres to prevent contamination or oxidation. In this method, the starting materials are placed in a sealed, evacuated, or inert-gas-filled fused-quartz ampoule, which is then heated to the required temperature to achieve melting or solid-state reactions. This controlled environment enables precise synthesis of compounds like semiconductors,

chalcogenides, and other materials where maintaining purity and avoiding unwanted reactions are essential.

For works in this dissertation thesis, the shared encapsulating station of the department of materials science is utilized to make the sealed ampoules. The encapsulating station features two sealing portals that allow fused quartz tubes with 12mm and 19mm outer diameters. The fused quartz tubes are purchased from Technical Glass Product, Inc. The tubes are coming with both ends open. The closed end and the sealing are made by heating the tubes using an oxyhydrogen torch. Before sealing, the initial materials are put inside tubes with one end sealed. Then the tubes are attached to the portal on the encapsulating station with double O-ring sealing, vacuumed and then purged with argon gas three times before sealing. The sealed ampoules held by alumina crucibles are heated in a KSL-1100

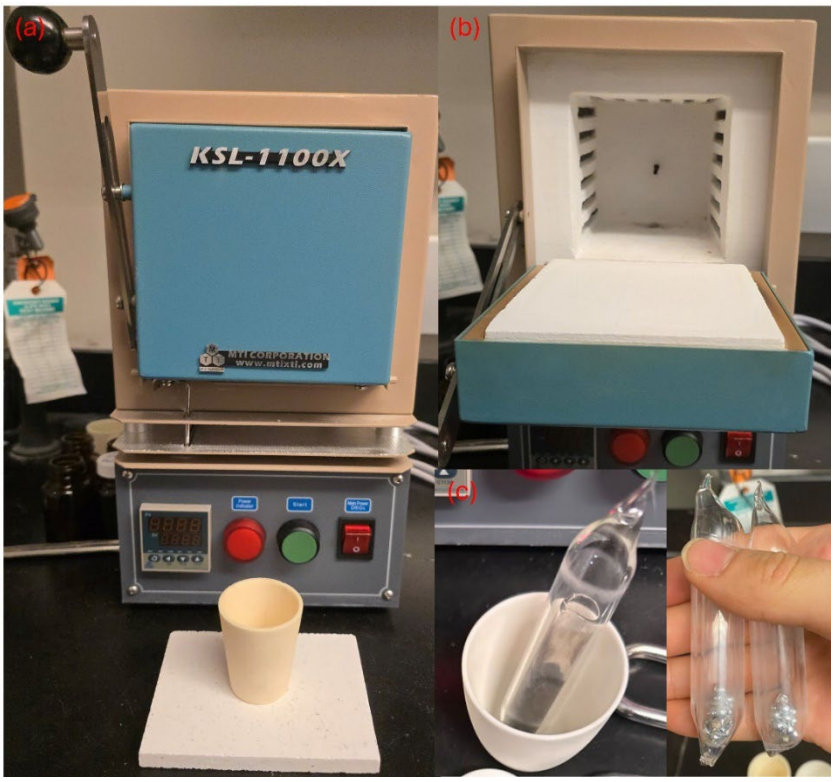

Figure 2-2 Muffle furnace and encapsulated ampoules. (a) muffle furnace (b) furnace chamber (c) encapsulated ampoule samples.

compact muffle furnace, which offers 4"x4"x4" high-purity fibrous alumina chamber and 30-segment, programmable temperature controller.

2.1.3 Arc-melting

Arc melting is a high-temperature synthesis and processing technique commonly used in materials science for producing high-purity metallic alloys and compounds. The process involves creating an electric arc between a tungsten electrode and the sample, which is placed on a conductive, typically copper, hearth. The arc generates temperatures exceeding 3000 °C, making it especially suitable for melting refractory metals or materials with high melting points. By operating in an inert atmosphere, often argon, arc melting minimizes oxidation and other contaminants, which is crucial for achieving high-purity results. During melting, the intense heat of the arc uniformly liquefies the sample, allowing for homogenous mixing and rapid solidification upon cooling. Arc melting is favored in alloy synthesis, particularly when precise compositional control and minimal contamination are required.

In this research, a custom-built arc-melter at the University of Virginia (by Prof. Shiflet), was employed to produce metallic samples. The system consists of a water-cooled stainless-steel bell jar that is hinged to a fixed baseplate, allowing for safe and controlled high-temperature operation. The electrode stinger, sealed with a ball joint and stainless steel bellow, can be precisely maneuvered under controlled pressure conditions. The water-cooled copper health has several concaved indentations allowing multiple samples loading at the same time. The chamber can be vacuumed to a level of approximately 1 Pa by a roughing oil vacuum pump attached, which is then backfilled with argon to create an inert atmosphere. The arc power is adjustable by adjusting the input current. This setup provides

flexibility and a high level of control, making it a suitable choice for advanced materials processing.

2.1.4 Direct Energy Deposition (DED)/Additive Manufacturing(AM)

Additive Manufacturing (AM) is a layer-by-layer fabrication process that directly constructs three-dimensional objects from digital designs, enabling production of complex, customized geometries with minimal waste. This approach has gained great interest in industries such as aerospace, automotive, and biomedical sectors, especially as metal AM processes have advanced. Among these, Directed Energy Deposition (DED) is notable for its versatility in producing high-performance, multi-material parts and performing repair applications on existing components[70,71].

DED works by focusing thermal energy, typically from a laser, electron beam, or plasma arc, onto a substrate while feeding material in powder or wire form into the melt pool, layer by layer. This enables high deposition rates and the production of dense, near-net-shape structures. DED's ability to handle a wide range of materials, from alloys to functionally graded materials, makes it suitable for rapid manufacturing and repairs. While the process can introduce directional microstructures and residual stresses due to its repeated thermal cycles, advanced monitoring and process controls are applied to optimize material properties and minimize defects[70,71].

Founded in 2011, the Commonwealth Center for Advanced Manufacturing (CCAM) is a not-for-profit applied research center that fosters collaboration between industry, academia, and government. CCAM specializes in advanced manufacturing technologies, including Directed Energy Deposition (DED). In the project discussed in chapter III, I collaborated

with Kyle Snyder from CCAM for utilizing their DED abilities. Kyle also tuned the process parameters for the DED manufacturing of the Cu-Ni alloys.

2.1.5 Hot Pressing

Hot pressing is a sintering technique in which heat and uniaxial pressure are applied to material powders contained in a rigid die. The uniaxial pressure accelerates atomic movement at particle contact points, facilitating the growth of cohesive necks between particles. This leads to densification and some grain growth while allowing sintering at lower temperatures and shorter times compared to conventional sintering[72]. The radical pressure applied to the powder is lower than the axial one, which can lead to anisotropic microstructures, where grains in the radial direction may grow larger than those in the axial direction[72]. Despite this, hot pressing is widely used for producing dense, strong components with controlled grain growth.

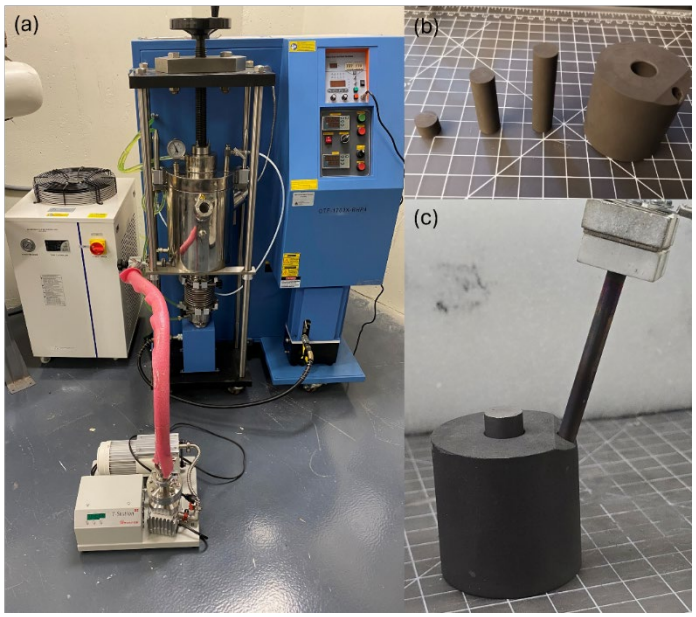

Figure 2-3 Hot pressing device and graphite die (a) hot pressing device with water-cooling station and vacuum pump, (b) graphite die and pushing rods, (c) loaded graphite die with thermocouple inserted.

The hot pressing in the following projects was performed by an OTF-1700X-RHP4 vacuum rapid heated pressing furnace MTI corporation. The setup features a 15 kW temperature controllable induction heater with water-cooled copper induction coil that can heat up the powders loaded in the graphite die at 4°C per second up to 1200°C. The pressure is supplied by electric hydraulic press with automatic pressure controller, providing maximum 100MPa pressure on the powder. A b-type thermal couple encapsulated in a tantalum sheeve is used to insert into the die to measure the temperature around the sample position. The hot press chamber can be sealed and vacuumed by a T-Station 85 turbo vacuum station from Edwards up to 0.1mbar, then back-filled by argon gas. This rapid heated hot pressing produces dense pallets from powders under the protective gas environment at a higher heating rate than conventional hot pressing, which limits the grain growth[73].

2.2 Characterization and Transport Measurements

2.2.1 X-ray diffraction (XRD)

X-ray diffraction (XRD) is a widely used technique in materials science for phase identification and lattice parameter determination. In this study, powder and bulk XRD are utilized to index phases. The fundamental principle of XRD lies in the interaction of monochromatic X-rays with the periodic lattice planes of a crystalline material. When X-rays encounter these planes, they are scattered by the atoms, and constructive interference occurs when the path difference between rays scattered from adjacent planes satisfies Bragg's law:

$$n\lambda = 2dsin\theta \qquad (2-1)$$

where n is the order of reflection, λ is the X-ray wavelength, d is the spacing between lattice planes, and θ is the angle between the incident beam and the normal to the reflecting plane. This interference produces a characteristic pattern of diffraction peaks that is unique to each phase, enabling phase identification. In powdered or polycrystalline samples with randomly oriented crystallites, a full diffraction pattern can be obtained by varying the 2θ angle along a fixed scattering direction, capturing all potential reflections. This pattern provides critical structural information, allowing for the calculation of lattice parameters and an in-depth understanding of the sample's crystallographic properties.

The powders and bulk samples were characterized by an Empyrean diffractometer from Malvern-Panalytical belonging to Nanoscale Materials Characterization Facility (NMCF) at the University of Virginia. The samples are measured spinning at 16 rpm. The XRD data are processed and analyzed using the X'pert Higherscore software.

2.2.2 Scanning electron microscopy (SEM)/ Energy-dispersive X-ray spectroscopy (EDS)

Scanning Electron Microscopy (SEM) is a versatile imaging technique that uses a finely focused electron beam scanning over a sample's surface to produce high-resolution images and compositional data. The two imaging modes most frequently used are secondary electron (SE) imaging, which highlights surface topography, and backscattered electron (BSE) imaging, which reveals contrasts in chemical composition based on atomic number differences. The electron beam's energy, controlled by adjusting the accelerating voltage (typically 1–30 kV), influences the interaction volume within the sample and, in turn, affects the depth of analysis and the range of X-rays generated. These X-rays can be further analyzed with Energy-Dispersive X-ray Spectroscopy (EDS), a semi-quantitative

technique for elemental composition. EDS detects characteristic X-rays emitted by atoms in response to the electron beam, compiling them into an energy spectrum that uniquely identifies elemental composition. For instance, the K-alpha and K-beta peaks correspond to electrons returning to the K shell, providing elemental signatures. Heavier elements tend to yield more accurate compositional data due to a greater number of distinguishable energy shells, while lighter elements may show overlapping peaks in the low-energy spectrum. EDS offers several analytical modes, including line scan, mapping, and spot analysis. In line scan mode, the electron beam is moved along a specified line on the sample, providing compositional data along that path to reveal elemental distribution changes over distance. Mapping mode, by contrast, captures the spatial distribution of elements across a defined area, producing color-coded maps that visually represent the concentrations of various elements. These modes allow for detailed compositional analysis, complementing

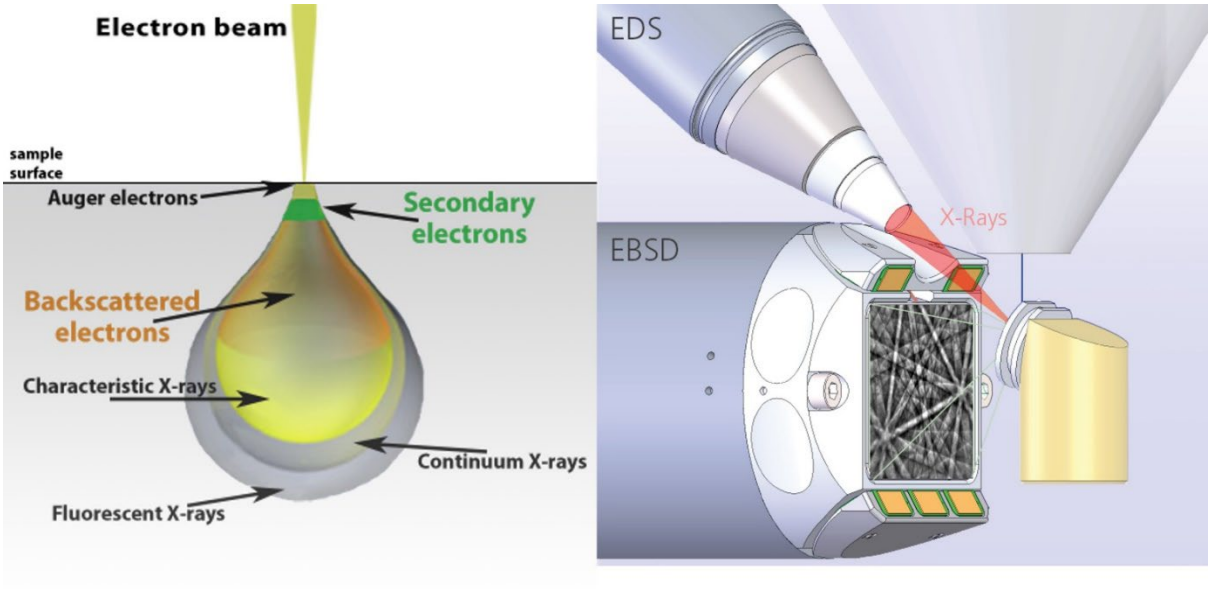

Figure 2-4 The interaction of the electron beam with the sample (left), and the geometry of the e-beam, EDS, and EBSD (right).

the imaging information obtained through SEM. Data for this work was collected on an FEI Quanta 650 SEM equipped with an Oxford EDS system at the University of Virginia.

2.2.3 Thermal/electrical measurements

The thermal and electrical properties of the samples are measured by a Quantum Design PPMS® VersaLab® physical property measurement system. It is a cryogen-free material

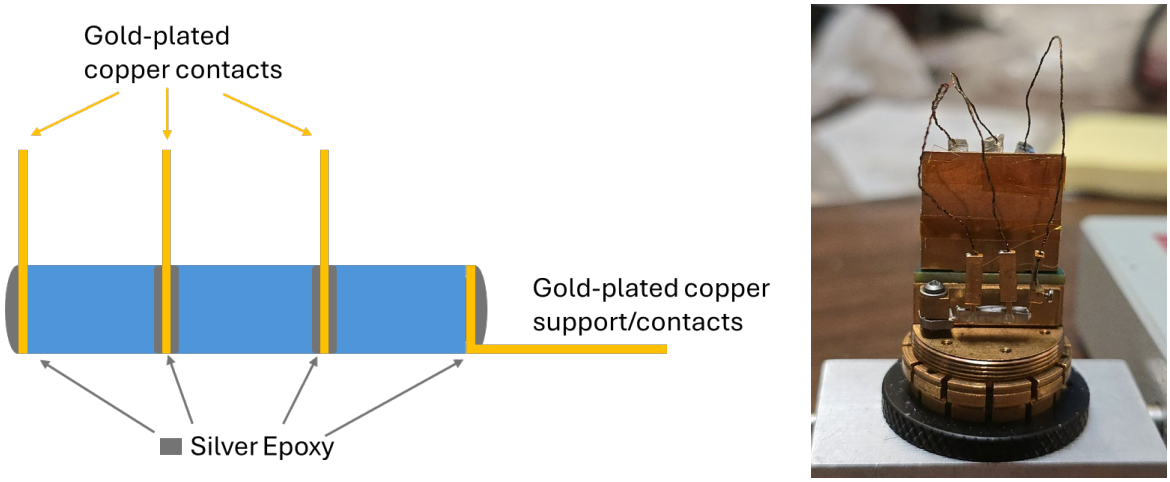

Figure 2-5 The bar-shape sample with gold-plated contacts (left), and the sample-loaded measurement stage with heating and thermal probes connected (right).

characterization system based on a cryocooler, offering a temperature range from 50 K to 400 K and a magnetic field capability of up to 3 Tesla. The Thermal Transport Option (TTO) for the Quantum Design PPMS enables simultaneous measurement of a sample's thermal conductivity, Seebeck coefficient, and electrical resistivity, facilitating the calculation of the thermoelectric figure of merit (ZT) across the 50K-400K range. The TTO operates under high vacuum, using a thermal pulse and model-based fitting algorithms to obtain thermal conductance and thermopower values, followed by a four-probe electrical resistance measurement. The system's adaptive measurement algorithm supports continuous data acquisition while ramping temperature, allowing efficient collection of high-density data.

In four-probe resistivity measurement, current is applied through the outer contacts, and voltage is measured across the inner contacts. This setup minimizes the influence of contact resistance, allowing for a precise determination of the sample's intrinsic resistivity. By isolating the voltage measurement from the current-carrying contacts, the technique provides high accuracy, especially crucial in materials with low resistivity, where contact resistance can otherwise introduce significant error.

The samples were cut into approximately 2 mm × 2 mm × 10 mm bars using an abrasive cutting saw. Four gold-plated copper contacts were then bonded to the sample surface using H20E conductive silver epoxy, as shown in Figure X. In this configuration, the left-end contact acts as the heat source to establish a temperature gradient for measuring thermopower and thermal conductivity, while also serving as the current injection point in resistivity measurements. The right-end contact functions as both the heat sink and current return probe, attaching to the puck stage to complete the thermal and electrical circuit. The two inner contacts, positioned along the sample length, serve as temperature sensors for thermal measurements and as voltage probes for resistivity measurements.

2.2.4 Laser flash thermal diffusivity measurements

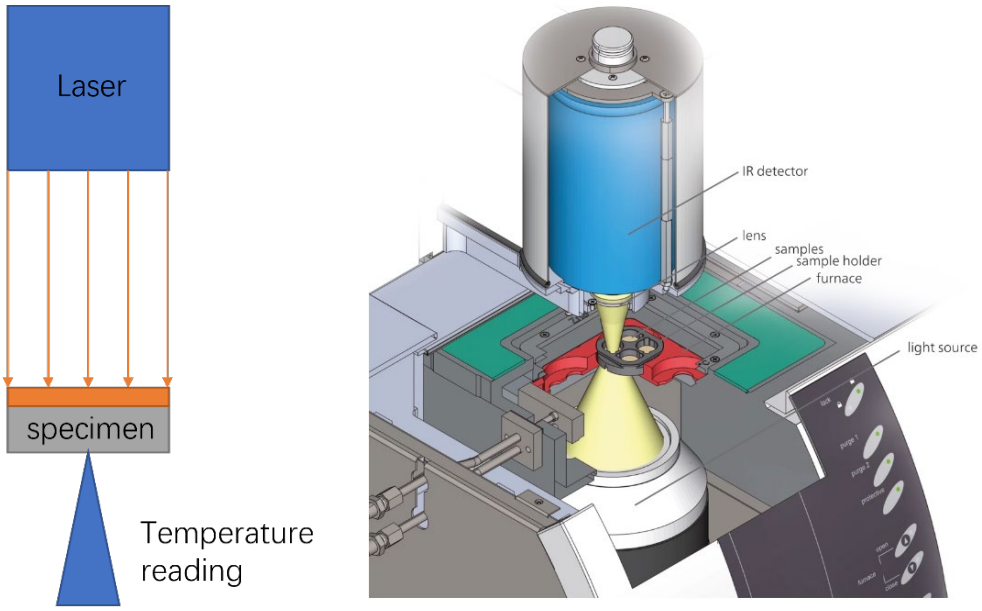

Figure 2-6 Schematic diagram of laser flash measurement

The laser flash method is used for measuring the thermal diffusivity of materials. In this method, an intense laser flash pulse is directed onto the front surface of the sample with limited thickness and size. This pulse creates a rapid temperature increase that diffuses through the material, and the resulting temperature rise is monitored on the sample's rear surface over time. By analyzing the rate at which heat propagates through the sample, the cross-plane thermal diffusivity can be calculated.

The thermal diffusivities of the bulk samples in this dissertation thesis were measured by a Netzsch LFA 467 Laser Flash instrument. The thermal conductivity of the samples is calculated using

$$\kappa = C_p \alpha \rho$$

where: κ represents the thermal conductivity (W/(m·K)). C_p is the specific heat capacity at constant pressure (J/(kg·K)). α is the thermal diffusivity (m^2/s). ρ is the density (kg/m^3).

The laser flash measurement is used to validate the thermal conductivity measurement by the PPMS Versalab.

3. Binary Alloy Approach

To maximize the κ_{eff}, metallic materials are preferred over traditional thermoelectrics due to their high passive thermal conductivity and electrical conductivity. Although some of the pure metals such as Co, and Ni exhibit relatively high Seebeck that combined with the electrical conductivity leads to noticeable power factor, further optimization of the power factor of metallic materials are still desirable. One of the approaches would be the alloys based on the high-Seebeck metals. With the success of CuNi[55], PdAg[74], NiAu[53], and reported high Seebeck samples of Cr-Mn[59] and Fe-Ni[57,58], high Seebeck is achievable by tuning the band structure of the binary alloys to optimize the density of states near Fermi level, manipulated scattering mechanisms or use Magnon-drag effects in the case of magnetic elements[5,52,53]. The binary alloys with at least one transition metals with partially filled d- or f-orbitals are suggested as potential candidates for large power factors due to possible sharp DOS near the Fermi level and inter-band scattering between s and d-orbital electrons.[53]

We explored the phase diagram and collected reported data on the thermoelectric performance of binary alloys. In our search, we found the following alloys are potential candidates for high power factor, high thermal conductivity materials: Co-Zn, Co-Sn, Cr-Fe, Cr-Mn, Fe-Sn, Fe-Al, Fe-Ni, Ni-Sn, and Ni-Zn, in which only Fe-Ni and Cr-Mn has been reported for Seebeck. All these candidates are binary alloys with one component being a high Seebeck pure metal. The thermoelectric properties have never been reported or optimized for active cooling for any of these alloys. In this study, trials are made on Cu-Ni, Ni-Fe, Cr-Mn, Co-Sn, Co-Al, and Ni-Sn alloys. The best results presented here are for Cu-Ni and Ni-Fe alloys.

3.1 Cost-efficient Copper-nickel Alloy for Active Cooling Applications

3.1.1 Background

In this project, we study the potential of additive-manufactured copper-nickel alloys for active cooling. We focus on additive manufacturing for two reasons. The first is to reduce the manufacturing cost. The current cost of manufacturing TE modules is high, preventing their wide commercialization. High-purity elements are often used in manufacturing TE modules to prevent oxidization and enhance the material figure of merit. However, high-purity elements, copper and nickel in our case, are much more expensive than industrial-grade ones. The process of mixing and alloying the pure powders in an inert environment further adds to the cost. The same problem exists and is harsher for making other classic TE materials such as Bi_2Te_3, in which the presence of tellurium can render the cost excessively high.[75] Attempts to lower the cost include co-optimizing the module geometry, cost, and power output[76], and usage of industrial waste powders.[77] Fan et al. for instance, showed that bismuth telluride developed from waste powders can closely match bismuth telluride created from high purity materials in terms of the Seebeck coefficient. [78] The second reason to use additive manufacturing is to enable the manufacturing of complex geometries. Frequently, the heat sources and sinks possess complex geometries which are needed to maximize the surface area and hence increase the coupling of the heat sink to the air- or water-cooling system for effective convective cooling. [79,80] The heat sink often needs to be shaped to match the heat source geometry to minimize thermal contact resistance. [81] The required complex geometry of the heat sinks is ill-suited for rigid TE devices constructed using traditional manufacturing methodologies.[82] The use of additive manufacturing (AM) to create TE devices permits the creation of modules with more

complicated shapes to accommodate various shapes of heat sources. AM also provides other benefits including reduced feedstock waste and shorter manufacturing cycles.[82–85] Traditional manufacturing techniques generate parts by subtractive methods in which material is removed from a large, initial volume until the desired geometry is achieved. In contrast, AM utilizes computer-aided design (CAD) models to construct parts in a layer-wise fashion from computer-generated cross-sections, typically ranging from 20 μm to 1 mm in thickness.[71,83,86–88]

This project is focused on the manufacturing of low-cost copper-nickel alloys with high κ_{eff} for active cooling applications. Industrial-grade powders are used to lower the cost. We use traditional methods including mechanical alloying followed by hot-pressing and arc-melting as well as Laser-Powder-based Directed Energy Deposition (LP-DED), a specific type of additive manufacturing (AM), to process these alloys. For the three different processes, we use the same batch of industrial powders. We compare the results in terms of the material's TE power factor, thermal conductivity, and most importantly effective thermal conductivity. The final goal is to make highly efficient heat sinks with complex geometries using the AM process and the project is the first step toward that goal. In what follows, we first introduce the experimental procedures to make and characterize the samples. Then, the performances of the samples and their relation to different experimental factors are discussed.

3.1.2 Experimental and Characterization

Ball Mill-Hot Pressed (BM-HP) Method: Industrial-grade 99.3 % copper (METCO 55) and nickel powders (METCO 56C-NS) are purchased from Oerlikon Metco at the cost of 48 $ per kg for copper and 65 $ per kg for nickel. In contrast, 99.999% copper from sigma

Aldrich costs 25.4 $ per gram, and 99.99% nickel costs 2.2 $ per gram. The purchased powders came in 5 lb. plastic bottles filled with air and are stored in the air. The mass ratio was determined based on atomic percentage. The powders were weighted and mixed in the air. One mass percent of selenium was added to all the ball-milled samples to avoid the products' agglomeration and sticking to the ball mill jar. No peak of selenium or selenide is found in the XRD results of the ball-milled powders. The mixture is then loaded into a stainless steel ball-milling jar. A VQ-N high-energy vibratory ball mill from Across International was used to ball mill the mixed powder for the maximum continuous working time of 9999 seconds, at 1200 rpm. Then around 2.5 grams of the product powder was loaded in a graphite die, and hot-pressed under 56 MPa pressure for 300 seconds using an OTF-1700X-RHP4 hot-press setup from MTI corporation. In the trial range of 600 ˚C to 950 ˚C, 800 ˚C was found as the optimum pressing temperature. The hot press chamber was filled with argon gas during the process. A disc-shaped solid sample with a diameter of 12.7 mm was obtained after polishing the hot-pressed ingot. The disc-shaped sample was then cut by a Mager BR220 precision cut-off saw into bar-shaped samples with approximate 2mm × 2 mm × 10 mm dimensions. The pure copper and pure nickel samples were made by directly pressing the ingredient powders.

Hot Press-Arc Melt (HP-AM) Method: The same ingredient powders, which were used for the BM-HP method were mixed and hand-milled in air. The same hot-press setup was used to hot-press the hand-milled sample at 600 ˚C under 56 MPa pressure for 300 seconds to form a pellet. The final pellet was prepared by arc melting in the argon atmosphere. Each ingot was melted three times to ensure homogeneity. The melted ingot was cut and processed using the same procedure as the BM-HP samples.

Direct Energy Deposition (DED) Method: The DED process was done by Kyle Snyder at the Commonwealth Center for Advanced Manufacturing of Virginia. The process used here (DED) provides a typical range of 0.5-5 mm. Using these cross-sections as a template, powder or wire feedstock is deposited layer-by-layer and melted using a diode laser as a heat source.[83,87,89] To successfully join materials in AM, the delivery of feedstock and energy must be optimized for the materials being used, with various techniques existing to join plastics, polymers, ceramics, and metals. [71,83,86,89,90] Powder-based directed energy deposition (PB-DED) has had particular success with the generation of metallic parts and entails the simultaneous deposition and melting of metallic powder. [83,86]

There are myriad process parameters that impact the eventual microstructure and mechanical properties of deposited materials including laser power, scanning speed, scanning pattern, feedstock rate, and time between successive layers. [71,86,91,92] The density of the deposited material is of critical importance as a high density is needed.

Four samples were prepared using DED processes and tested for their TE properties. All samples were made from the original industrial powder mixing in the ratio of 65% Cu and 35% Ni. The mixture was obtained by tumbling Cu and Ni powders for 8 hours to make a 5 kg batch of 65% Cu-35% Ni. Initial parameter development was conducted by depositing single bead tracks with varied core process parameters to determine optimized settings. Core process parameters include laser power, scan speed, powder flow rate, laser spot size, and step-over distance. Larger, bulk tests samples were produced with three different process parameter settings to eliminate porosity. The first batch of samples, B1S1 and B1S2 received “baseline” process parameters based on the initial parameter development study as summarized in Table 3-1. A lack of fusion or incomplete melting/fusing of adjacent

tracks was observed. In the second batch of samples, sample B2S3 received a reduced scan speed with the expectation that a slower scan speed would produce a wider deposit and allow complete melting between adjacent tracks. Sample B2S4 received a reduced stepover distance (stepover between tracks) with the expectation that depositing the tracks closer together will allow for complete melting between adjacent tracks.

Table 3-1 Summary of samples made using the DED process

Sample #	Laser Power (W)	Scan Speed ($mm.s^{-1}$)	Powder Feed Rate ($gr.min^{-1}$)	Stepover Distance (mm)	Density ($gr.cm^{-3}$)
B1S1	800	550	5	1.05	8.25±0.20
B1S2	800	550	5	1.05	8.34±0.02
B2S3	800	500	5	1.05	8.36±0.16
B2S4	800	550	5	0.95	8.46±0.13

Material characterization and property measurement: The electrical resistivity, Seebeck coefficient, and thermal conductivity were measured in a PPMS Versalab system from Quantum Design Inc. The thermal conductivity was cross-checked using the Netzsch Laser Flash setup. The error bars of the Seebeck coefficient, resistivity, and thermal conductivity measurements are ±5%, ±3%, ± 3% respectively.

The powders and disc-shaped samples were characterized by an Empyrean diffractometer from Malvern-Panalytical. The mass density of the DED samples is determined by Archimedes' method using a Secura Precision balance with a YDK03 density kit. Multiple parts cut from each sample block are measured at 22.5˚C and the average density of each sample is calculated by taking the arithmetic average of all the parts measured. The results are reported in Table I.

3.1.3 Result and Discussion

Material characterization

Samples of $Cu_{1-x}Ni_x$ were made using mechanical alloying, arc melting, and DED as described in the experimental section. The composition reported within this work (the value of x) is the initial composition, which stands for the atomic ratio of the initial powders we calculated, weighed, and mixed, not the actual composition of the final samples. Due to the quality of the powders and the synthesis process, the final composition can be slightly different from the initial one. The XRD results in Figure 3-1 show that the ingredient copper powder (purple triangles) contains Cu_2O (peaks marked by grey rhombuses). Since the ball milling was performed in air, during the process, more oxygen was introduced as indicated by the increased relative intensity of oxide peaks of the BM-HP sample. The sample prepared by hot-pressing the mixture without ball milling, labeled as HP-$Cu_{52}Ni_{48}$, shows two separate series of peaks corresponding to pure copper (purple triangle) and pure nickel (yellow triangle) while the ball-milled then hot-pressed sample (BM-HP-$Cu_{52}Ni_{48}$) shows only one series of peaks of copper-nickel alloy, demonstrating the effectiveness of ball-milling in alloying.

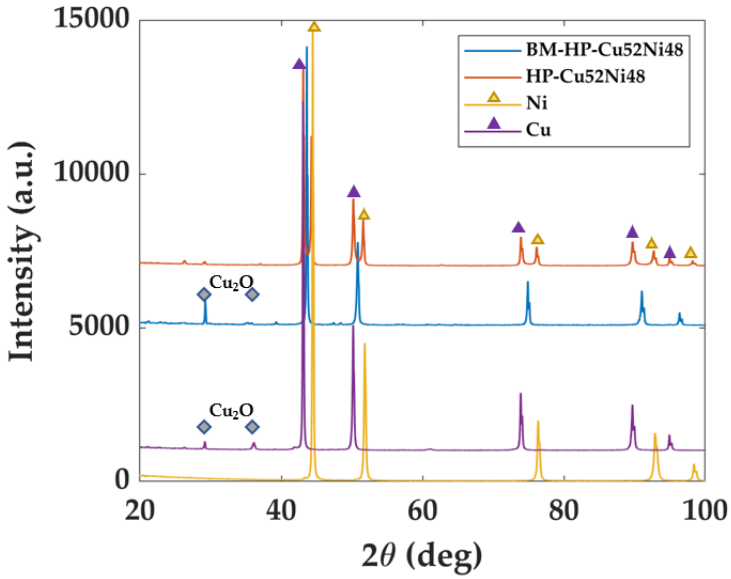

Figure 3-1 XRD results of copper powder (purple), nickel powder (yellow), ball-milled and hot-pressed sample (blue), and hot-pressed powder mixture without ball milling (orange).

Room Temperature Performance

A summary of the TE performance of the samples versus their copper-nickel ratio is presented in Figure 3-2. As shown in this figure, the Seebeck coefficient of the BM-HP samples reaches a peak at 60 atomic percent of copper, while the electrical and thermal conductivity increases as the copper fraction increase beyond 25%. All alloys show lower electrical and thermal conductivity compared to the pure copper and nickel samples as expected. The resistivity of the copper prepared by hot-pressing the industrial powder directly is twice larger than the one reported in the literature for pure copper (3.01×10^{-8} Ω m versus 1.55×10^{-8} Ω m [93]). This is due to the presence of copper oxide, impurities, and grain boundaries in our samples.[94] For the same reason, the thermal conductivity of as-pressed copper samples is also much lower than pure copper and is around 253 W m^{-1} K^{-1} compared to 350 W m^{-1} K^{-1} reported for pure copper.[95] The Seebeck coefficient however

is not affected and is similar to that of pure copper. The Seebeck coefficient of pure copper is 1.70 μV K^{-1}[96] and that of our sample is 1.75 μV K^{-1}. Similarly, the resistivity of the as-pressed Ni sample, 1.13 ×10^{-7} Ω m is higher than reported values in the literature, 6.20×10^{-8} Ω m.[93] The thermal conductivity of the as-pressed Ni sample is around 60 W m^{-1} K^{-1}, lower than the 93 W m^{-1} K^{-1} from reference [95]. The measured Seebeck coefficient, -15.3 μV K^{-1}, is like the reported value of -18.3 μV K^{-1} in reference.[96] for pure Ni. We also need to clarify the case of Cu_{100} vs $Cu_{98}Ni_2$. While the former does not contain any additives, the latter sample includes an extra 1% selenium consistent with our other alloys. This extra Se changes the Seebeck and the electrical conductivity significantly and as a result, the alloyed sample does not follow what is expected from a simply bowing model of binary alloys, instead, we see a very sharp change in the TE properties between these two samples.

Combining the Seebeck and the resistivity, the peak of the power factor is at 65 Cu atomic percentage, indicating $Cu_{65}Ni_{35}$ as the best-performing composition of the BM-HP alloys. The maximum power factor measured at room temperature for these alloys is 35 μW cm^{-1} K^{-2} which is comparable to the 40 μW cm^{-1} K^{-2} record power factor obtained by Mao et al. [97] reported for constantan made from high-quality copper and nickel powders. The HP-Arc melted sample and DED samples have a lower Seebeck coefficient than the BM-HP samples and higher electrical and thermal conductivity. The main difference between these two processes compared to BM-HP is the melting process, which can potentially result in larger grain sizes, lower oxygen levels, and fewer defects. In addition, Se was added in the BM-HP process which can serve as an extra impurity and further lower the electrical and thermal conductivity. Finally, the process of ball-milling in the air can introduce more oxygen to the system as indicated in Fig. 1, and hence can lower the

electrical and thermal conductivity. Despite the lower electrical and thermal conductivity, the overall power factor of the BM-HP sample is slightly larger compared to the AM-HP and DED samples. When calculating the effective thermal conductivity, we noted that all three $Cu_{65}Ni_{35}$ samples should perform similarly (within ~ 5%) in terms of their effective thermal conductivity. This 5 % is within the measurement and sample variations error bars.

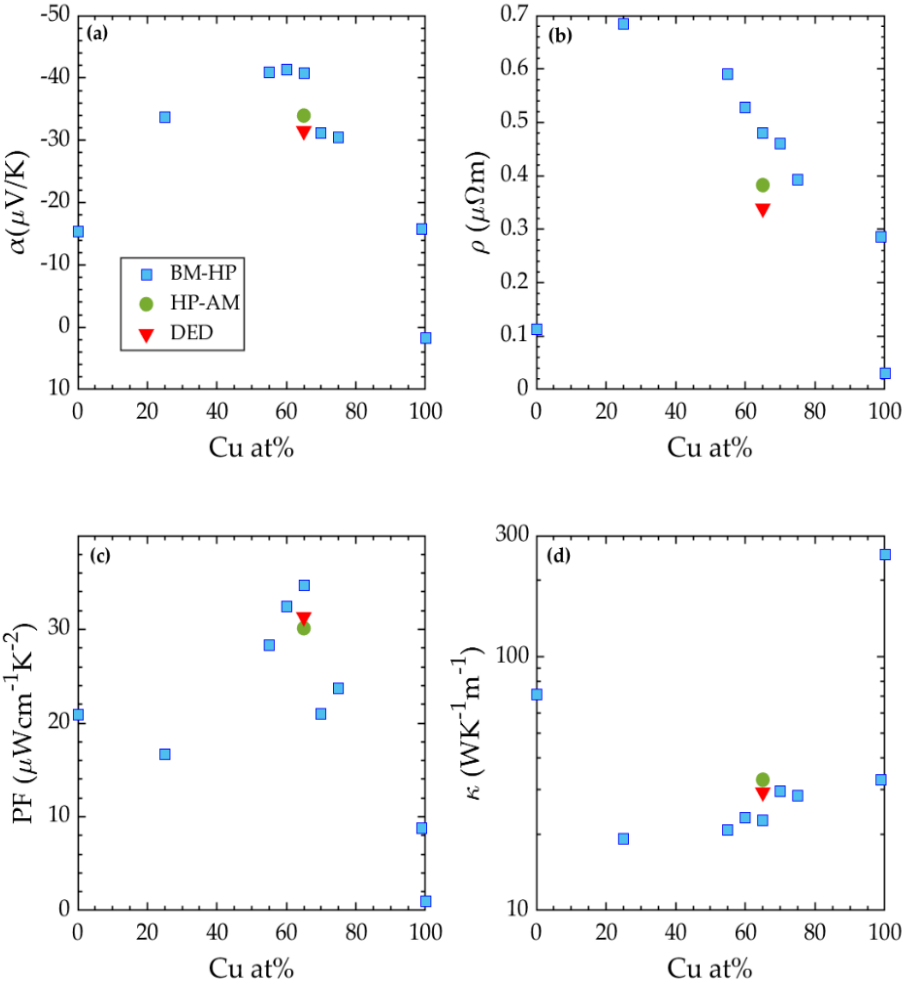

Figure 3-2 Variation of the (a) Seebeck coefficient, (b) Resistivity, (c) Thermal conductivity, and (d) Power factor with copper concentration. The blue squares show the data points of BM-HP samples with different compositions at 300K. The two ends (pure copper and pure nickel) were prepared by direct hot-pressing of the industrial-grade powders. The green circle stands for the hot-pressed- arc melted sample with the composition of $Cu_{65}Ni_{35}$. The red triangle stands for the DED sample with the $Cu_{65}Ni_{35}$ composition.

Comparison to Previous Study

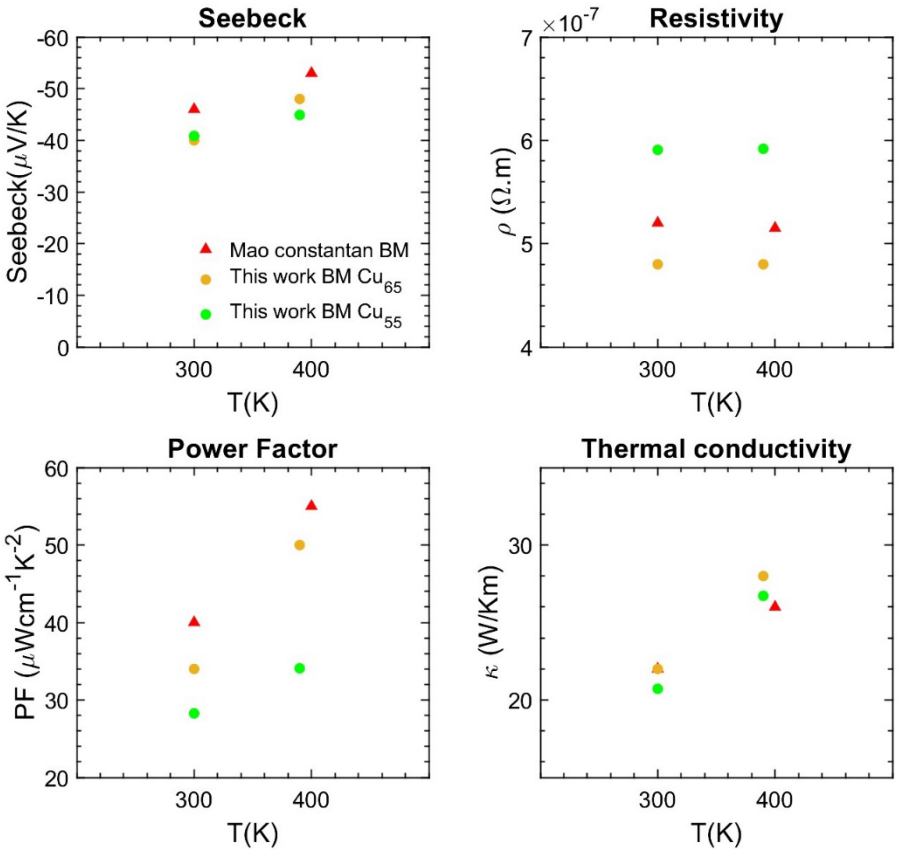

Figure 3-3 Comparison of the ball-milled (BM) samples in this work with the study by Mao et al.[55] on Constantan

The work of Mao et al[55] is focused on Constantan with the composition of $Cu_{56}Ni_{42}Mn_2$. The closest sample that we have in composition and is shown here is $Cu_{55}Ni_{45}$ sample. Comparing the results of our using industrial-level powder with the results from the literature, the differences exist in both Seebeck and resistivity at the same temperature. The reference reported higher Seebeck as well as lower resistivity, leading to a higher power factor. The thermal conductivities are comparable in the two studies.

The identifiable differences between the powder used in Mao's work and this work are the purity of the powder (99.5 Cu vs 99 Cu, 99.8 Ni vs 99.3 Ni), the storage, and the process

of mixing are done in a glovebox in Mao's work while in our work, both steps are operated in air. Therefore, the oxidization level of the copper powder should be much higher in our work, which can also be illustrated by the results from XRD. While Mao's samples don't show the copper oxide peaks compared, our samples do. Finally, the ball-milling time of the reference is 20 hours compared to 4 hours in this work.

The reference attributes improvement of the Seebeck coefficient to the nanoscale twin boundaries. it is reasonable to assume that the longer ball-milling time leads to more nano-twins and therefore higher Seebeck. And the lower conductivity in our sample can be explained by the existence of oxides.

We also compare our ball-milled $Cu_{65}Ni_{35}$ sample with Mao's Constantan sample. The composition of our samples is optimized among other samples formed from industrial powder for the power factor. The Constantan is optimized for its figure of merit.

The reference reported higher Seebeck but higher resistivity. But the Seebeck difference prevails leading to a higher power factor in the Constantan. The thermal conductivities are comparable in the two studies. The Seebeck difference can come from the composition and the amount of nano-twins resulting from the longer ball-mill time. The resistivity can be explained by the higher copper concentration for our $Cu_{65}Ni_{35}$ sample since copper is a better conductor than nickel. The lower thermal conductivity of Mao's Constantan can be related to the extra defects like nano-twins introduced by the longer ball-mill time.

Performance vs. Hot-press Temperature

Figure 3-4 shows a comparison of four BM-HP samples with different hot-press temperatures. All samples have the same $Cu_{65}Ni_{35}$ composition. The maximum TE power factor is obtained at 800 ºC pressing temperature. The passive thermal conductivity increases with the hot-press temperature. But in terms of effective thermal conductivity, when ΔT=1 K, the 800 ºC sample outperforms the 950 ºC sample. Hence, we choose 800 ºC as our default pressing temperature.

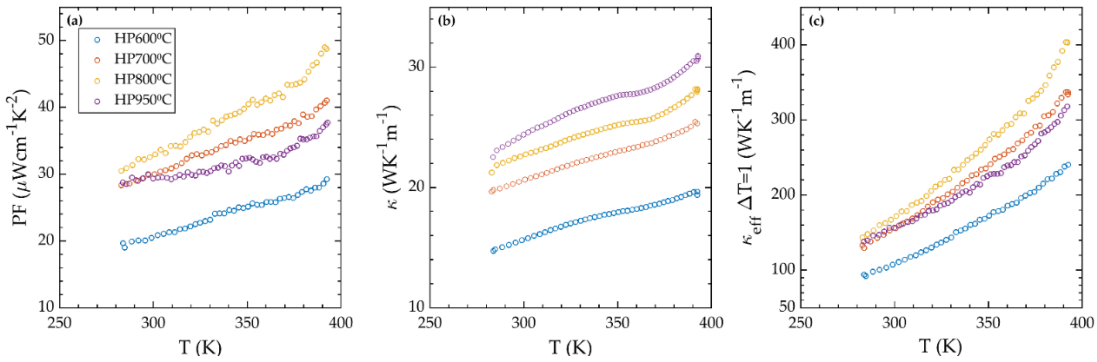

Figure 3-4 (a) power factor, (b) thermal conductivity, and (c) effective thermal conductivity (ΔT=1) of $Cu_{65}Ni_{35}$ samples hot-pressed under different temperatures from 600 ºC to 950 ºC

For electrical and thermal conductivity, the raised hot press temperature benefits both due increased grain coarsening and the decomposition of the oxides. The Seebeck of samples hot-pressed from 600 ˚C to 800 ˚C is minor compared to the Seebeck drop when hot-press temperature increases from 800 ˚C to 950 ˚C. A similar drop in Seebeck is observed in the literature as hot-pressing temperature increases from 800 ˚C to 900 ˚C, where the difference is considered negligible. To explain the performance dependence of the performance, we speculate the following results from rising hot-pressing temperature: the decomposition of the oxides, the coarsening of the grains, the loss of the selenium-introduced improvement, and the loss of the nano-twins which is introduced by ball-milling and benefits Seebeck.

From 600 ˚C to 800 ˚C, the first two mechanisms prevail, leading to improvement in performance, while beyond the optimal temperature, the last two lead to a major drop in power factor and therefore effective thermal conductivity.

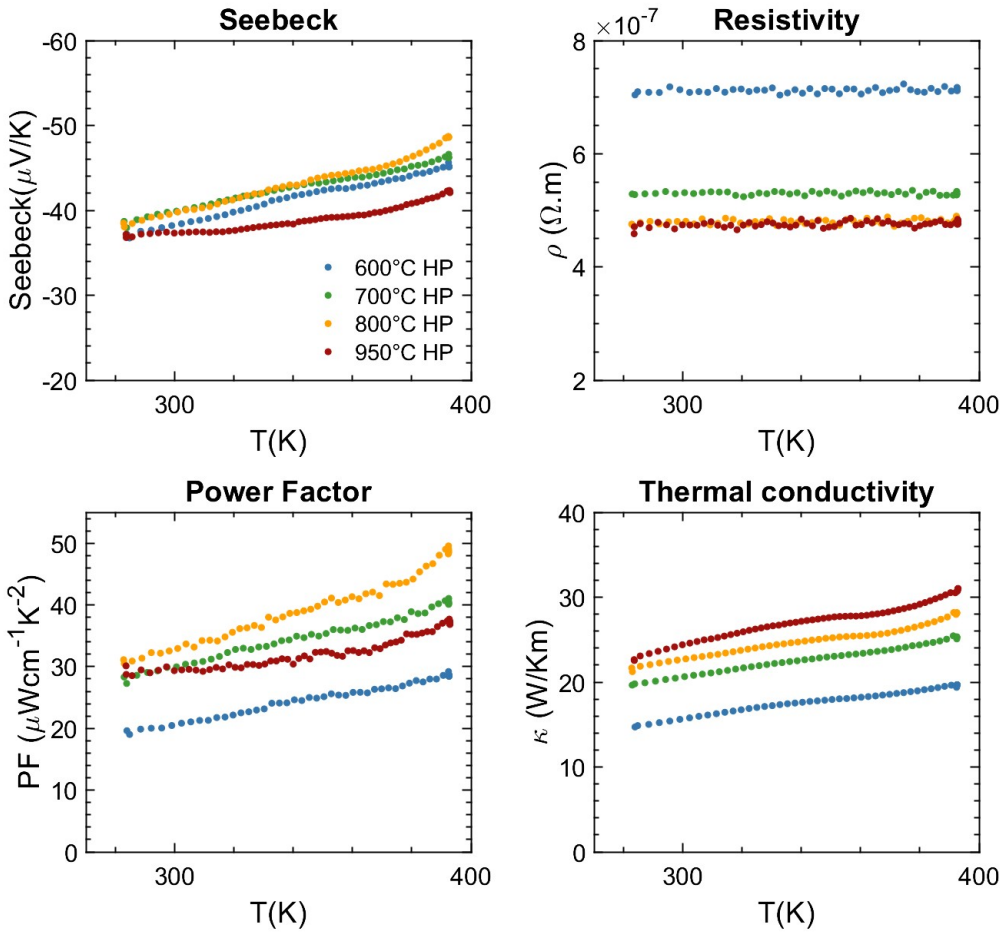

Figure 3-5 Comparison of the performance of BM-HP samples with different hot-press temperature.

Effect of Selenium Addition

Two identical BM-HP $Cu_{65}Ni_{35}$ samples were fabricated with different selenium powders. The first sample was made with fresh Se powders right after it was taken out of the glove box while the second sample is made using Se powders that were exposed to air for months and hence were partially oxidized. As shown in Figure 3-6, we see a large difference

between these two samples. For instance, at 390ºC, the sample made with fresh Se powder has a 15.3% higher Seebeck coefficient and a 12.9% lower resistivity compared to the sample made with partially oxidized Se powder. As a result, the difference in the TE power

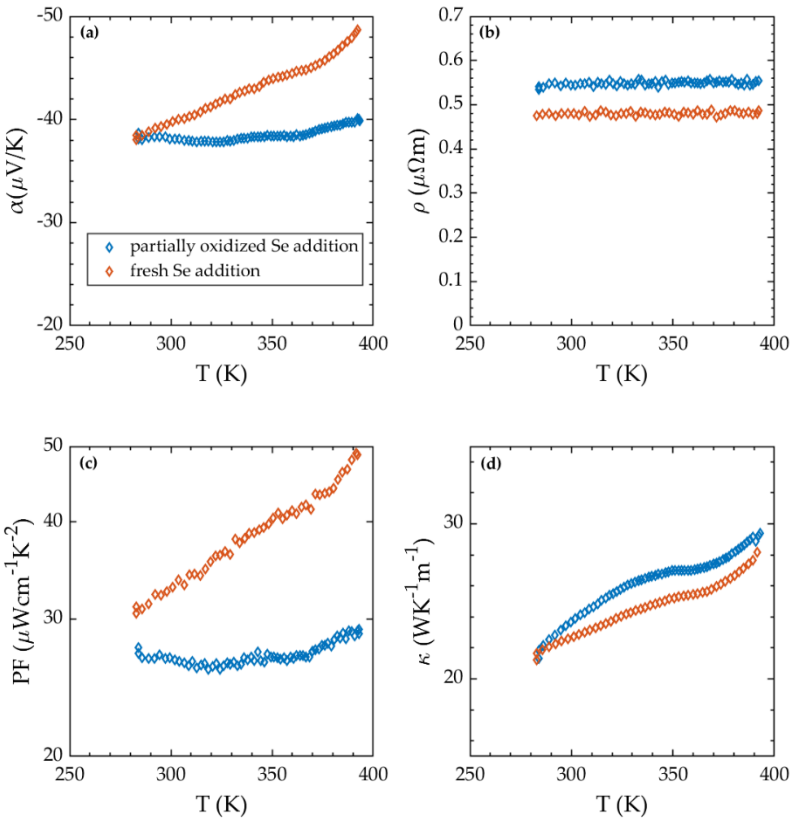

Figure 3-6 (a) Seebeck coefficient, (b) resistivity, (c) power factor, (d) thermal conductivity of $Cu_{65}Ni_{35}$ samples made with fresh and partially oxidized Se powders.

factor between these samples is 68.8%. These results indicate that the added Se powder makes a significant difference in the performance. While the Se was originally added to prevent stickiness during the ball mill process, we note that its addition in fresh form can enhance both the Seebeck coefficient and the TE power factor.

DED samples

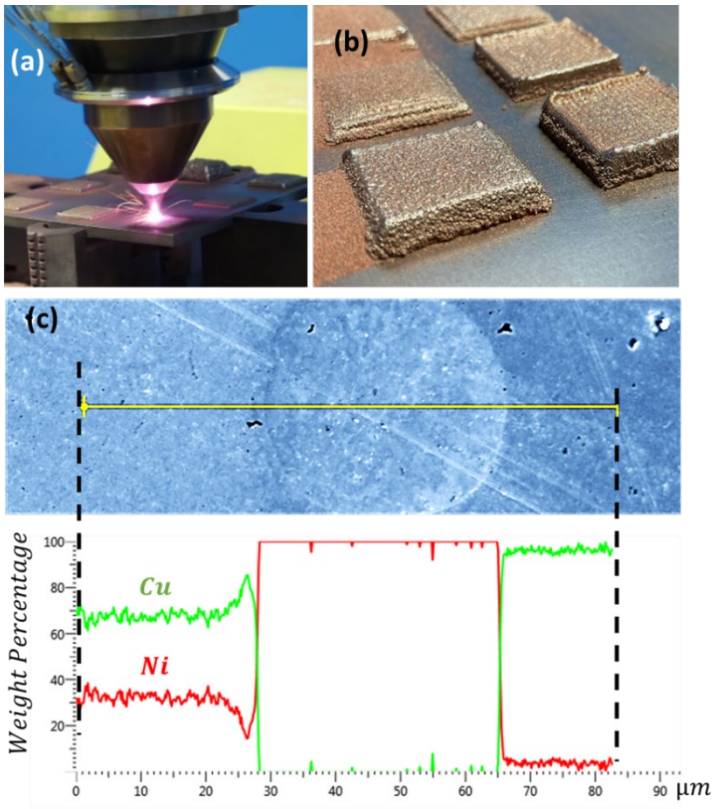

Figure 3-7 (a) DED nozzle flowing Cu-Ni mixed powder and melts them following the program-designed geometry shown in (b). (c) The SEM-EDS results on an area from B1S1 with three different textures: (from left to right) alloyed Cu-Ni region, un-melted Ni particle, and Cu-rich matrix.

As shown in Figure 3-7, the DED process produces heterogeneous texture and cavity in the alloy blocks, which can be explained as follows: The pre-mixed Cu-Ni powder is heated by the laser and melted. A melt pool is formed in which the melted copper and nickel are partially mixed and alloyed. As the laser moves away, the unalloyed liquid cools down to form phase separations. This can be seen from the scanning electron microscope (SEM)-energy dispersive spectroscopy (EDS) results shown in Fig. 5 (c). An EDS line scan is performed across a spherical particle identified inside the DED copper-nickel sample. The spectrum shows that there are three different regions along the line: the alloyed Cu-Ni with

approximately 65-35 composition, the pure Ni particle, and the Cu-rich matrix that surrounds the Ni particle. We see the segregation of copper and nickel and the formation of nickel particles which leaves a rich copper matrix behind. Therefore, while there are areas with uniform alloys, there are also regions inside the DED sample wherein during the scanning of the laser, the temperature distribution was not homogeneous and resulted in inhomogeneity of the samples. The center part of the laser line forms a melting pool directing the formation of the alloy. However, on the edge of the laser spot, the energy received by the mixed powder was not enough to melt the Ni powder. Only Cu powder was melted and formed a Cu-rich matrix. Furthermore, the scanning and the feeding flow of the powder injection are not perfectly aligned and leave vacancies in the lines.

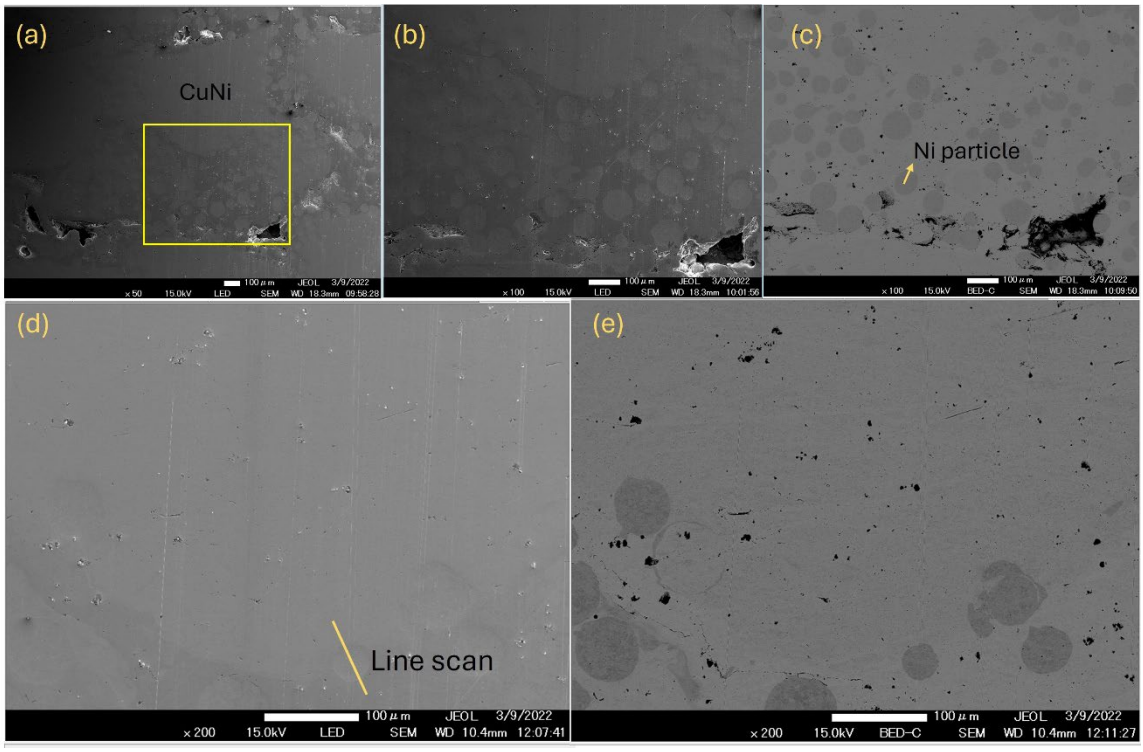

Figure 3-8 secondary and backscattered electron images from DED Cu-NI sample. (b) and (c) are the SE and BSE images of the area marked in yellow in (a). (c) and (d) are the SE and BSE images of the larger area where contains line scanned defects in Figure 3-7(c)

As shown in the SEM SE and BSE images, at a larger scale. The major phase is still Cu-Ni alloy with scattered Ni particles in Cu-Ni matrix. We can confirm the matrix is not Cu particle mixed with Ni particles also using transport properties. The Seebeck coefficient measured for the DED sample is not an average between the Seebeck coefficient of Cu and Ni, instead, it is larger than both parent elements. We speculate that the anisotropy of the DED process could lead to the different phase distributions in the x-y-z direction and therefore lead to the performance difference. The heterogeneous texture of the materials leads to mismatched thermal expansion, which also contributes to the cavity. All these can be further improved in the future by fine-tuning the laser and mixing parameters and by using pre-alloyed powders.

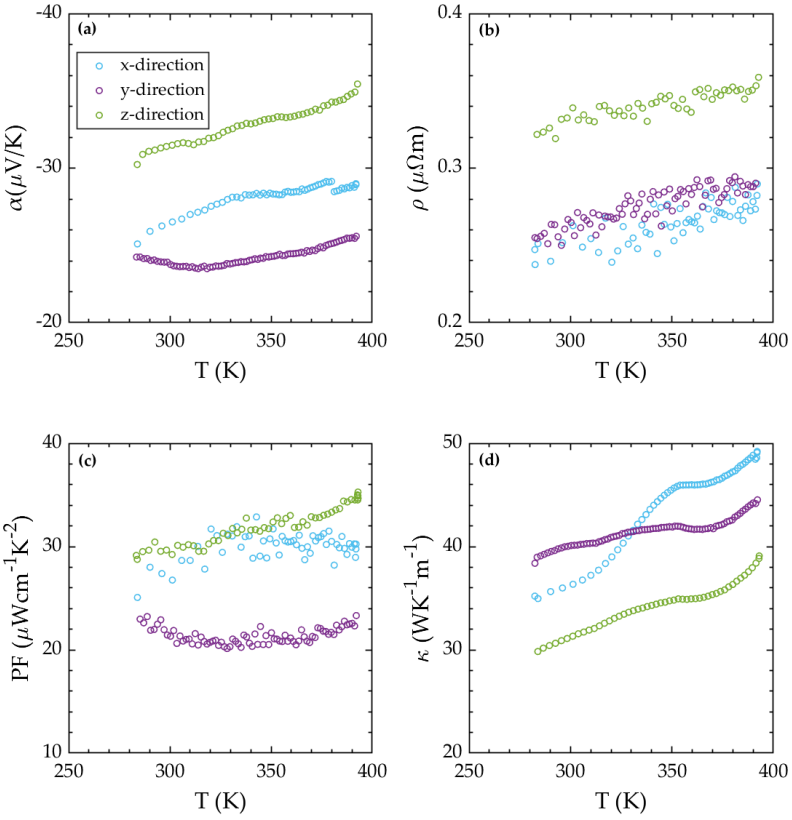

Figure 3-9 (a) Seebeck coefficient, (b) resistivity, (c) power factor, (d) thermal conductivity along x and y (in-plane), z (cross-plane) direction from the same block of the DED sample B1S2.

The DED process features the scanning movement of the powder injection and laser point, and the layer-by-layer stacking of deposited layers, which leads to the anisotropy of the bulk materials. In Figure 3-9, the x and y directions are the in-plane directions in the deposition plane, while the z-direction is the direction of the layer stacking which is perpendicular to the substrate, and we will refer to as the cross-plane direction. The characterization of each direction is performed on a bar-shaped sample cut along the assigned direction. The power factor of the cross-plane direction is larger compared to the in-plane directions. However, the cross-plane direction suffers from the lower thermal and electrical conductivity, which could be resulted from the interfaces between stacked layers.

To compare samples with different DED parameters, bar-shaped ingots were cut and measured along the cross-plane direction. As shown in Figure 3-10, sample B1S1 which has the lowest density also has the largest resistivity and the lowest thermal conductivity. The strategy of reducing the stepover distance with the anticipation that depositing the tracks closer together will allow for complete melting between adjacent tracks which was performed on sample B2S4 seems to be effective. This sample has the largest mass density, electrical, and thermal conductivity. Samples B1S1 and B1S2 are made with the same parameters but their properties are different as their mass density values are very different 8.25 g/cm^3 compared to 8.34 g/cm^3 indicating unintentional variations in the DED process. Compared to the theoretical density of $Cu_{65}Ni_{35}$ alloy at 8.939 gr/cm^3, the DED samples contain 5.4% to 7.7% of pores in volume.

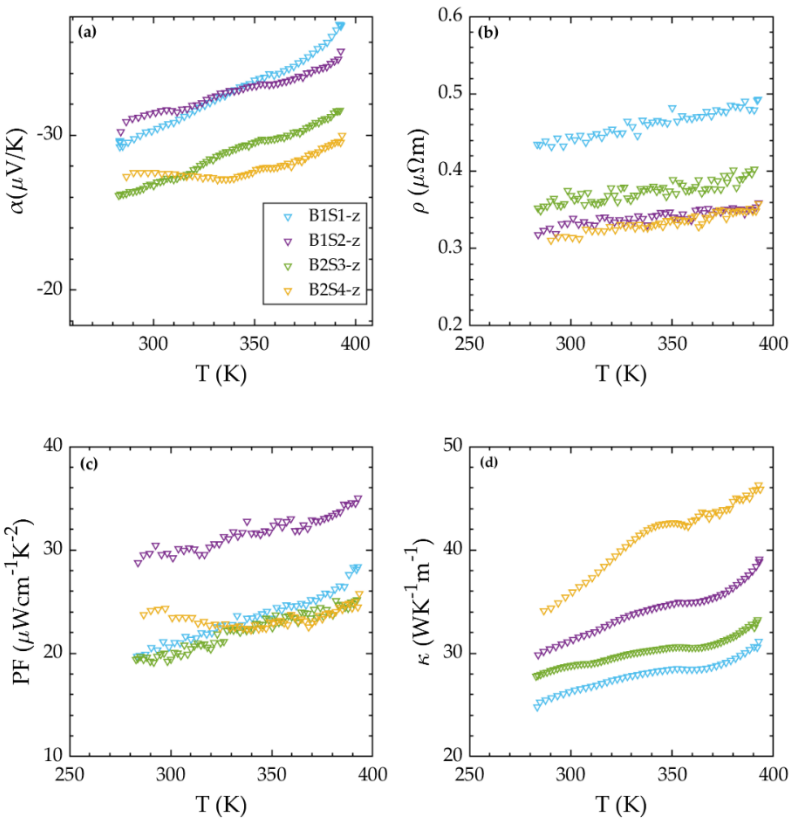

Figure 3-10 (a) Seebeck coefficient, (b) resistivity, (c) power factor, (d) thermal conductivity along x and y (in-plane), z (cross-plane) direction from the same block of the DED sample B1S2.

All DED samples show similar TE power factor values, however, sample B1S2 seems to have a larger TE power factor which we cannot attribute to anything other than fluctuations in the sample fabrication process. This sample is from the same batch as B1S1, but is more uniform and has a higher density, resulting in a 30-40% larger power factor. As discussed before, some parts of DED samples are inhomogeneous and suffer from copper-nickel segregation and some other parts are very uniform and are fully alloyed. Overall, we see that the DED samples are having lower power factors compared to BM-HP samples, however, the best DED sample has a power factor of 31 μW cm^{-1} K^{-2} which is only 11% smaller than the BM-HP sample. The difference in terms of effective thermal conductivity is even lower and is about 5% owing to the higher passive thermal conductivity of the DED

samples. Considering the mixed texture of the DED samples confirmed by SEM-EDS, and the existing porosity, optimizing the DED parameters further might help in terms of the uniformity and higher density of the samples, as well as the increase in the TE power factor.

3.1.4 Conclusion

In this work, we investigated the potential of DED processed Cu-Ni powders for the design of active heat sinks. We showed samples prepared using industrial powders have a similar thermoelectric power factor range compared to the samples reported in the literature made from highly pure copper and nickel powders. The maximum thermoelectric power factor measured in this work is for ball milled-hot pressed samples and is 35 μW cm^{-1} K^{-2} at room temperature. In comparison, the highest power factor reported for Cu-Ni alloys made from highly pure powders is 40 μW cm^{-1} K^{-2} at room temperatures.[97] The corresponding effective thermal conductivity for a 1K temperature difference at room temperature is 172 W m^{-1} K^{-1} and increases to 403 W m^{-1} K^{-1} at 390K. The effective thermal conductivity shows a steep increase with temperature, indicating that these samples can achieve much larger effective thermal conductivity values at higher temperatures. The DED processed samples show sample-to-sample variations, but their overall performance is similar to mechanically alloyed samples. The largest measured TE power factor for DED samples is 31 μW cm^{-1} K^{-2} , but is accompanied by a larger thermal conductivity of 29.23 W m^{-1} K^{-1}. These values correspond to an effective thermal conductivity of 170.18 W m^{-1} K^{-1} at room temperatures which are comparable with reported values for BM-HP samples. The DED process using industrial powders allows large-scale fabrication of these materials at a low cost. The DED process also allows the fabrication of complex geometries

customized and matched to different heat source geometries allowing lowering of the thermal contact resistance and hence efficient heat transfer.

3.2 High Thermoelectric Power Factor in Ni-Fe Alloy for Active Cooling Applications

3.2.1 Background

The Ni-Fe alloys have been studied vastly due to their significance in geology, meteoritic, and material science[98–106]. There are scattered and old studies have reported the Seebeck of Ni-Fe alloys of various compositions and temperature range [57,58,107], showing the peak Seebeck of Ni-Fe alloys can reach -50 μV/K for samples with 53.8%[58] and 40%[57] Ni atom percentage. The gap exists to systematically study the Seebeck coefficient, TE power factor, and the thermal conductivity of Ni-Fe alloys from low temperatures to room temperature range and explore the potential of Ni-Fe alloys to reach high effective thermal conductivity for active cooling applications. This work focused on the power factor performance of the Ni-Fe alloys in the 50-400K temperature range, identified the peak power factor composition range, characterized the microstructure of the as-arc-melted sample, and confirmed the homogeneity of the alloy at microscales.

3.2.2 Experimental and Characterization

Iron powder with 99.5% purity and nickel powder with 99.996% purity were weighted to 5 grams per sample and mixed in an argon-filled glovebox. The powder mixtures were then hot-pressed into solid bulk samples at 800ºC under 56 MPa pressure for 300 seconds using an OTF-1700X-RHP4 hot-press setup from MTI Corporation. The solid bulk samples were later arc-melted to form a Ni-Fe solid solution. Each sample was melted and flipped twice for homogeneity and then melted without flipping allowing bubbles and voids to diffuse to the top of the sample which was then cut out. The central-bottom part of the arc-melted samples were then sectioned into approximately 2mm × 2mm × 10mm bar-shape. Transport performance is performed on the Quantum Design PPMS Versalab. The XRD

characterization is performed using an Empyrean X-ray diffractometer from Malvern-Panalytical on the sectioned as-arc-melted ingots. SEM/EDS is performed on an FEI Quanta 650 Scanning Electron Microscope (SEM).

3.2.3 Result and Discussion

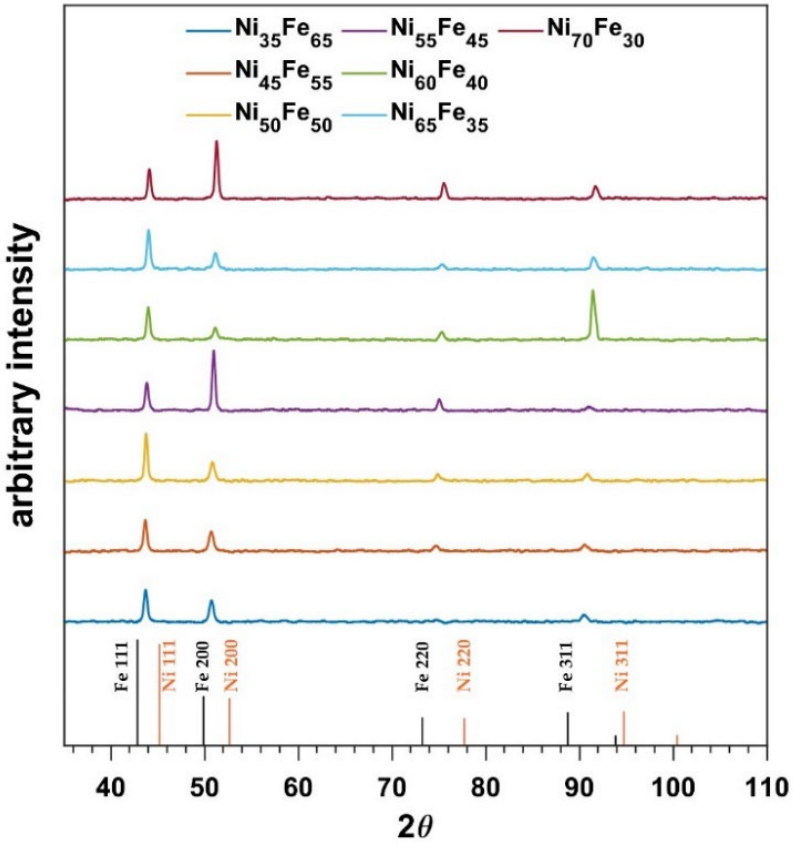

Figure 3-11 XRD results of arc-melted Ni-Fe samples. The black and orange straight lines on the bottom are fcc iron and nickel reference peaks.

Material Characterization

According to the phase diagram, Ni-Fe alloys form a simple face-centered cubic γ-Ni, Fe solid solution within the probed composition range. Due to the slow diffusion of nickel and

iron atoms in this γ-Ni, Fe solid solution[101–104,108], phase separation is unlikely under our experimental conditions.

The X-ray diffraction (XRD) data of all Ni-Fe alloy samples are shown in Figure 3-11. The bulk XRD measurements are performed on the vertical cross-section of the as-arc-melted ingots. Going from bottom to top, Ni concentration in the samples increases. All samples exhibit a consistent series of diffraction peaks, corresponding to the (111), (200), (220), and (311) crystallographic planes of the face-centered cubic (fcc) structure. The variation of intensities of peaks among samples can be attributed to the random distribution of crystal orientation of the the crystal grains at the section surface, which is confirmed by the SEM results. The orange and black lines at the bottom indicate the reference peak positions for pure fcc Ni and Fe. The peaks of the alloys are positioned between the reference peaks for pure Ni and Fe. As the Ni concentration increases, the peaks shift to higher 2θ values, indicating smaller lattice parameters. This trend is consistent with solid solution behavior and reference[109]. The XRD results confirmed that the prepared Ni-Fe samples are single-phase polycrystalline without impurities.

Figure 3-12 presents the backscattered electron image of the vertical cross-section of the as-arc-melted $Ni_{55}Fe_{45}$ sample. The different greyscale regions represent the varying crystal orientations of the grains. At the top of the sample, a prominent needle-shaped bubble is observed, likely formed from the degassing of the powders during the melting process. Several smaller bubbles can also be seen in the upper section of the cross-section. To avoid these bubbles, subsequent transport measurements were performed on samples cut from the central section near the bottom of the arc-melted ingot with the surface layer removed by an abrasive saw, should have varying grain sizes exceeding 10 microns.

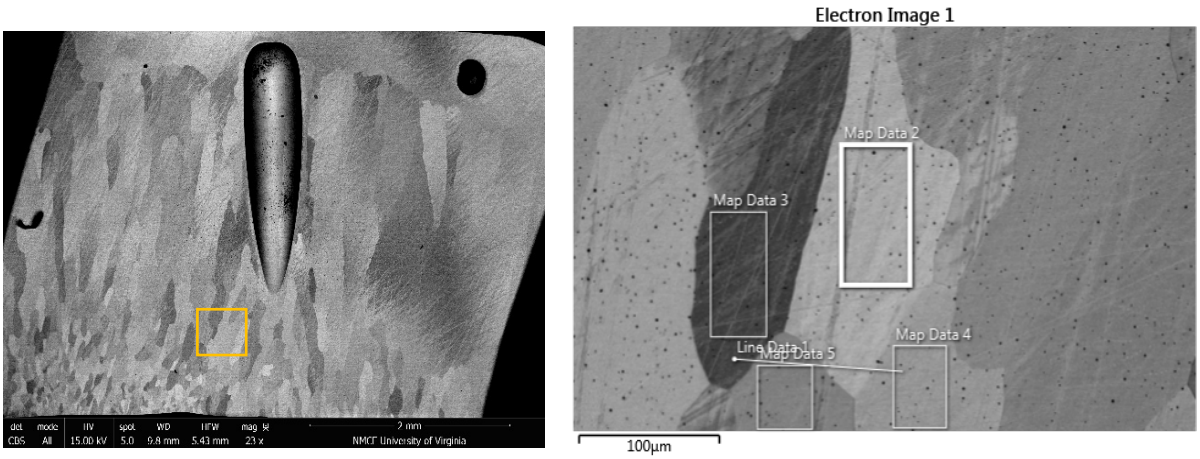

Figure 3-12 SEM backscattered electron image on cross-section of the arc-melted Ni-Fe sample(left), the yellow square marked area is the chosen EDS mapping area. EDS mapping locations on different grains (right).

The SEM image (Figure 3-12) clearly illustrates the distribution of grain size and shape representing the side pieces cut off from the as-melted ingot. The bottom of the sample, which was in contact with the water-cooled copper plate of the arc-melter, experienced a higher cooling rate, resulting in smaller grains (below 100 µm). In contrast, the upper section contains large, elongated grains measuring up to several millimeters. Further EDS mapping of the highlighted area was conducted to characterize the composition of different grains. The black dots visible in the enlarged image are colloidal silica residues from the sample polishing process. The atomic composition data in Table 3-2 confirms the homogeneous composition across the grains, consistent with the stoichiometric ratio of the starting powders. As shown in Figure 3-13, the line scan reveals that the composition remains uniform both within and across grains. Additional SEM/EDS characterizations performed on different samples and in different areas and orientations support that the samples are homogeneous and consistent with the measured composition.

Table 3-2 EDS mapping locations element atomic percentage results

	MapData 2	MapData 3	MapData 4	MapData 5
Ni atom%	54.7	54.3	54.7	54.7
Fe atom%	45.3	45.7	45.3	45.3

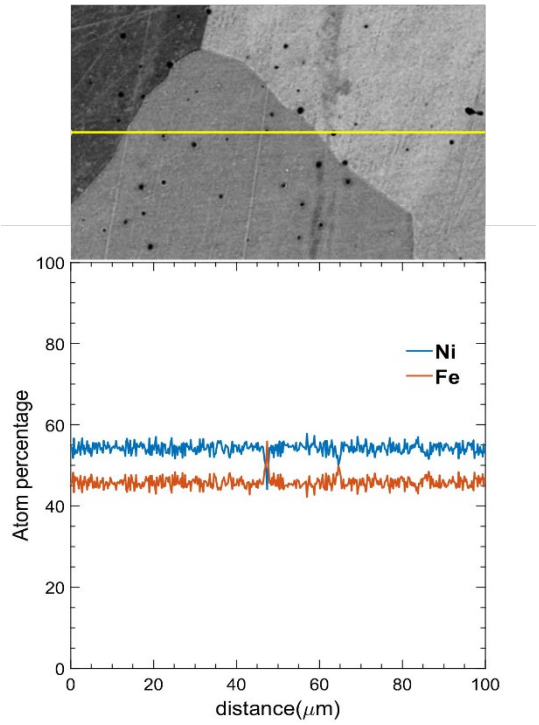

Figure 3-13 EDS line scan across the grains. Location shown in Figure 3-12 as LineData 1

Performance

For the arc-melted Ni-Fe alloy sample with a composition range of 45% to 70% atomic Ni, the absolute value of the Seebeck coefficient is up to 2.5 times greater than that of pure Ni or Fe. The peak Seebeck coefficient varies with composition, with the highest values observed at $Ni_{55}Fe_{45}$ and $Ni_{45}Fe_{55}$, both reaching -52 μV/K. The Seebeck coefficient's dependence on composition also changes with temperature: at lower temperatures (<200K), the absolute value of the Seebeck coefficient decreases with increasing Ni content.

However, this trend does not hold at intermediate temperatures (200K to 400K). previous work[58] observed similar concentration dependence of Seebeck abnormal at higher temperatures and hypothesized the concentration fluctuation as the reason, which is not supported by the SEM/EDS results in this paper. Regarding resistivity, it increases with higher Fe content, consistent with the lower resistivity of pure Ni compared to pure Fe. The resistivities of the Ni-Fe alloys, ranging from 5.60×10^{-8} Ω·m to 7×10^{-7} Ω·m, highlight the highly metallic nature of these alloys. Combining high Seebeck coefficients for alloys with low resistivity, the peak power factor reaches 120 μW/cm·K² for both $Ni_{60}Fe_{40}$ and $Ni_{55}Fe_{45}$. This is 20% higher than the peak values reported at 750K in previous studies on Cu-Ni

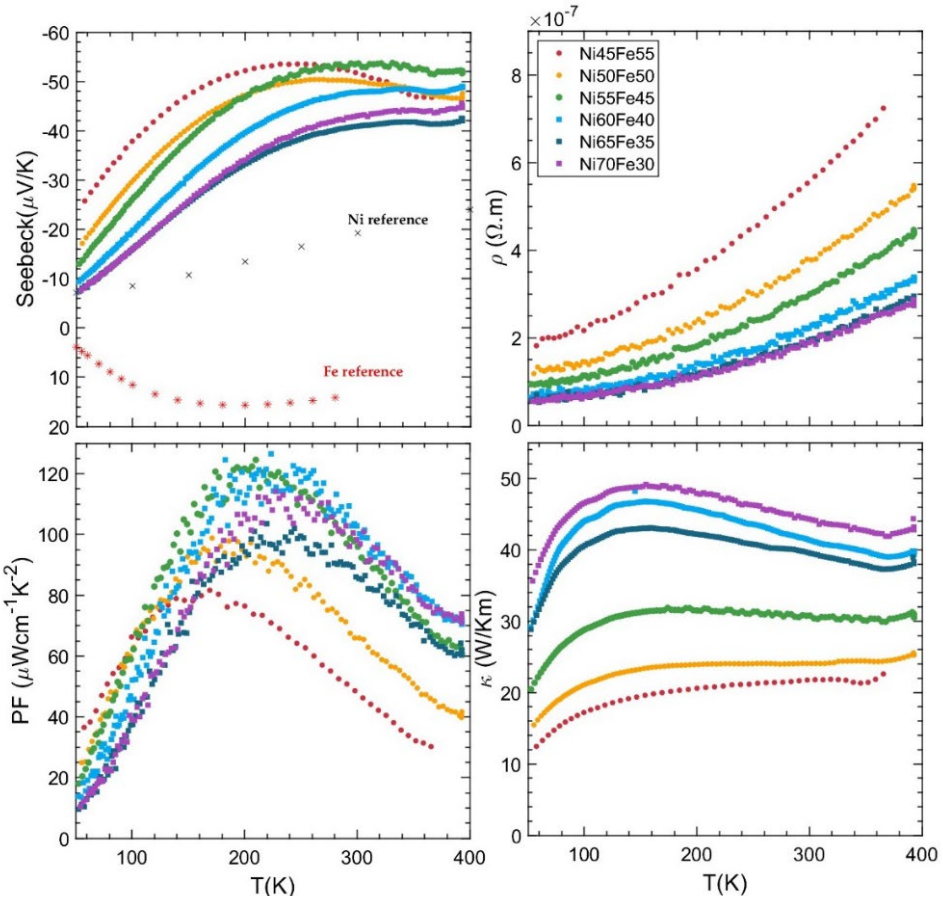

Figure 3-14 (a) Seebeck coefficient, (b) resistivity, (c) power factor, (d) thermal conductivity of Ni-Fe samples. The black and red crosses in (a) are reference Seebeck of pure Ni and Fe

alloys. At 200K, the power factors of $Ni_{60}Fe_{40}$ and $Ni_{55}Fe_{45}$ are comparable to those of the hot-pressed $YbAl_3$ sample, which is well-known for its high power factor. However, the power factors decrease rapidly with increasing Fe or Ni concentration due to the corresponding increase in resistivity and reduction in the Seebeck coefficient, respectively. Since power factor was the primary focus, the Ni-Fe composition range was restricted to 45% to 70% atomic Ni. Thermal conductivity increases with Ni content across the investigated range, except for $Ni_{65}Fe_{35}$, which remains within the margin of experimental error.

As reported in the SEM images, in the arc-melted samples, grains are significantly larger than the typical electron and phonon mean free paths in metals[110–112], eliminating the possibility of grain size influencing thermoelectric properties, especially Seebeck. However, given the limited studies on Ni-Fe alloys as thermoelectric materials, further investigations with improved parameter control are essential to elucidate the role of microstructure in the thermoelectric performance of these alloys.

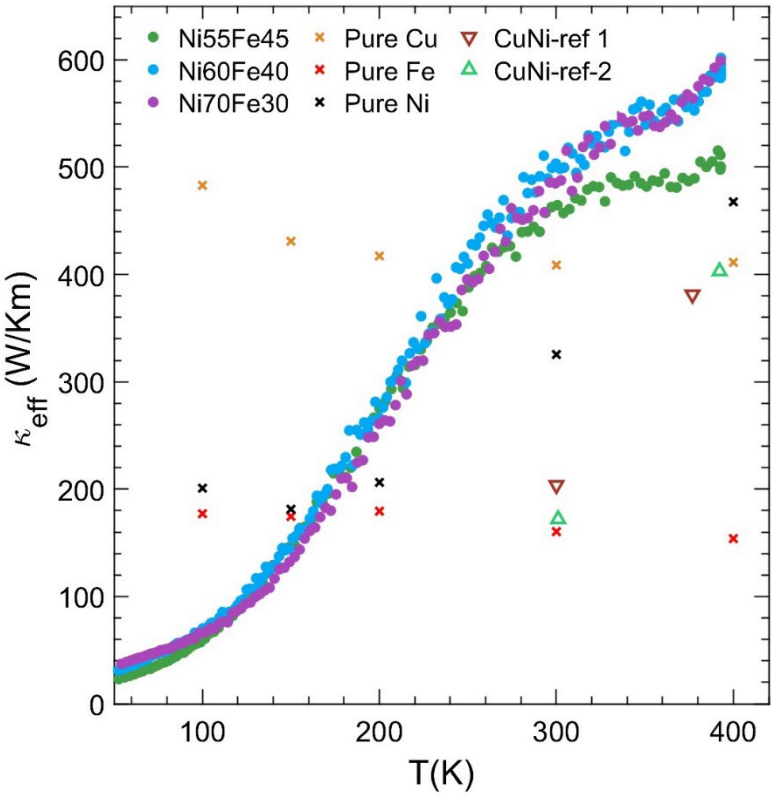

Figure 3-15 Effective thermal conductivity of Ni-Fe alloys comparing with pure Cu, pure Fe, pure Ni, and reference Cu-Ni alloys: twin-boundary enhanced Cu-Ni [55] and ball mill-hot pressed Cu-Ni (3.1)

The effective thermal conductivity (κ_{eff}) of the $Ni_{60}Fe_{40}$ sample exhibits the best balance between power factor and thermal conductivity. As shown in Figure 3-15, the κ_{eff} of the Ni-Fe samples under a 1K temperature gradient is 2 to 3 times higher than the κ_{eff} of pure Fe or Ni in the above 200K range. Above room temperatures, κ_{eff} of the $Ni_{60}Fe_{40}$ alloy is still higher than that of pure copper and previous studies of high power factor Cu-Ni alloys[55,113], reaching 600 W/Km for both $Ni_{60}Fe_{40}$ and $Ni_{70}Fe_{30}$ alloys.

Table 3-3 Comparison of Ni-Fe and Cu-Ni at room temperature

	S(μV/K)	ρ(μΩ·m)	PF(μW/(cm·K²))	κ(W/Km)
$Ni_{60}Fe_{40}$	-47.77	0.22	102.83	41.38
$Cu_{65}Ni_{35}$	-33.95	0.38	30.12	32.75

At room temperature, the arc-melted $Ni_{60}Fe_{40}$ sample is better in all active-cooling-related aspects than the arc-melted $Cu_{65}Ni_{35}$ sample in the previous study. If we compare the pure elements, copper has the lowest resistivity, then nickel, then iron. In addition, copper and nickel are closer in their electronegativity and electron affinity suggesting a smaller alloy scattering. Therefore, it is surprising that the copper-nickel sample has a larger resistivity, and a lower conductivity compared to nickel-iron. While more detailed studies are needed, possible explanations could be the presence of other impurities and defects in Cu-Ni.

Compared to Cu-Ni, and Au-Ni we cannot speculate Seebeck of the Ni-Fe alloy can be attributed the same s-d inter-band scattering model without a valid band structure calculation, due to the difference in the band structure of copper and iron near the Fermi level.

In a metal, the diffusive Seebeck coefficient is obtained from the Mott equation and is proportional to the slope of DOS divided by DOS at the Fermi level. The Seebeck of Ni-Fe is larger than pure Ni, pure Fe, and Cu-Ni. Part of this could be the result of a larger slope of DOS for Ni-Fe compared to other candidates which needs to be confirmed using first-principles calculations. In pure elemental nickel and iron, a contribution from magnon-drag[52] is suggested a linear dependence of Seebeck on the factor of $\left(\frac{T}{T_c}\right)^{3/2}$. Considering the curie temperature of γ-Ni_xFe_{100-x} alloys increases with increasing Ni concentration until $x>70$, and the drop of low temperature absolute Seebeck value with the increasing Ni in our Ni-Fe samples, it is possible that Ni-Fe alloy also exhibits magnon-drag Seebeck coefficient. This term will be additive to the diffusive Seebeck coefficient.

A band structure calculation, magnetic property measurement, and Hall measurement to determine carrier concentration should be performed on a high-quality sample in the future to help us understand the contribution of these two mechanisms.

3.2.4 Conclusion

The power factor and effective thermal conductivity of arc-melted Ni-Fe alloys with 45 to 70 atomic percent nickel were investigated over the temperature range of 50K to 400K. Notably, the $Ni_{55}Fe_{45}$ and $Ni_{60}Fe_{40}$ alloys demonstrated an optimal peak power factor of 120 $\mu W/cm \cdot K^2$ at 200K, an impressive value for stable alloys composed of cost-effective and abundant elements. his value is larger than any other binary metal reported in the past at 200K. The effective thermal conductivity, κ_{eff}, at a 1K temperature difference was also calculated using the measured values of passive thermal conductivity and TE power factor. The largest κ_{eff} values exceeding 600 W/K·m at 400K were observed for $Ni_{60}Fe_{40}$ and $Ni_{70}Fe_{30}$ alloys outperforming pure copper, Ni, Fe, and state-of-the-art Cu-Ni alloys under the same conditions. The microstructure of the arc-melted Ni-Fe ingots was characterized using SEM and EDS, providing insights into grain size and elemental distribution. The abnormal composition dependence of the absolute Seebeck coefficient at intermediate temperatures (200K-400K) was also noted. A hypothesis suggesting that local concentration fluctuations account for this anomaly was tested using EDS analysis, which invalidated this explanation. Further research is needed to assess the effects of grain size, magnetic domains, single crystals, and defects on the thermoelectric performance of Ni-Fe alloys. The maximum power factor for this system remains to be determined. This study reveals the overlooked potential of Ni-Fe alloys for high-power factor applications, highlights the promise of transition metal alloys in the search for high power factor metallic

materials, and encourages further research into metallic thermoelectric materials for active cooling.

3.3 Other Attempts

3.3.1 Chromium-Iron alloy

A trial on the same composition is made using industrial-level chromium powder and high-purity manganese powder. The same ball milling and hot pressing process as the Cu-Ni BM-HP samples are used to make the $Cr_{0.9}Mn_{0.1}$ samples. Three samples with the same composition are made and tested for the performance. However, the three samples show inconsistency with the reference and the samples. The contamination from the stainless

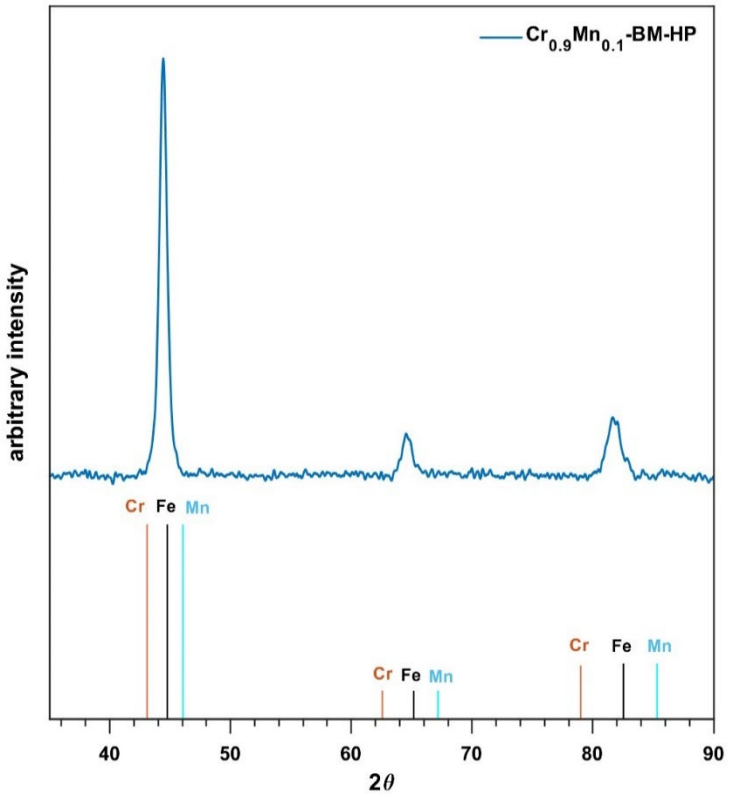

Figure 3-16 XRD of ball milled-hot pressed $Cr_{0.9}Mn_{0.1}$. The orange, black and cyan straight lines are reference peaks for pure Cr, Fe, and Mn

steel jar is suspected to have altered the composition of the ball-milled sample causing the deviation of Seebeck performance from the reference[59], Similar effects were also observed in other mechanical alloying study of Cr-based alloys in steel jars.[114]

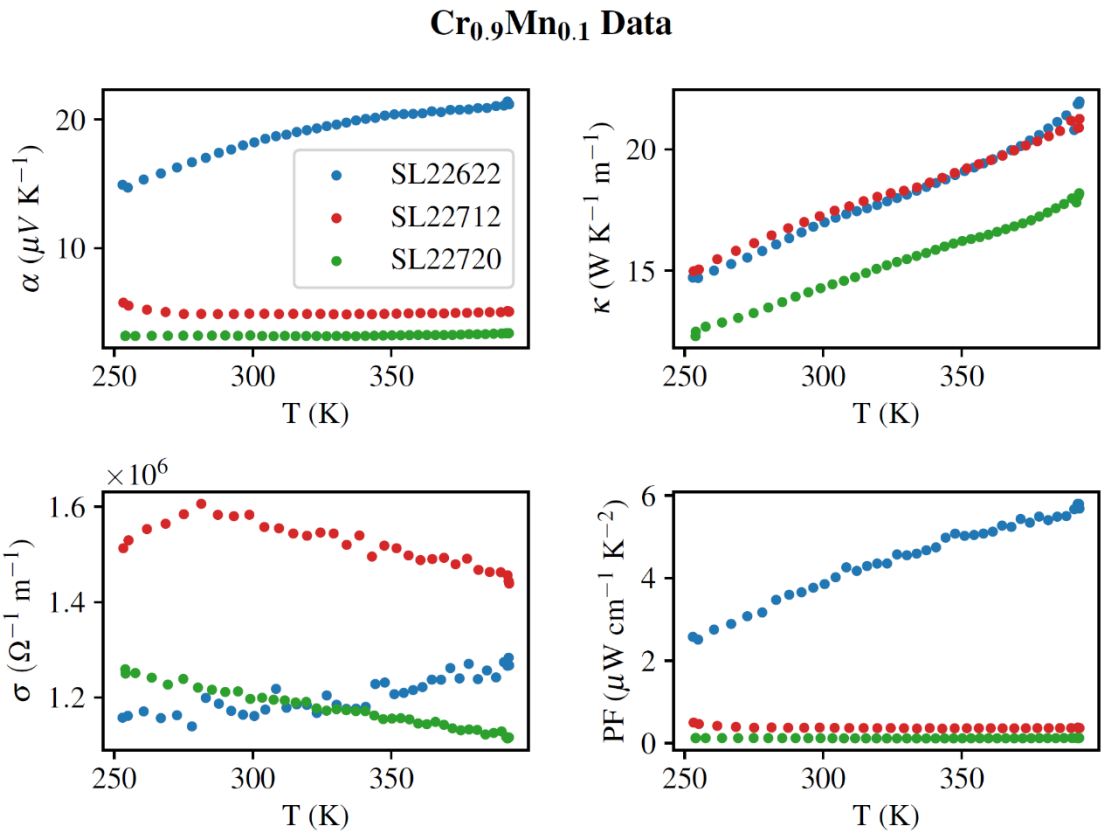

Figure 3-17 (a) Seebeck coefficient, (b) resistivity, (c) power factor, (d) thermal conductivity of three $Cr_{0.9}Mn_{0.1}$ sample. All the sample are prepared in the same way, the SL22622 just labels the sample preparation date.

3.3.2 Nickel and Cobalt based Alloys

Solid solution alloys of Sn, Al in Co, and Sn in Ni are made via hot-pressing and then arc-melting just like Ni-Fe alloys. 1% of Sn and Al alloying are chosen to test the dilute alloys, and 7% of Sn is chosen to approach the solubility limitation of Sn in Co and Ni at 1000K. The performance is shown in Figure 3-18. The Seebeck of the dilute solid solution alloys are worse or barely better than the pure metal.

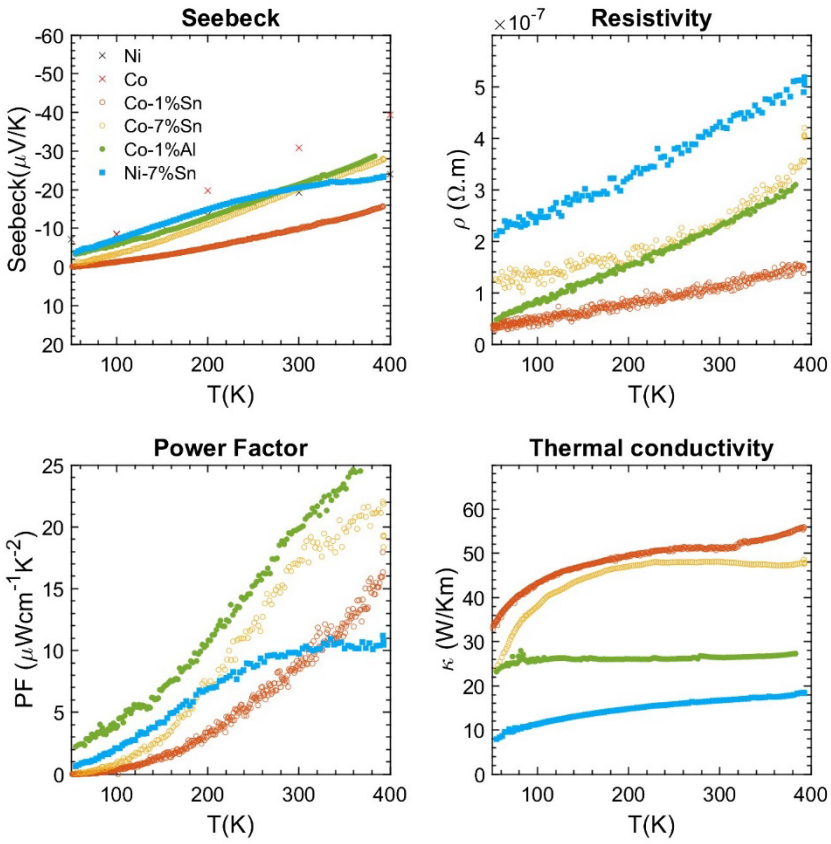

Figure 3-18 (a) Seebeck coefficient, (b) resistivity, (c) power factor, (d) thermal conductivity of other Ni- and Co-based samples.

3.4 Summary and Prospects

In this section, the compositions of binary nickel alloys with copper and iron are optimized to achieve a desirable effective thermal conductivity. The thermopower of the inter-soluble solid solution of nickel benefits from possible three distinct mechanisms arising from its valence electron configuration: diffusive contribution from the slope of DOS near the fermi level, diffusive contribution from the inter-band scattering that improves the Seebeck value without scarifies the electron mobility significantly, and the magnon-drag contribution from the magnetism. Although the performance and the potential of the Ni-based alloys for active cooling are clearly shown in the phenomenal observations in my work. The physic

aspect of the performance still awaits in-depth study. For Cu-Ni system, the ball-milled process is introduced in previous study aiming enhance ZT by nano structuring, which should not benefit effective thermal conductivity in the same level due to the trade-off of the lowered electrical and thermal conductivity. Systematic studies on high quality sample with microstructure that benefit electron and phonon transport should further optimize this system for effective thermal conductivity. For Ni-Fe system, the mechanism that dominates the Seebeck value contribution remains unclear, future studies on Seebeck in high quality even single crystal samples and related first-principle calculation should reveal more details on the contribution from different mechanism. Based on the dominate mechanism, attempts should be made to further improve the effective thermal conductivity. Ultimately, developing robust methodologies to guide material selection and performance enhancement for high effective thermal conductivity alloys will be as critical as those established for high-ZT thermoelectric materials.

4. Intermetallic Approach

Intermetallic compounds with high power factor potentials are Half-Heusler alloys[115–120] and rare-earth compounds[65]. Half-Heusler alloys are prized for their high figure of merit, attributed to their elevated thermopower and relatively low thermal conductivities (~4 W/m·K) within the metallic materials. Certain rare-earth compounds consisting of cerium and ytterbium compounds[61–64] achieve remarkable power factors due to their extraordinarily high Seebeck coefficients. $YbAl_3$, for instance, remains a top-performing material with a high power factor across a wide temperature range (200K-400K)[5,63–65]. A study of its band structure[68] uncovers a sharp density of states (DOS) singularity near the Fermi surface. This phenomenon may be linked to the proximity of the 4f-level to the chemical potential[68] and the resulting Kondo resonance[65]. Nonetheless, $YbAl_3$ falls short in terms of its figure of merit due to a relatively high total thermal conductivity, around 10 W/m·K, which contrasts with materials with glass-like thermal conductivity ($\kappa_L < 1$ W/m·K) and half-Heusler alloys ($\kappa \sim 4$ W/m·K). Nevertheless, the $YbAl_3$ example suggests that Yb-based compounds could feature a sharp DOS singularity near the chemical potential, potentially resulting in a high power factor. Yb-Ag and Yb-Zn intermetallic compounds are tested in this study. The investigation on $YbZn_{11}$ is presented below.

4.1 Thermoelectric Properties of $YbZn_{11-x}Al_x$

4.1.1 Background

In metals, the Mott Formula[121] relates the Seebeck coefficient to the slope of the density of states (DOS) at the Fermi level. For metals, therefore, a sharp peak of the DOS near the Fermi level indicates the potential of a high Seebeck coefficient. [5,122–124] Some of the Yb-based intermetallic compounds show such features according to first-principles

calculations. A good example is $YbAl_3$ which has a sharply peaked DOS due to the f-orbitals and as a result, has a record high thermoelectric power factor. [65] $YbZn_{11}$ is another candidate in this class of materials. Since its crystal structure was first reported in 1966[125], $YbZn_{11}$ has received little attention. Apart from a few studies that mention it while exploring the phase space of related systems[126,127], the only paper discussing its inter-band interaction dates to 1998[128]. Moreover, the thermoelectric properties of $YbZn_{11}$ have never been thoroughly examined or reported.

The expected sharp peaks in the DOS of several intermetallic Yb-based compounds are confirmed within the Topological Materials Database[129–132] band structure calculations. [65,123,125] Similarly, in $YbZn_{11}$, a sharp peak of DOS near the Fermi level is shown in the topological materials database which in principle should result in a large Seebeck coefficient as evidenced by the Mott equation. However, this material is rarely studied, and its thermoelectric properties have never been reported. To assess the guidance provided by computational results and investigate the unreported thermoelectric properties of the materials, we synthesized $YbZn_{11}$. Here, we report structural characterization and assessment of defects, followed by intrinsic thermoelectric properties. Finally, we explore avenues to enhance the thermoelectric performance using doping.

4.1.2 Experimental and Characterization

Experimental Methods

Sublimed Yb pieces with 99.9% purity and 99.999% zinc shot were mixed to the stoichiometry of $YbZn_{11}$. The mixed pure metals were loaded into a fused quartz glass tube. The tube was evacuated and backfilled with Argon three times, then sealed. The sealed ampoule was heated up to 890ºC to melt the metal for 16 hours, then kept at 760ºC for 16

hours. After cooling down the ingot is ground into powder with mortar and pestle. Ball-milling was not attempted due to the reactive nature of ytterbium. X-ray Diffraction (XRD) was performed on powders and hot-pressed samples to confirm the formation of the compound. Al was used to substituting Zn to adjust the Fermi level. 99.999% aluminum powder and wires were added according to stoichiometry. The intrinsic and $YbZn_{10.7}Al_{0.3}$ samples were annealed at 650ºC in a sealed tube for 24 hours, to improve the Al distribution and substitution. For each sample around 2.5 grams of the product powder was loaded in a graphite die, with graphite paper covering the inner wall and the interface between the powder and the pushing rod to prevent sticking. The powders were then hot-pressed at 650ºC under 56 MPa pressure for 300 seconds using an OTF-1700X-RHP4 hot-press setup from MTI Corporation. The hot press chamber was filled with argon gas during the process. A disc-shaped solid sample with a diameter of 12.7 mm was obtained after polishing the hot-pressed ingot. The disc-shaped sample was then cut by a Mager BR220 precision cut-off saw into bar-shaped samples with approximate 2mm × 2mm × 10mm dimensions. Transport performance is performed using the Quantum Design PPMS Versalab. The XRD characterization is performed using an Empyrean X-ray diffractometer from Malvern-Panalytical on a pressed disc sample. Imaging is performed on an FEI Quanta 650 Scanning Electron Microscope (SEM).

Computational Methods

The computational part was carried out by Ruhul Quddusb and Sree Sourav Das from UVa. $YbZn_{11}$ crystallizes in a tetragonal I41/amd space group with 2 Yb and 22 Zn atoms in the unit cell. The lattice parameters were nominally a=b=10.66 Å and c=6.383 Å from the topological materials database1. First-principles calculations were performed using the

density functional theory (DFT) as implemented in the QUANTUM ESPRESSO package.[133] We used Perdew-Burke-Ernzerhof generalized gradient approximation (PBEsol)[134] pseudopotential for Zinc (Zn) and Wentzcovitch (PAW) pseudopotential[135] for Ytterbium (Yb). Scalar relativistic pseudopotentials were used throughout the calculation as we found no spin-orbit coupling (SOC) effects on electronic band structure as shown in supplementary information Figure S2. The electronic structure calculation employed a kinetic energy cutoff of 60 Ry with a charge density cutoff of 320 Ry and a Monkhorst-Pack k-point mesh of 8×6×6. The atomic positions were relaxed through the Broyden–Fletcher–Goldfarb–Shanno (BFGS algorithms). The convergence threshold of energy was set to 4.8×10-9 Ry in the self-consistent calculation. A Gaussian smearing value of 0.01 Ry was chosen during the calculations. Finally, the Seebeck coefficient was evaluated using the BoltzTraP package.[136] BoltzTraP solves the Boltzmann Transport Equations (BTE) under constant relaxation time approximation.[136] Within the constant relaxation-time approximation, the Seebeck coefficient can be obtained directly from the electronic structure without any adjustable parameters, and it is expressed in the following equation:

$$S_{\alpha B}(T,\,\mu) = \frac{1}{eT\Omega\alpha_{\alpha\beta}(T,\,\mu)}\int \sigma_{\alpha\beta}(\varepsilon)(\varepsilon - \mu)\left[-\frac{\delta f_0(T,\,\varepsilon,\,\mu)}{\delta\varepsilon}\right]d\varepsilon \qquad (4-1)$$

where Ω is the cell volume, e is the electron charge, μ is the chemical potential, ε is the electron energy, and T is the absolute temperature. f_0 is the equilibrium Fermi-Dirac distribution function and $\sigma_{\alpha\beta}$ is the transport distribution tensor with α and β as the tensor indices indicating the crystallographic directions. $\sigma_{\alpha\beta}(\varepsilon)$ is also referred to as the differential conductivity and is $\sigma_{\alpha\beta}(\varepsilon) = v_g^2\tau(\varepsilon)g(\varepsilon)$, where v_g is the group velocity, τ is the scattering time, and $g(\varepsilon)$ is the DOS. Under constant relaxation time approximation

used here, $\tau(\varepsilon) = \tau_0$ and is a constant and the elements of conductivity tensor are calculated using the Fourier interpolation of the band structure only.

4.1.3 Result and Discussion

Material Characterization

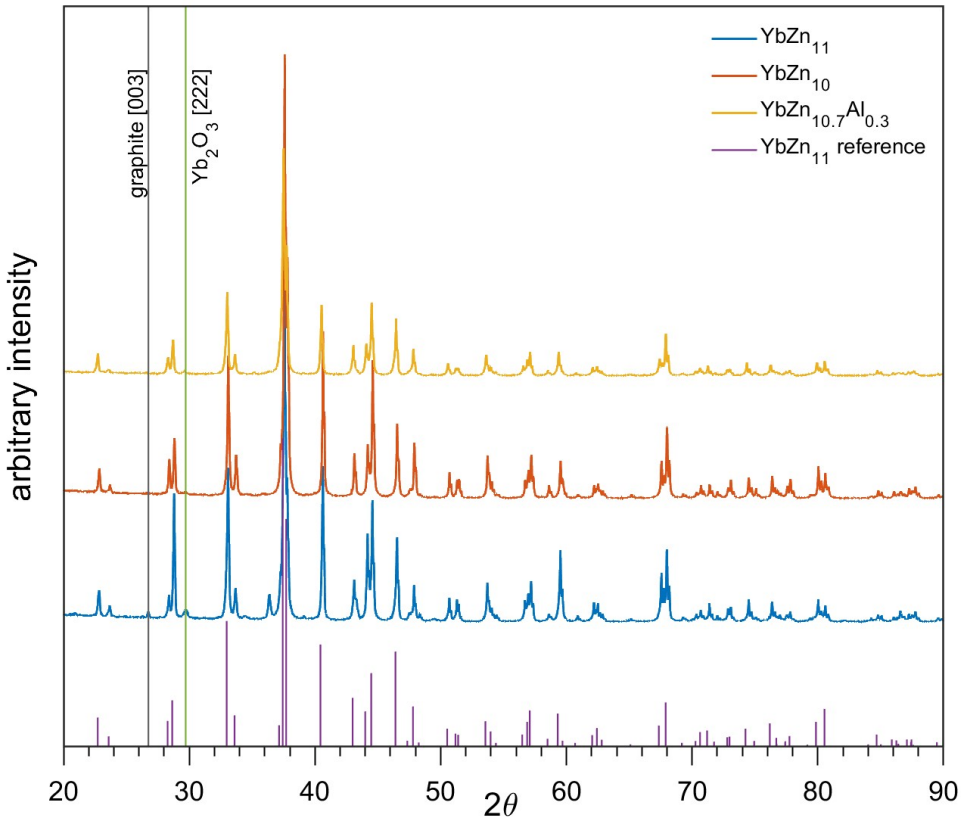

Figure 4-1 XRD results of Yb-Zn samples, annealed intrinsic $YbZn_{11}$ sample in blue, Zn-deficient sample YbZn10 sample in orange, and Al-substitution sample $YbZn_{10.7}Al_{0.3}$ in yellow, and the reference peaks in purple. Minor impurity peaks from graphite and ytterbium oxide are marked by black and green lines.

The XRD results of three representative samples are shown in Figure 4-1. Note that in the patterns of $YbZn_{11}$ and $YbZn_{10.7}Al_{0.3}$, two minor peaks of graphite and Yb_2O_3 can be identified. The graphite peak comes from the residue of graphite paper during the hot press process and only exists at the surface. The residue can stay in small cavities during the polishing process. The oxide peaks may result from residual oxygen in the sealing process.

All the relevant samples show excellent correspondence in XRD of the synthesized material with the standard diffraction pattern for $YbZn_{11}$ and the impurities only appear in small volume fraction as indicated by the few identifiable minor peaks in XRD.

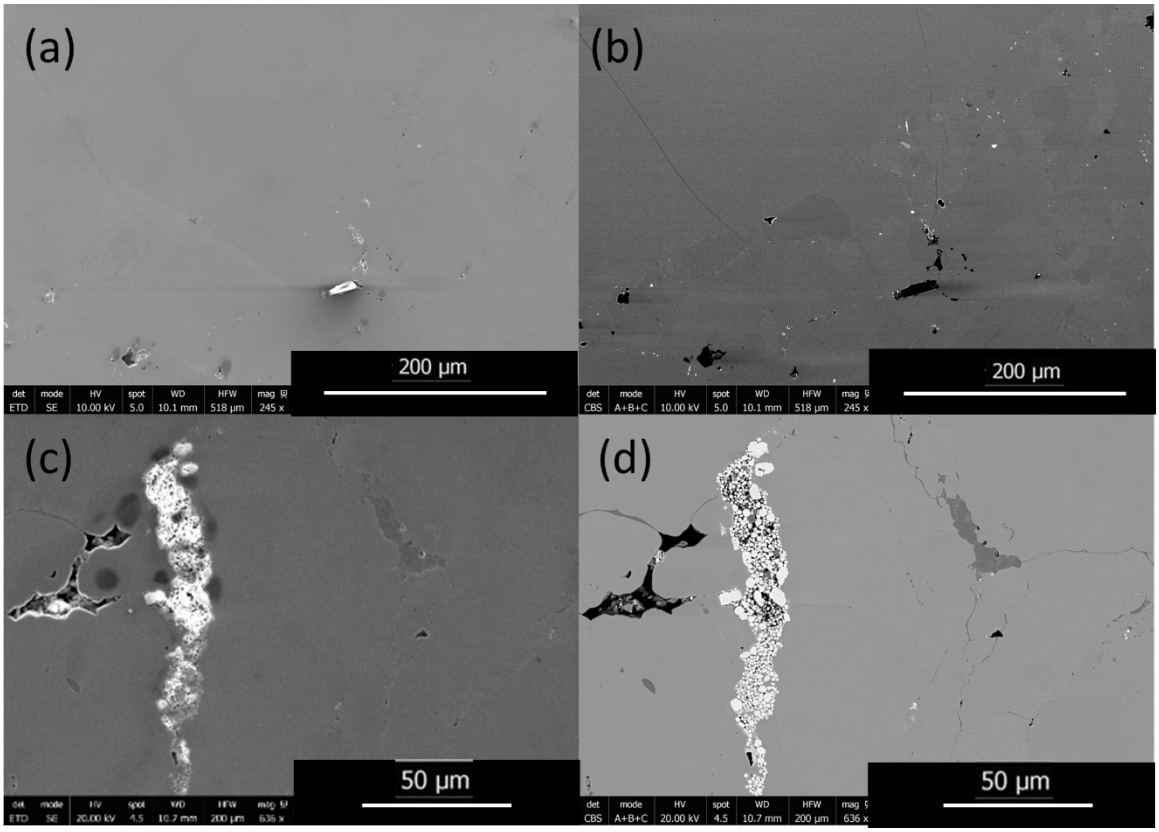

Figure 4-2 (a) and (b) are the secondary electron (SE) image and back-scattered electron (BSE) image of YbZn11 sample at a larger scale (with a scale bar of 200µm) at the same site. The bright feature shown in SE image (a) is charging from a glass fragment coming from the synthesis process, which can be confirmed by the fact that the BSE image shows a low electron count from back-scattering, indicating low mass elements. (c) and (d) are SE and BSE images at higher magnification (scalebar of 50µm) on typical defects.

SEM micrographs from the $YbZn_{11}$ sample in Figure 4-2 show the typical defects in these Yb-Zn intrinsic samples. Figure 4-2(a) and (b) show the secondary electron (SE) image and back-scattered electron (BSE) image of the $YbZn_{11}$ sample with a scalebar of 200 µm. Shown as the extended light grey area in the BSE image, $YbZn_{11}$ constitutes the majority of material corresponding well with the XRD results. With higher magnification, (Figure

4-2(c) and (d), SE, and BSE respectively) the impurities in the microstructure can be identified. Typical defects are pores (black), Yb-rich (white), and Zn-rich (dark grey).

The samples are sintered from hand-milled powders. The intrinsic limitation of this sintering process results in minor retained porosity, as shown in the BSE images. This observation is confirmed by the SE image, which illustrates the morphology. The mass density of the $YbZn_{11}$ sample is measured to be 98% of the theoretical density indicating the presence of some pores. Small Yb pieces that remained un-melted during the melting process or precipitated after cooling down oxidized post-process, exhibiting higher

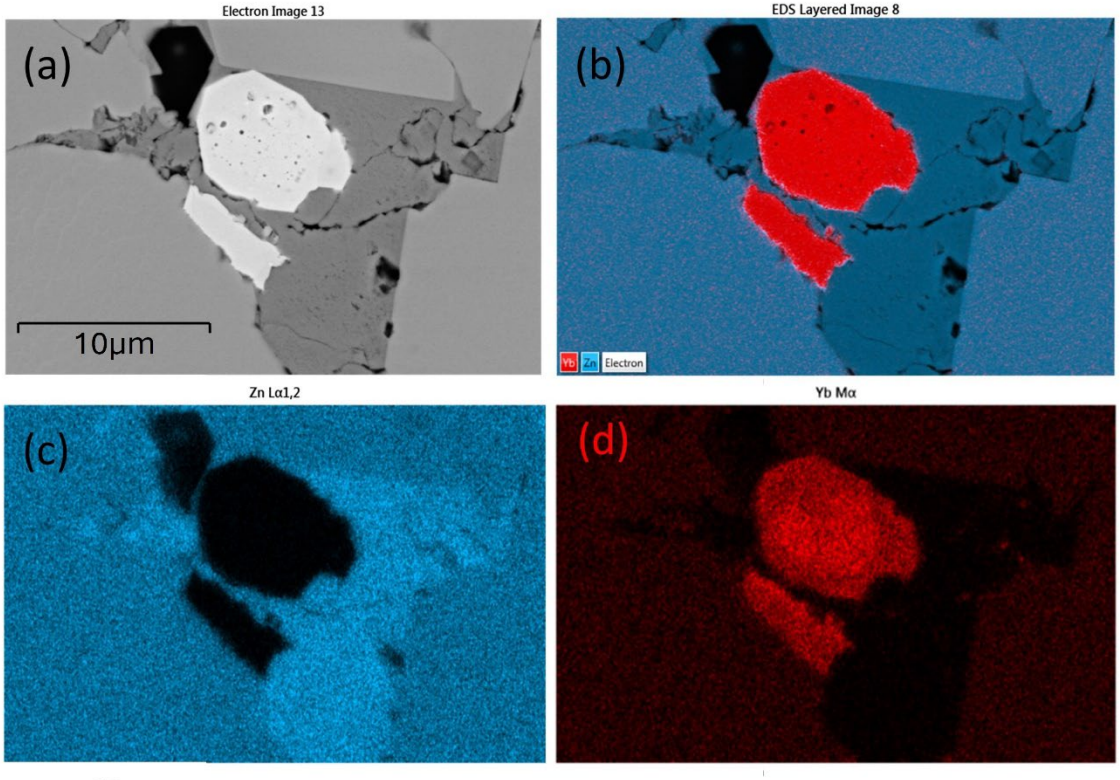

Figure 4-3 EDS mapping. (a) BSE image of a typical defect site with cavities (black), Yb oxides (white), Zn (dark grey), compared to YbZn11 (light grey). (b) layered EDS map, (c) Zn distribution EDS map, (d) Yb distribution map. The blue and red dots density in (c) and (d) represent the relative Zn and Yb concentration

brightness in the SE image due to the charging effect and in the BSE image owing to their higher relative mass.

In EDS mapping mode, the distribution of the elements can be demonstrated clearly as shown in Figure 4-3, All three types of defects: cavity(pores), Yb-rich, and Zn-rich phase are shown in one site. In Figure 4-3(b), Yb-rich, Zn-rich, and the pure $YbZn_{11}$ phases are identified by the red, dark blue, and blue areas, respectively. Figure 4-3 (c) and (d) show that the defects are caused by unreacted Yb and Zn. The dark grey area in Figure 4-3(a) shows a higher Zn concentration as confirmed in Figure 4-3(c) and near-zero Yb concentration as confirmed in Figure 4-3(d), indicating the existence of the Zn-rich phase. Similarly, the white area in Figure 4-3(a) seems to be majority Yb with almost no Zn. Here we postulate that these small defects are ytterbium oxide considering the reactivity of Yb, Yb_2O_3 peaks in XRD, and the charging effect of this kind of defect under the electron beam. Further EDS line scan on the same site crossing all separate phases as shown in Figure 4-4 confirms the weight percentage of Yb and Zn in these phases. The main matrix shows the correct weight percentage of Yb and Zn for $YbZn_{11}$, combined with XRD results and EBSD results in Supplementary, the major matrix is confirmed to be $YbZn_{11}$.

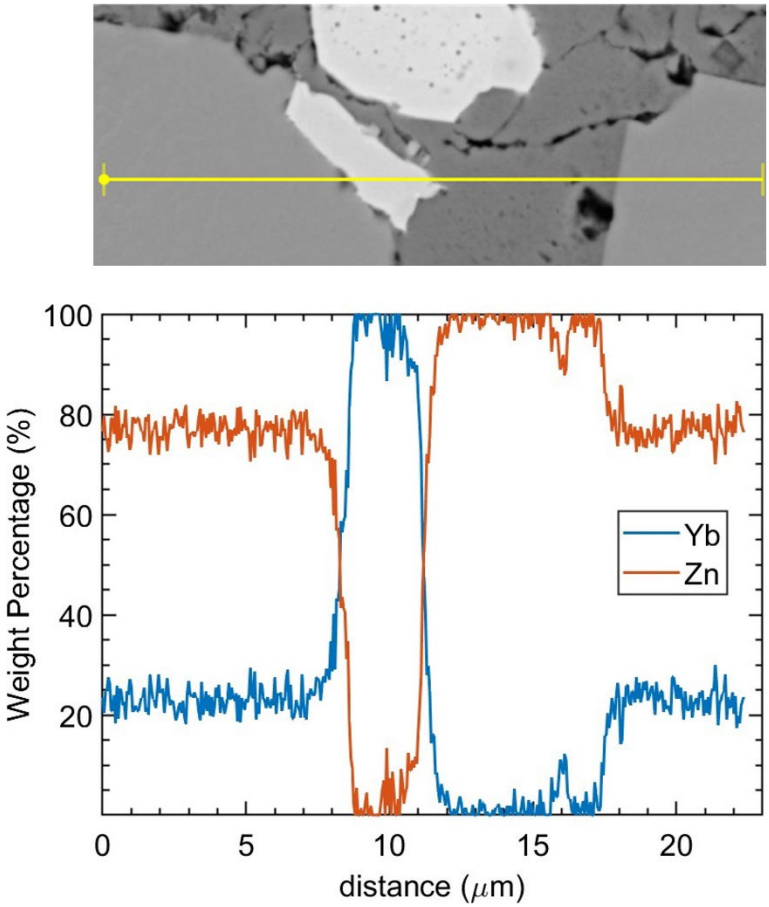

Figure 4-4 EDS line scan on the defect site. The scanning line goes through $YbZn_{11}$ matrix, Yb oxides (white), Zn-rich phase (dark grey), and $YbZn_{11}$.

Combining XRD and SEM results, the micron-sized oxide with extremely small volume fraction primarily appears in cavities. Considering the extended grain size of the $YbZn_{11}$ crystals, (Figure 4-5), we believe the scattered oxide impurities should not significantly affect the overall transport properties nor the overall thermoelectric performance of macroscopic samples.

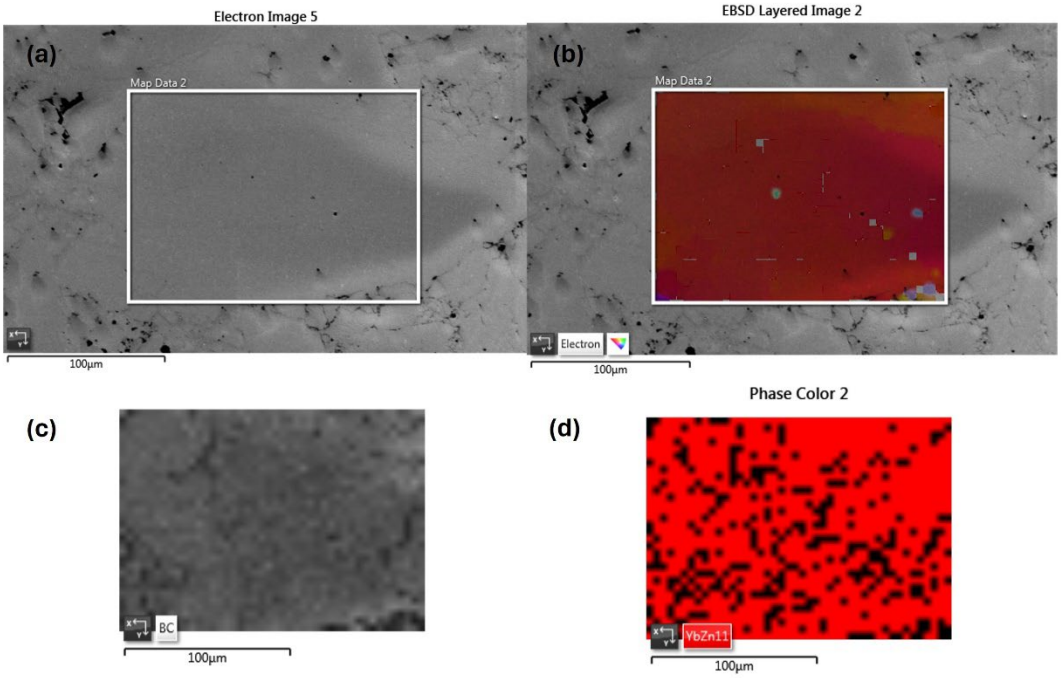

Figure 4-5 Electron Backscatter Diffraction(EBSD) results on $YbZn_{10.7}Al_{0.3}$, (a) electron image, (b) EBSD layered image, (c) Band contract image, (d) Phase color mapping. The red area indicates $YbZn_{11}$ diffraction (Kikuchi bands patterns) identified.

Band Structure Calculations

The electronic band structure and electronic density of states (DOS) calculated for intrinsic $YbZn_{11}$ are shown in Figure 4-6. The band structure is shown in Figure 4-6(a) along high

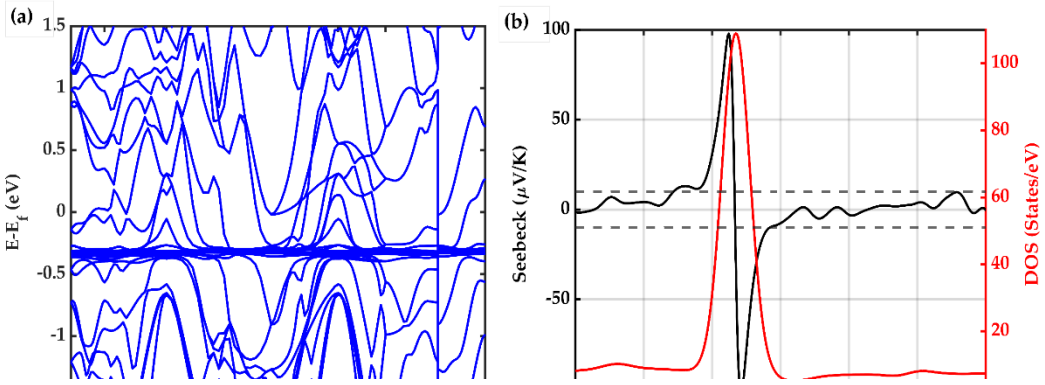

Figure 4-6 . (a) Electronic Band Structure and (b) Seebeck and Density of States of $YbZn_{11}$.

symmetry direction P(0.25,0.25,0.25)-N(0,0.50,0)- Γ (0,0,0)-M1/M(-0.50,0.50,0.50)- Γ - X(0,0,0.50)- P/M(0.50,0.50,0.50)- X1(0,1.00,0.50). The obtained DFT band structure and the DOS are in good agreement with previous calculations shown in the Topological Materials Database.[129] The density of states has a smeared delta-function (Gaussian) shape centered approximately 322 meV below the Fermi level. This is an ideal band structure shape for a thermoelectric material as was discussed by Mahan and Sofo.[124] However, the Fermi level ideally should be within a few kBT from the peak point where the slope of the DOS with respect to energy is maximum.

The Seebeck coefficient at room temperature (300 Kelvin) and the DOS are shown together in Figure 4-6(b). The Mott formula for the thermoelectric power S for metals is defined in the following equation:

$$S_{\alpha\beta} = \frac{\pi^2}{3}\left(\frac{k_B^2 T}{e}\right)\left(\frac{d \ln \sigma_{\alpha\beta}(\varepsilon)}{d\varepsilon}\right)_{\varepsilon = \mu} \qquad (4-2)$$

Where k_B is the Boltzmann constant and the rest of the parameters are defined in Eq. 1. Under constant relaxation time approximation, Seebeck is directly proportional to the slope of the natural log of DOS. To achieve a high Seebeck coefficient, a large slope in the DOS near the chemical potential is required. Therefore, a delta function in a metallic material can potentially correspond to both large conductivity (due to large DOS) and large Seebeck coefficient (due to large slope of DOS) values. Here we note that the Seebeck coefficient has a range of -100 to 100 $\mu V/K$ in a narrow chemical potential range (~500 meV). The main problem in this sample is that the intrinsic Fermi level is not close enough to the peak of the DOS. As shown in Figure 5(b), at the intrinsic level, the Seebeck coefficient is only -10 $\mu V/K$. Hence, the experimental intrinsic Seebeck coefficient is expected to be small.

To reach larger Seebeck values, therefore, careful adjustment of the Fermi level via alloying and doping is needed.

For example, Figure 4-7 demonstrates that upon doping with Al, we can shift the peak in the DOS to lower energies. Specifically, upon 4.5% Al doping, the peak is 371 meV below the Fermi level, which is 49 meV further away from the Fermi level compared to the intrinsic case. On the other hand, upon inclusion of zinc deficiency, we can move the peak toward the higher energies and closer to the Fermi level. Including 4.5% zinc vacancy shifts the peak to approximately -286 meV, bringing it closer to the Fermi level compared to the intrinsic case by 36 meV. In terms of the changes in the Seebeck coefficient, these two doping strategies should show opposite trends which we can confirm experimentally as will be discussed later. However, the predicted changes are not significant enough to increase the Seebeck coefficient significantly. To achieve a high Seebeck coefficient, the

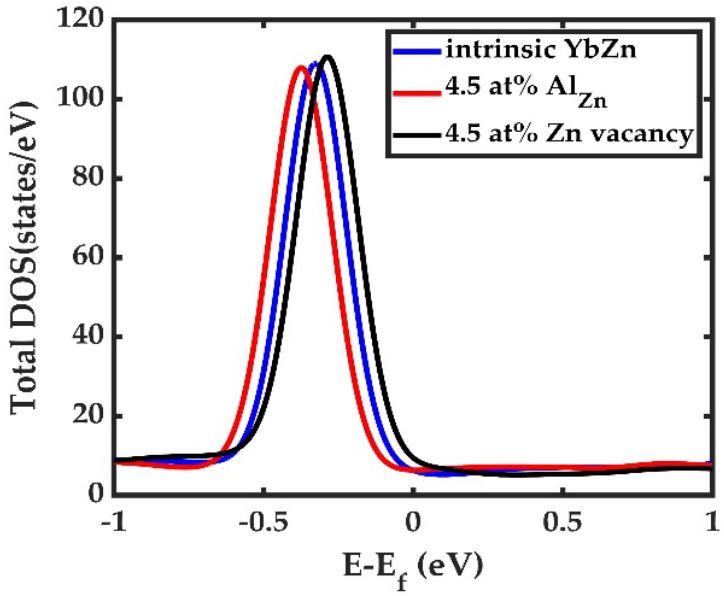

Figure 4-7 Effect of Al doping and Zn deficiency on the density of states. Al doping shifts the DOS to lower energy levels while Zn vacancy moves the DOS to higher energy levels.

Fermi level must be shifted ideally to 202 meV below the intrinsic Fermi level where the slope of the DOS is the largest. There may be other promising transition metals that could serve as dopants to fine-tune the Fermi level. Further research is necessary to optimally adjust the Fermi-level position, which will be the focus of future studies.

Performance

As discussed in the theoretical section, intrinsic YbZ_{11} is expected to have a low Seebeck coefficient. The room temperature value measured for intrinsic $YbZn_{11}$ is only 1 $\mu V/K$. Therefore, we attempted to tune the Fermi level via doping. We note due to the errors in theoretical calculations for small Seebeck values and the presence of defects in experimental samples, a direct quantitative comparison of theory and experiment is not possible, and we only can use theory to predict trends.

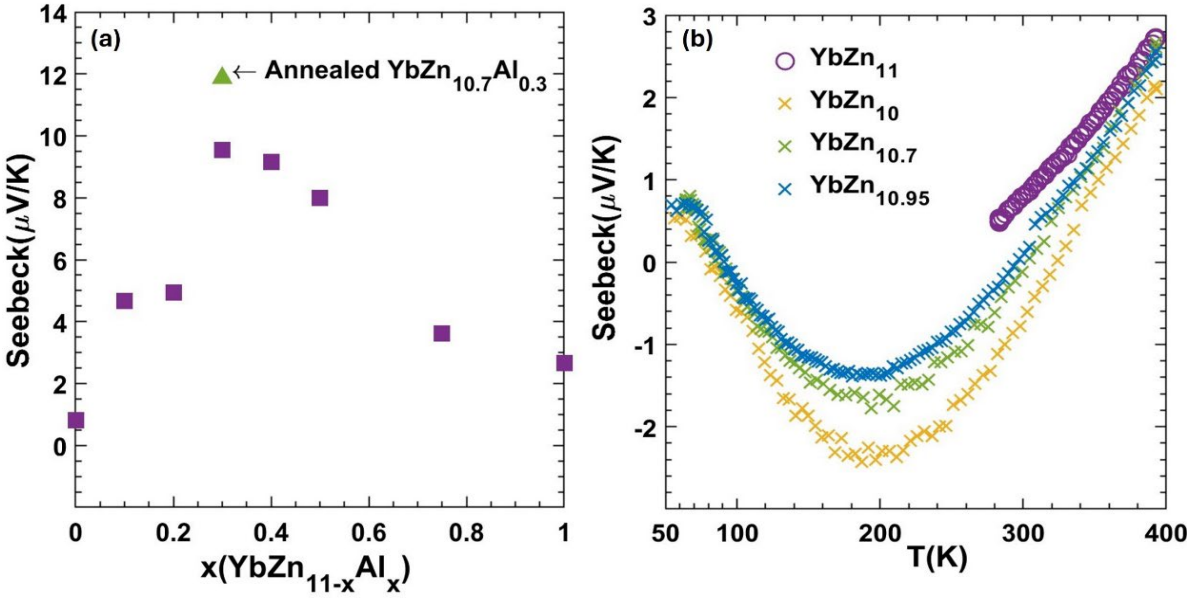

Figure 4-8 (a) Room temperature Seebeck of $YbZn_{11-x}Al_x$ versus Al component x. The green triangle shows the annealed $YbZn_{10.7}Al_{0.3}$. (b) Seebeck of $YbZn_{11-x}$ (x=0.05, 0.3, 1) versus temperature from 70-400K

In Figure 4-8, the trend of measured room temperature Seebeck versus Al composition x ($YbZn_{11-x}Al_x$) is demonstrated. The addition of a small amount of Al improves the Seebeck of YbZn11-xAlx, peaking at $YbZn_{10.7}Al_{0.3}$. A further increase in Al amount reduces the Seebeck coefficient. The low performance of samples with x larger than 0.3 could be attributed to the formation of other Yb-Al compounds due to limited solubility Al in $YbZn_{11}$. However, due to their low concentration, they are not identified in the XRD analysis. The Seebeck value peaks at x=0.3, reaching 9.54 μV/K at 300K. After annealing, the Seebeck further increased by 24.4% to 11.87 μV/K, which should be attributed to improved distribution and dissolution of Al in the Yb-Zn. Further high-temperature measurements after annealing are reported in Figure 4-10 (in the following Supplementary section), indicating further small improvements in the Seebeck coefficient. The discrepancy and uncertainty of data in Figure 4-10 are going to be discussed in the following Supplementary section.

Figure 4-9 summarizes the trends of the transport properties, including the Seebeck coefficient, electrical resistivity, and thermal conductivity as a function of temperature from 50 to 400K for Al-doped samples. The uncertainty on the Seebeck coefficient is less than 15% and for resistivity, it is less than 10%. These values are estimated by repeating the measurements under different thermal history conditions and are detailed in supplementary materials. As temperatures increase, the Seebeck coefficient and resistivity both increases, a common trend in all samples studied here and in general in the

thermoelectric field. The increasing Seebeck coefficient can be explained by the Mott equation of metals (Eqn. 4-2). Assuming no change in the slope of DOS with temperature, Seebeck should increase linearly with temperature. However, the relation is not exactly linear as the Fermi level position changes slightly with temperature. The increase in the resistivity can be explained by the increasing scattering between electrons and phonons at elevated temperatures. Finally, the thermal conductivity is dominated by the electronic

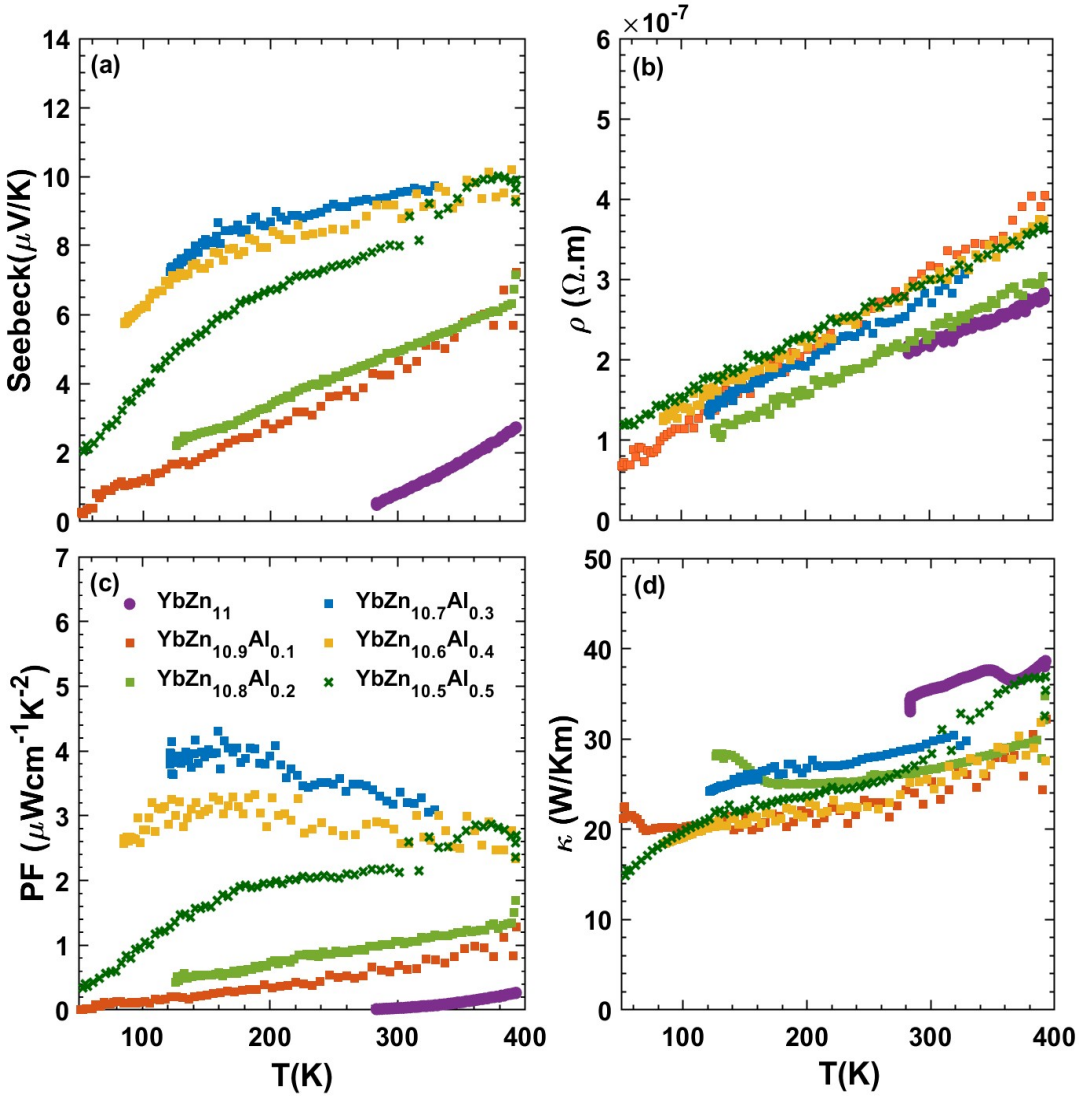

Figure 4-9 (a) Seebeck coefficient, (b) resistivity, (c) power factor, (d) thermal conductivity of $YbZn_{11-x}Al_x$ samples (x=0, 0.1, 0.2, 0.3, 0.3, 0.4, 0.5) versus temperature from 70K-400K.

contribution and follows Wiedemann-Franz law closely. At room temperature, the electronic contribution of the thermal conductivity is 93% for $YbZn_{11}$ sample and 88% for $YbZn_{10.7}Al_{0.3}$. Details of lattice thermal conductivity calculations and relevant plots are presented in the supplementary materials.

The addition of the optimal amount of Al (x = 0.3-0.5) altered the trend of the Seebeck coefficient versus temperature, particularly in the lower temperature range, resulting in a significant increase in the Seebeck coefficient. This increase is the primary reason for the enhanced power factor. The resistivities of all $YbZn_{11-x}Al_x$ samples closely resemble that of intrinsic $YbZn_{11}$, indicating only minor increases in scattering rates at low Al compositions. Further increasing the Al composition surpasses the solubility limit, and leads to different reactions during the melting process, resulting in the appearance of multiple crystalline oxides that increase the resistivity while the thermal conductivity remains close to intrinsic $YbZn_{11}$. The thermoelectric power factor of $YbZn_{11-x}Al_x$ (x=0.3,0.4) peaks at around 100K to 4 $\mu W cm^{-1} K^{-2}$ due to the decreased resistivity at low temperatures and the sharp increase of the Seebeck coefficient.

Other ways of altering the $YbZn_{11}$ system such as non-stoichiometry composition $YbZn_{10.9}$ and Ag and Sn substitution $YbZn_{10.9}Sn_{0.1}$ have been tried. All show improvements but do not exceed the $YbZn_{10.7}Al_{0.3}$ sample. Zn-deficient samples $YbZn_{11-x}$ with x=0.05, 0.3, 1 were prepared using the same methods as those of intrinsic and Al-substitution samples. As shown in Figure 4-8(b), the introduction of Zn deficiency results in more negative Seebeck coefficient values. This is the opposite of what was observed with Al doping and is consistent with our theoretical results discussed in section 3.2. Since Al-doping results in a shift of the DOS delta function to lower energy values and Zn-efficiency does the

reverse (see Figure 4-5,6,7,8), an opposite trend in the Seebeck coefficient is expected using these two doping strategies. While we can predict some trends using the first-principles approach, we acknowledge that a direct comparison between theory and experiment is not possible due to several factors. First, the as-grown $YbZn_{11}$ in the experiment is different from the ideal intrinsic $YbZn_{11}$ used in modelling, and the exact position of the Fermi level is unknown due to inherent low dimensional defects that are evenly distributed in the $YbZn_{11}$ crystal grains such as vacancies, substitutional impurities, and interstitials. As shown in the supplementary materials, changes in the inherent atomic-level defects/impurities results in changes in the DOS which alters the Seebeck coefficient at a given chemical potential. Second, the first-principles data generated has an error bar due to errors in band structure calculations and the constant relaxation time approximation used. As seen in Figure 4-9(a), the Seebeck coefficient does not show a linear trend with respect to temperature for many of the samples. This nonlinear trend can be attributed to temperature-dependent relaxation times as well as minor changes in the chemical potential with temperature and is discussed further in the supplementary materials. While we do not have a good way to estimate this error, the error in Seebeck calculations should be on the order of 10 $\mu V/K$ and therefore small Seebeck values as highlighted in the dashed-line region of Figure 4-6(b) have values close to the noise level of Seebeck calculations.

In the case of Zn deficiency, the value of the Seebeck coefficient is maximum at around 200K, but its value remains small. The vacancies lowered both thermal and electrical conductivity slightly and combined with its low Seebeck values, did not result in improvements larger than Al-doping. At x=1 deficiency the hot-pressed sample shows a large level of cavities and poor sintering. Hence, Al-doping is identified as a better solution

compared to the Zn-deficiency method. Similarly, Ag doping (not presented here) made the Seebeck coefficient more negative, however, Ag solubility is not good enough to significantly affect the Seebeck values toward large negative values.

4.1.4 Supplementary

Sample Stability and Uncertainty

The $YbZn_{11}$ samples demonstrate reproducible results at low temperatures. However, upon annealing, exposure to high temperatures, and long exposure to ambient (air, moisture), the properties change. We also observe visible changes on the surface of the materials. While an in-depth analysis of sample stability is beyond the scope of this work, here we report the range of changes in the properties.

Figure 4-10 reports repeating the measurements for $YbZn_{10.7}Al_{0.3}$. First, we measured the sample as prepared in our lab and using Quantum Design Versalab as discussed in the main manuscript. This is reported as purple open circles. We then annealed the samples and remeasured the properties as shown in green squares. We noted a slight increase in the resistivity and the Seebeck coefficient and an improved power factor. We then shipped the samples to University of Houston for high-temperature measurements, here represented by x. We note the resistivity is similar to our measured data, but the Seebeck coefficient is larger than what we measured. The data at University of Houston was measured using ZEM3. Hence this can be partially related to instrument differences and partially due to sample exposure to ambient conditions for more than a month. Measurement dates are noted in the legend. Upon receiving the sample back, we polished the surface and remeasured the properties. Surprisingly, the results are very similar to our original measurements indicating the effect of annealing on Seebeck is eliminated, which could be

attributed to the temperature history during the ZEM3 measurement. The ZEM3 measurement went up to 900K which is close to the annealing temperature, while the temperature changing rate could be distinguishably different, leading to the Al re-distribution and re-precipitation. Based on these 5 measurements performed on the same

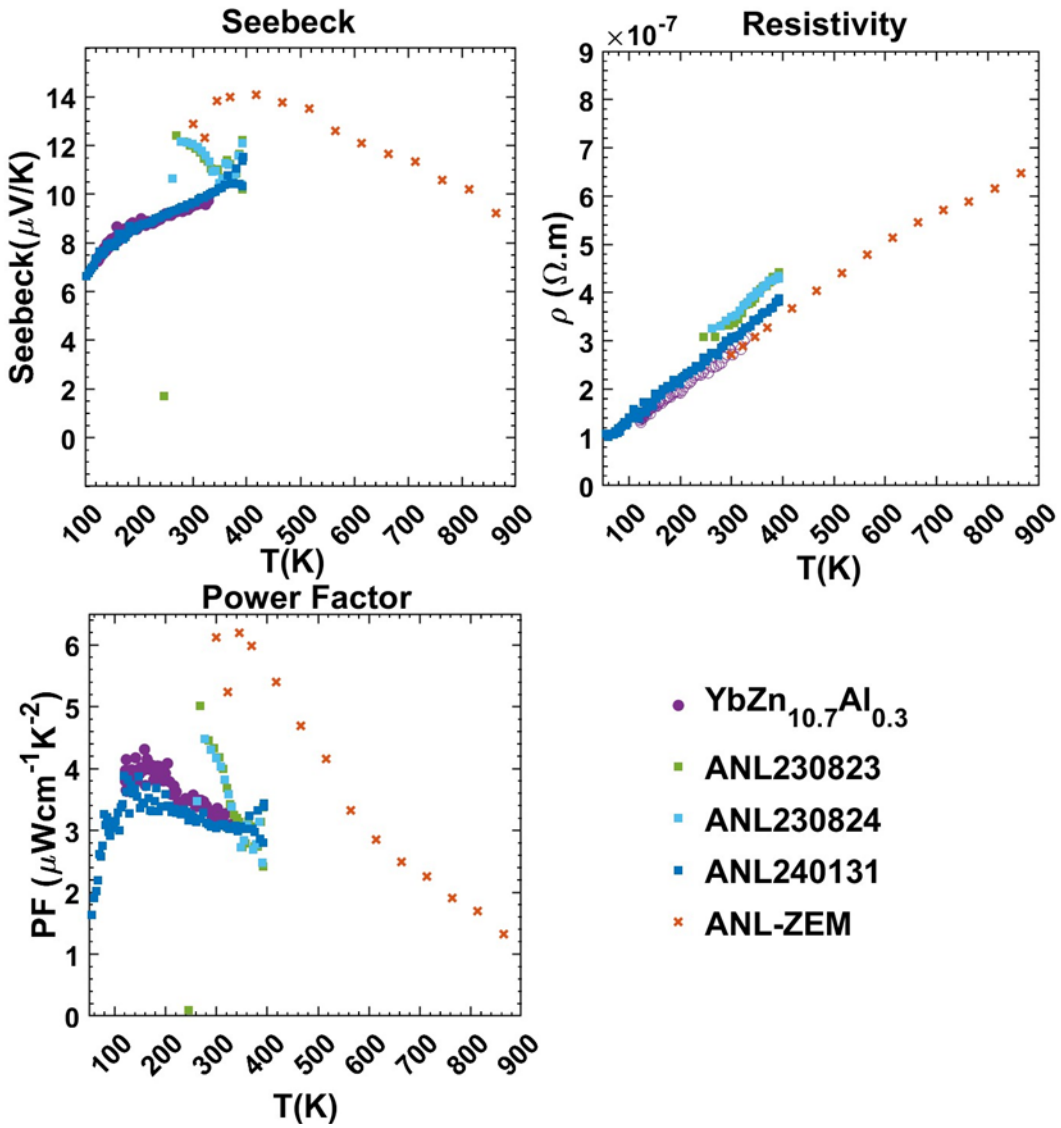

Figure 4-10 High-temperature (a) Seebeck, (b) resistivity, and (c) power factor of annealed/unannealed $YbZn_{10.7}Al_{0.3}$ samples. The ANL230823, ANL230824 samples are annealed samples measured on Quantum Design Versalab at the University of Virginia on August 23rd and 24th 2023. The ANL240131 sample is the same sample after the high-temperature measurement measured by Quantum Design Versalab at the University of Virginia on January 31st, 2024. The high-temperature measurement is done on ZEM3 by Xin Shi at the University of Houston.

sample, we estimate uncertainty in Seebeck measurement to be 15% and 11% at 300K and 400K respectively where the maximum differences are observed. This estimation includes sample conditions and instrument errors and is consistent with ~10% error usually assumed for Seebeck measurements. The variations in the resistivity are smaller and are 8 and 9% respectively.

Uncertainty in Seebeck calculations

To address the uncertainties in our Seebeck coefficient calculations, we used the Mott formula based on the density of states (DOS), assuming a constant relaxation time. First-principles calculations inherently involve some uncertainty due to the usage of pseudopotentials, which are approximations for modeling the interactions between ions and core electrons. Various approximations, such as Local Density Approximation (LDA), Generalized Gradient Approximation (GGA), and Hybrid functionals (HSE, HSE06), with or without Spin-Orbit Coupling (SOC) interactions (particularly relevant for heavy atoms), can lead to differences in the interaction between valence electrons and the core. These differences can alter the band structure and DOS near the Fermi level, thereby influencing the calculated Seebeck coefficient.[5]

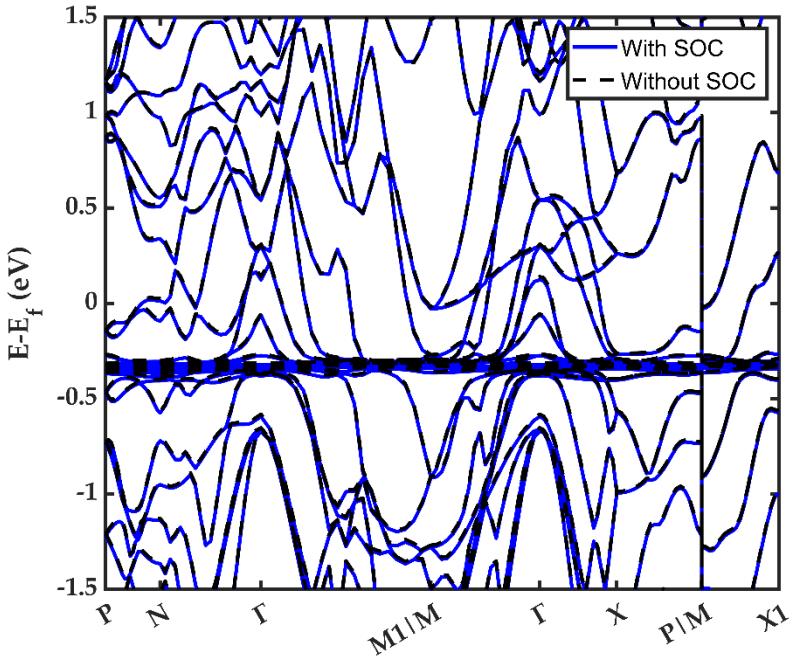

Figure 4-12 Band structure calculation with/without spin-orbit coupling (SOC) effects

As mentioned in the main text and illustrated in Figure 4-12, the inclusion of SOC does not significantly alter the band structure. However, a closer analysis of the DOS in Figure 4-11(a) reveals a subtle change in the slope near the Fermi level when SOC is considered, resulting in a difference of approximately ~6 μV/K in the Seebeck coefficient compared to calculations without SOC, as shown in Figure 4-11(b).

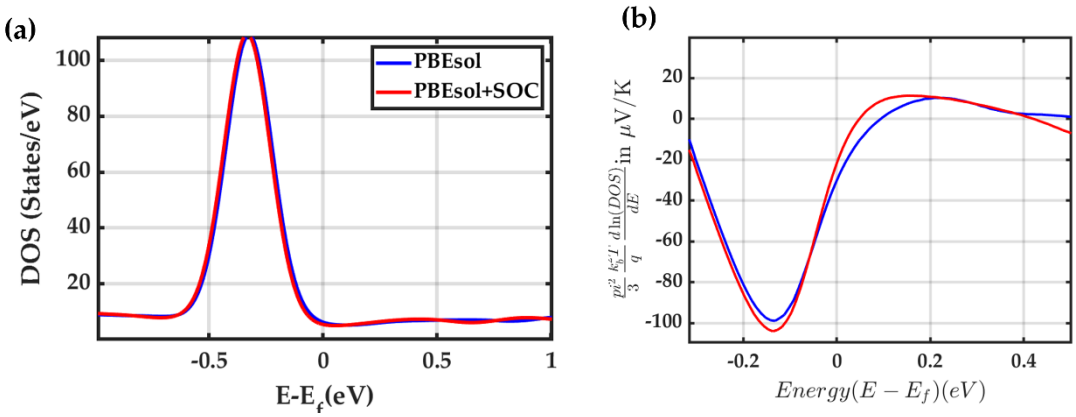

Figure 4-11 Spin-Orbit Coupling Effects on Seebeck.

In our calculation, we ensured consistency by using the same computational parameters for all defect calculations to minimize variability. For convenience, we excluded the effects of SOC in favor of faster calculations. As was discussed in the main text there are multiple other sources of error in Seebeck calculations, we discuss two main sources here:

1- Position of the Fermi level. Since the samples inherently contain defects, the position of the chemical potential is not priori known. In the case of $YbZn_{11}$, due to the fragile nature of the samples, thinning to perform Hall data to determine the position of the Fermi level experimentally was not possible. Below we show that by adding defects (Zn vacancy, or impurities) the chemical potential position can change resulting in different values of the Seebeck coefficient. As shown in Figure 4-13(a), in the presence of defects such as Zn vacancy and Al substituting Zn, the Seebeck coefficient can vary from the intrinsic value to larger (vacancy case) or lower (Al case). This shift impacts the Seebeck coefficient and is a crucial factor in interpreting experimental results. Simulating these effects precisely in first-principles calculations is challenging due to computational complexity and resource limitations as well as a lack of accurate information on the precise nature and concentration of the impurities in the experiment. Hence, theory can only provide general guidance and cannot predict the experimental values accurately.

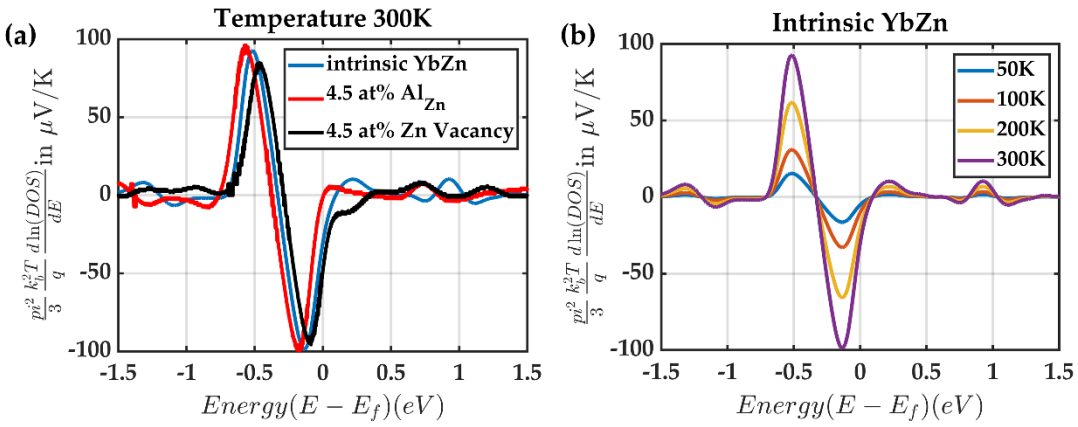

Figure 4-13 Seebeck coefficient with respect to defects and temperature.

2- Energy-dependent Relaxation times: The Mott Formula ($S = \frac{\pi^2}{3}\left(\frac{k_B^2 T}{e}\right)\left(\frac{1}{DOS}\frac{\partial DOS}{\partial \varepsilon} + \frac{1}{\tau}\frac{\partial \tau}{\partial \varepsilon}\right)_{\varepsilon = \mu}$) predicts the Seebeck coefficient to change not only with the DOS but also with energy-dependent relaxation times, $\tau(\varepsilon)$. Within constant relaxation time, the second term in the Mott equation is neglected which can play a significant role when the Seebeck values are small. When ignoring the second term, and when chemical potential is fixed, the Mott equation predicts a linear increase in the Seebeck coefficient with respect to temperature (see Figure 4-14). While some of the samples show linear S with respect to T (e.g. $Yb_{10.6}Al_{0.4}Zn_{11}$), some others show a clear deviation from linear temperature dependence ($Yb_{10.8}Al_{0.2}Zn_{11}$) as shown in Figure 4-7 pointing to the significance of the second term.

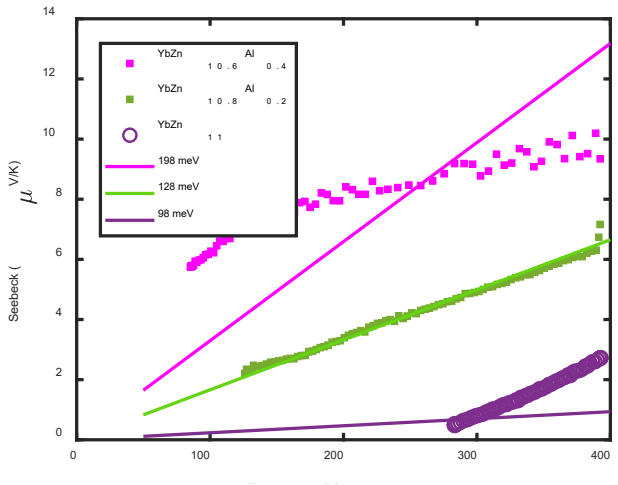

Figure 4-14 Seebeck coefficient vs temperature. Symbols are experimental data and lines are theoretical results obtained using the Mott Equation as applied to $YbZn_{11}$ and for different chemical potentials

Electron backscatter diffraction (EBSD)

Electron backscatter diffraction (EBSD) in scanning electron microscopy (SEM) is a powerful technique for characterizing the crystallographic structure and orientation of materials. The electrons interact with the crystal lattice, scattered back as the backscattered electrons, and produce a diffraction pattern known as a Kikuchi pattern. These patterns contain information about the crystal structure, which the EBSD system can analyze to identify phases and determine the crystal orientation at each point on the sample surface.

To map the $YbZn_{11}$ phases, the EBSD system compares detected patterns to the reference $YbZn_{11}$ crystal structures. By scanning the sample spot by spot, EBSD can create detailed maps of the spatial distribution of the $YbZn_{11}$ crystal structure, along with their orientations.

Figure 4-5 and Figure 4-15 show the EBSD images and mapping on $YbZn_{11}$ and $YbZn_{10.7}Al_{0.3}$ samples, demonstrating the homogeneity of the $YbZn_{11}$ matrix and the relatively large grain size.

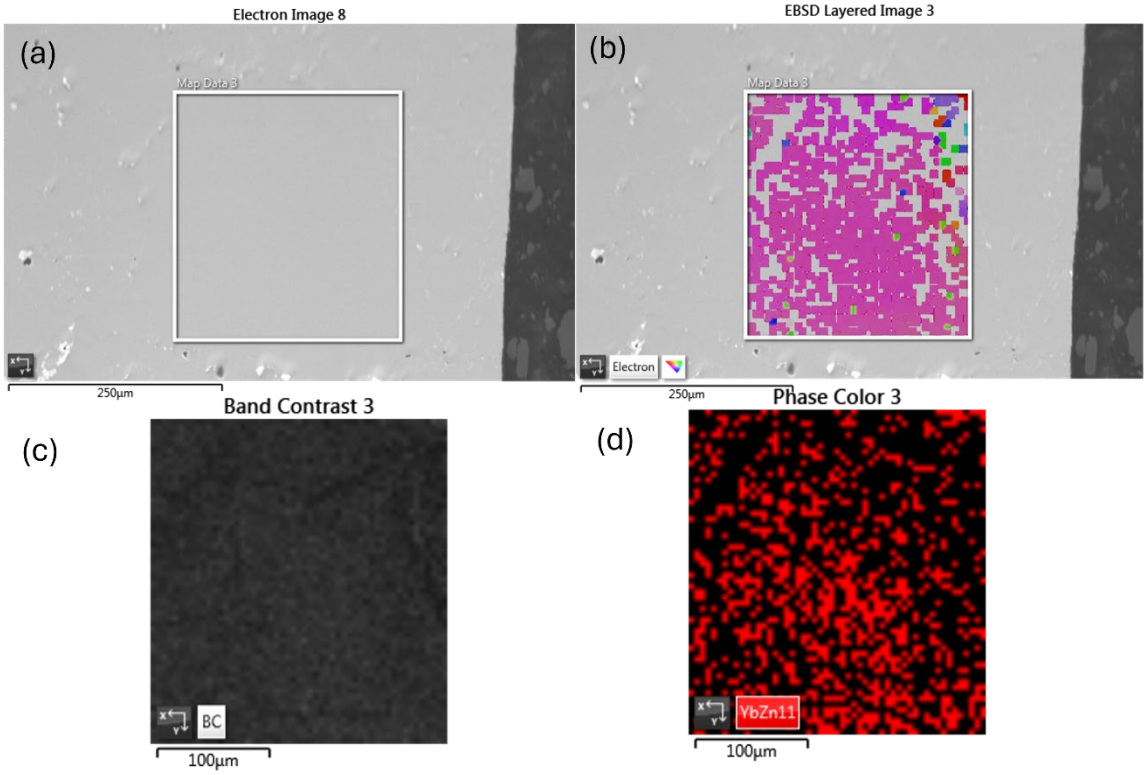

Figure 4-15 EBSD on $YbZn_{11}$ sample

4.1.5 Conclusion

$YbZn_{11}$-based samples were synthesized and confirmed using XRD and SEM methods. Small pores, Yb_2O_3, and zinc-rich defects were identified in the samples. The thermoelectric properties are reported for the first time. All samples have low resistivity confirming the metallic nature of the samples. The thermal conductivity of the samples is dominated by the electronic contribution as expected from metals with the intrinsic sample having a thermal conductivity of 35 $Wm^{-1}K^{-1}$ at room temperature and further increasing with temperature. The downside of these samples is their low Seebeck coefficient values. Efforts to improve the Seebeck coefficient by Al substitution are conducted and resulted in

improved Seebeck by an order of magnitude without sacrificing the electrical or thermal conductivity. However, the thermoelectric power factor remains modest with a peak value of 4 $\mu Wcm^{-1}K^{-2}$ at 100 K. First-principles calculations identified a Gaussian-shape DOS ideal for thermoelectric power factor in $YbZn_{11}$. However, the Fermi level is not ideally positioned with respect to this Gaussian function and needs to be adjusted for high performance. The limited solubility of Al, Sn, and Ag prevented further adjustments to the Fermi level. Similarly, zinc-deficiency tuning of the Fermi level is limited and does not allow for adjusting the Fermi level far enough to verify the existence of the DOS peak and, therefore, the high performance. Further studies of other dopants and alloying are needed to adjust the Fermi level to increase the Seebeck coefficient.

4.2 Other Attempts

Other than the $YbZn_{11-x}Al_x$ system reported above, ytterbium-silver and other ytterbium-zinc intermetallic compounds have been tested. Various synthesis methods were tried to synthesize pure target compounds, most of which failed due to inhomogeneity and impurities. Yb_2Zn_{17} was synthesized but abandoned later due to difficulty of the processing of the ingots and the low performance. In the study of cobalt-tin alloy system, Co-Sn intermetallic compounds were also synthesized. Co_3Sn_2 sample was tested for the performance. A study on Ag_2Se was conducted beside all the studies on metallic materials, but did not progress further since the performance of the samples didn't match the references.

4.2.1 Ytterbium-Silver Intermetallic Compounds

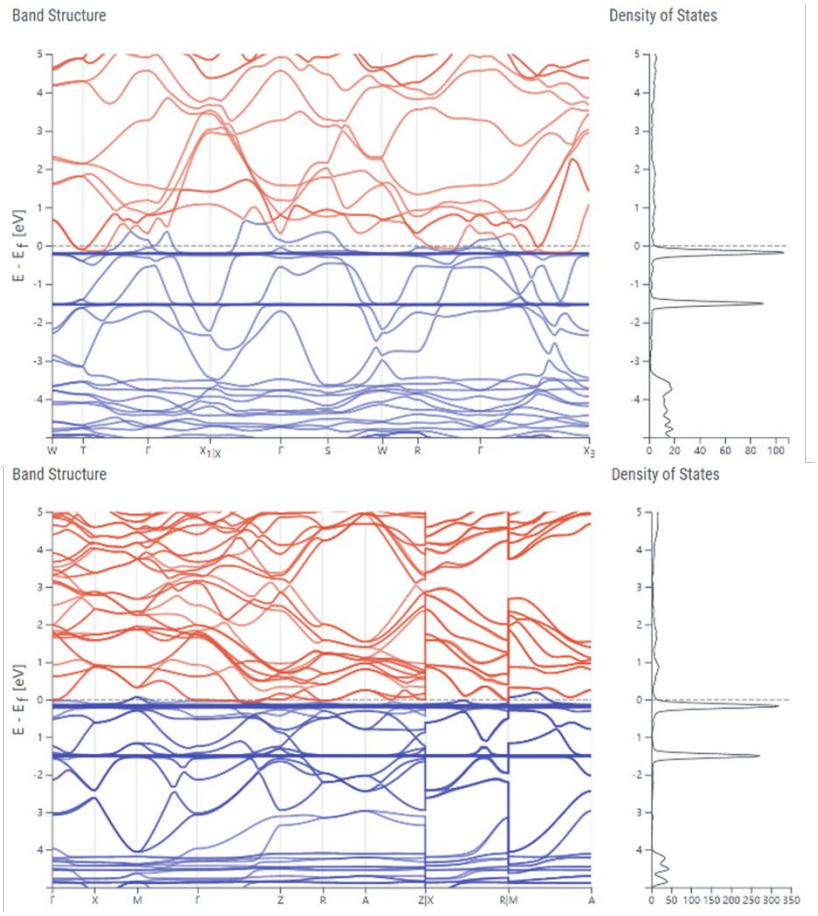

Figure 4-16 Band structure and density of states diagram of Ag_2Yb (top) and Ag_2Yb_3 (bottom).

According to the band structure and DOS calculation from the Topological Materials Database[129–132], Ag_2Yb and Ag_2Yb_3 show a sharp peak of the DOS near the Fermi level. The following attempts are made to synthesis Ag-Yb intermetallic compounds.

Arc melting

99.9% sublimed Yb pieces and 99.999% silver shots are mixed according to the stoichiometry of Ag_2Yb_3 and Ag_2Yb. The mixed pure metals are arc-melted in an Argon atmosphere. After melting the ingot showed inhomogeneity. XRD is performed on both sides of the ingot after polishing, confirming that both ingots are inhomogeneous. For

Ag_2Yb, the XRD result of the bottom side of the ingot shows majorly the peaks from Ag_2Yb but after cutting, the cross-section shows the inhomogeneous area with the color difference. Peaks from Ag_2Yb_3, Ag_3Yb_5, and Ag_2O are found in the Ag_2Yb_3 XRD results . This could be due to the vapor pressure difference between Yb and Ag (order of 10^3) at melting temperature. And the inhomogeneity should be caused by the initial form of the metals being bulk with limited mixing.

Furnace Melting

99.9% sublimed Yb pieces and 99.999% silver shots are mixed according to the stoichiometry of Ag_2Yb_3. The mixed pure metals are loaded into a Mo crucible. The crucible is then loaded into a fused quartz glass tube, the tube is vacuumed and filled with Argon three times, then sealed by heating the glass to soft. The sealed tube is heated up to 960 ºC to melt for 16 hours. After cooling down the ingot is ground using ball-milling into powder. Peaks of Ag_2Yb_3 are found in XRD. The powder is then hot pressed at 500 ºC 56Mpa for 5 minutes with argon gas filling. The pellet is brittle and breaks up when being polished, which limited the further characterization of the sample since it requires mechanical work on the pellet.

Ball milling

99.9% sublimed Yb pieces and 99.999% silver powders are mixed according to the stoichiometry of Ag_2Yb. The mixture is then loaded into a stainless steel ball-milling jar. A VQ-N high-energy vibratory ball mill from Across International was used to ball mill the mixed powder for the maximum continuous working time of 9999 seconds, at 1200 rpm. The products are heavier oxidized after ball milling.

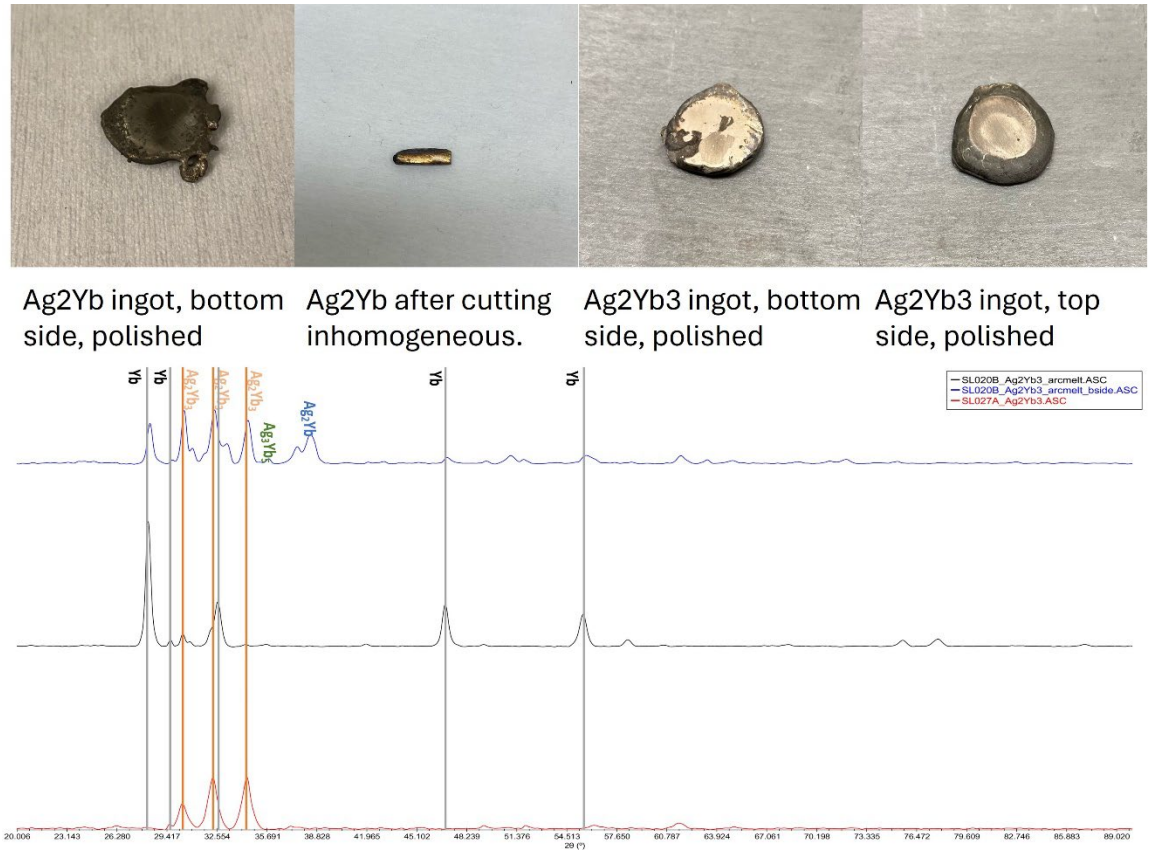

Figure 4-17 Ag-Yb samples inhomogeneity after arc-melting (top), XRD results on different samples

4.2.2 Other Ytterbium-Zinc Intermetallic Compounds

Like the case of Yb-Ag, and according to the band structure and density of state calculation from the Topological Materials Database [129–132], Yb_2Zn_{17} show the sharp peak of the density of state (DOS) near the Fermi level.

99.9% sublimed Yb pieces and 99.999% zinc shots are mixed according to the stoichiometry of Yb_2Zn_{17}. Yb_2Zn_{17} sample was then prepared by melting the mixed pure metals in the Mo crucible at 800ºC. The XRD result of the grounded powder shows major peaks of Yb_2Zn_{17} and minor peaks of $YbZn_{11}$. Further, Ag and Al are used to substitute Zn to adjust the Fermi level. 99.999% silver shot and 99.999% aluminum powder are added according to stoichiometry. The $Yb_2Zn_{15}Ag_2$ sample is made in the Mo crucible and the addition of Ag makes the ingot difficult to be removed from the crucible. As the result, two $YbZn_{10}Ag$ samples are made in both Mo crucible and glass tube to compare, confirming that the addition of Ag makes the ingot more ductile and tough to be broken apart and taken out of the crucible. The $YbZn_9Al_2$ sample is melted in the sealed glass tube. All ingots are

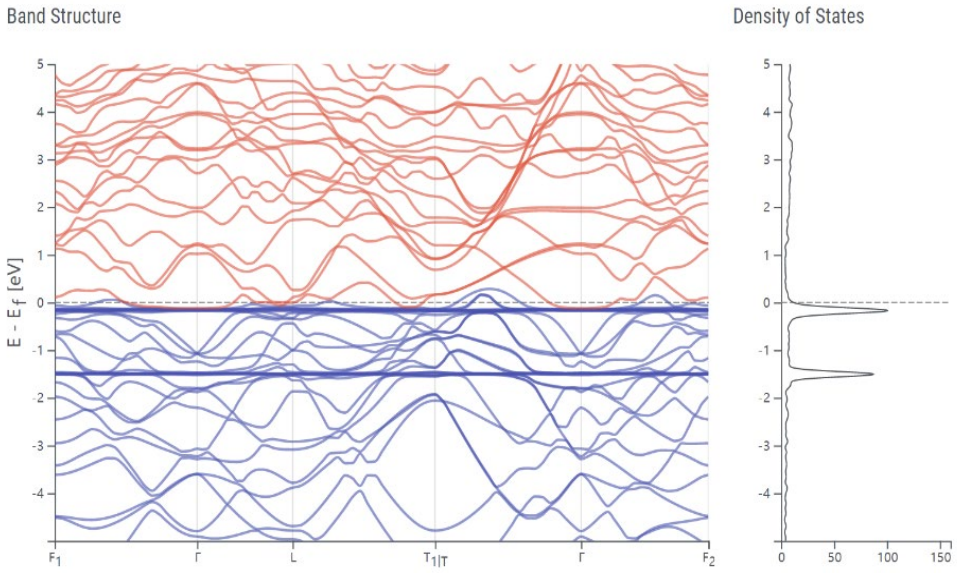

Figure 4-18 Band structure and density of states diagram of Yb_2Zn_{17}

then ball milled in an Ar-filled ball mill jar. the powders are then hot pressed at 550 ºC 56Mpa for 5 minutes with argon gas filling. Transport performance is measured by the Quantum Design PPMS Versalab.

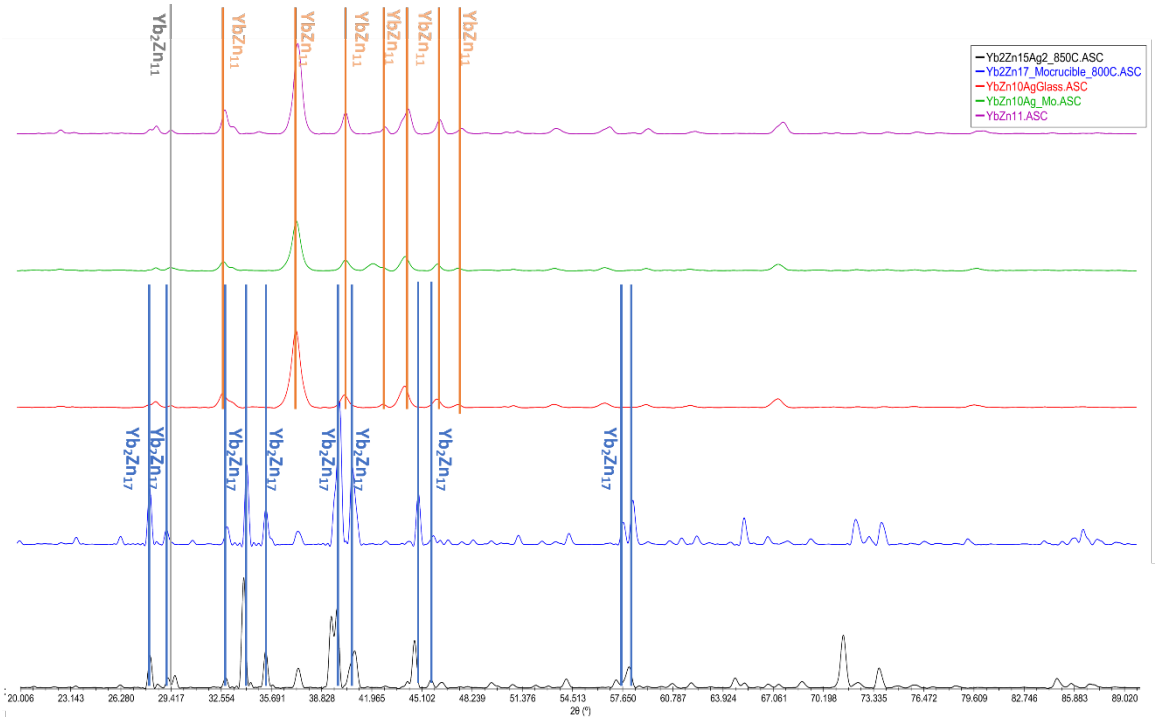

Figure 4-19 XRD results of early Yb_2Zn_{17} and $YbZn_{11}$ samples and doping trials.

As shown in Figure 4-19 , XRD results indicate the existence of minor Yb_2O_3 impurities in samples that are melted in the glass tube which is the side-effect of the Yb-SiO_2 reaction. But for Ag substitution samples, no peaks from silver compounds are found. In the Mo crucible, a good Yb_2Zn_{17} sample can be made. The performance of all the samples is shown in Figure 4-20. The $YbZn_{11}$ sample was measured only from 290 K to 390 K. Others are measured from 50 K to 390 K. The intrinsic $YbZn_{11}$ shows better performance even with the presence of the oxide. The addition of Ag makes both Yb_2Zn_{17} and $YbZn_{11}$ Seebeck curves move towards the negative therefore resulting in a lower absolute value. And the

addition of Al improves the performance of $YbZn_{11}$ at temperatures below 360 K. However, the cost is a lower Seebeck at higher temperatures and worse electrical conductivity.

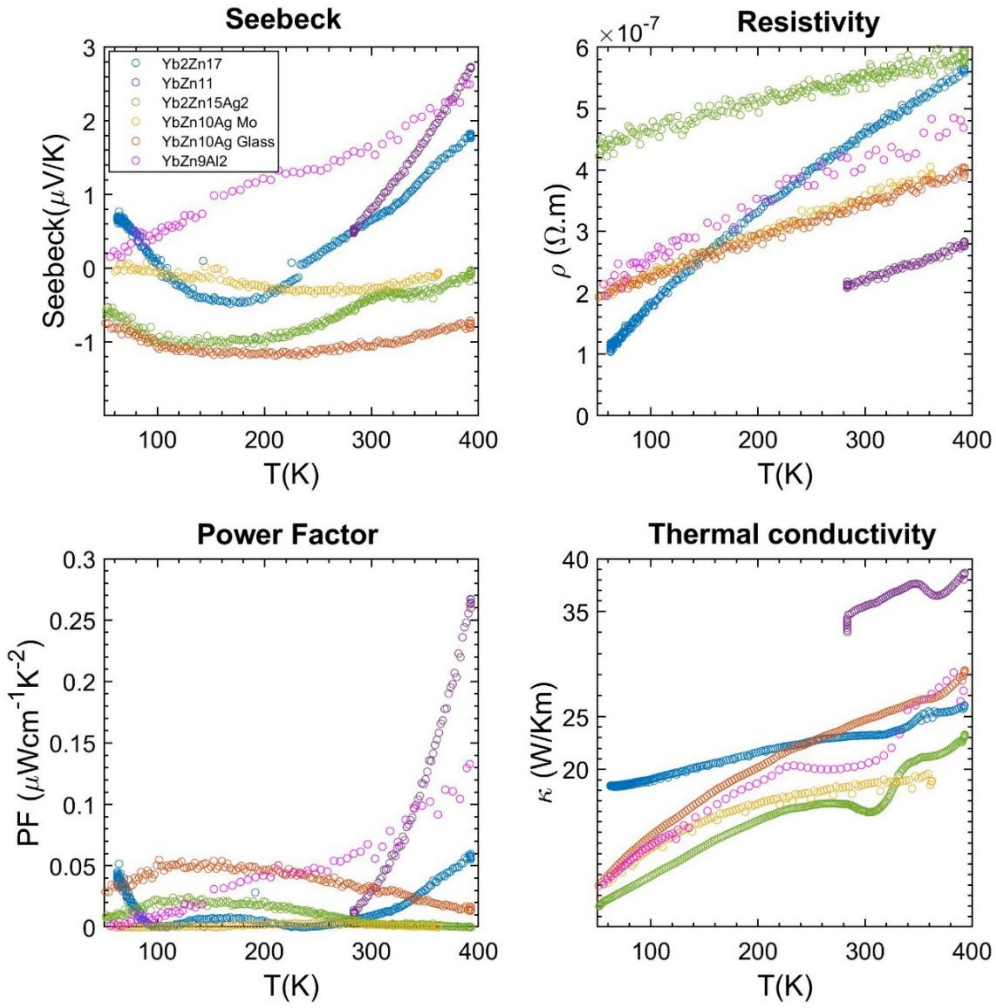

Figure 4-20 (a) Seebeck coefficient, (b) resistivity, (c) power factor, (d) thermal conductivity of early Yb_2Zn_{17} and $YbZn_{11}$ samples and doping trials.

4.2.3 Cobalt-Stannide

Cobalt-stannides, as intermetallic compounds, were investigated while studying the Co-Sn alloy system. The band structure of CoSn and Co_3Sn_2 features the sharp peak of the density of state (DOS) near the Fermi level[129–132]. High-purity cobalt and tin powders are weighted and mixed in glove box and loaded into jars for high energy (HE) ball mill and low-energy (LE) planetary ball mill. The HE ball-milling lasts 4 hours while the LE ball milling lasts

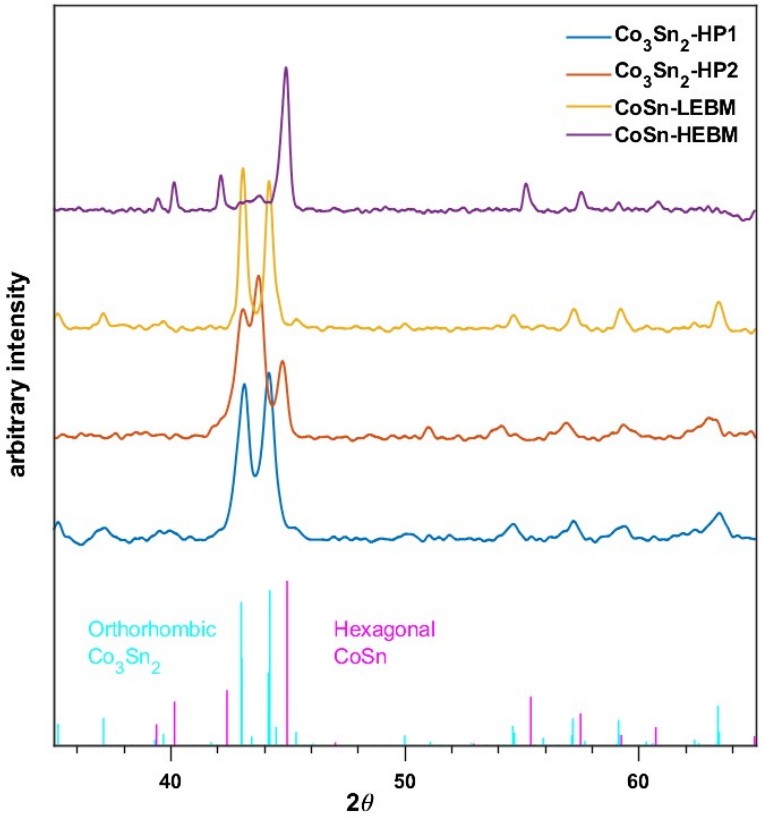

Figure 4-21 XRD of ball milled-hot pressed Co_3Sn_2. The magenta and cyan straight lines are reference peaks for hexagonal CoSn and orthorhombic Co_3Sn_2.

30 hours. The HE ball-milling produces CoSn intermetallic compounds and minor impurities of tin oxides. The LE ball milling produces Co_3Sn_2 intermetallic compounds. For both LE and HE ball milling, loss of tin during the process is suggested by the products. Both samples turn into Co_3Sn_2 after hot press. The performance of the hot pressed samples is very metallic, showing a Seebeck of -10 μV/K. The investigation does not go further since Ni-Fe alloy appears more promising and the limited timeline for graduation.

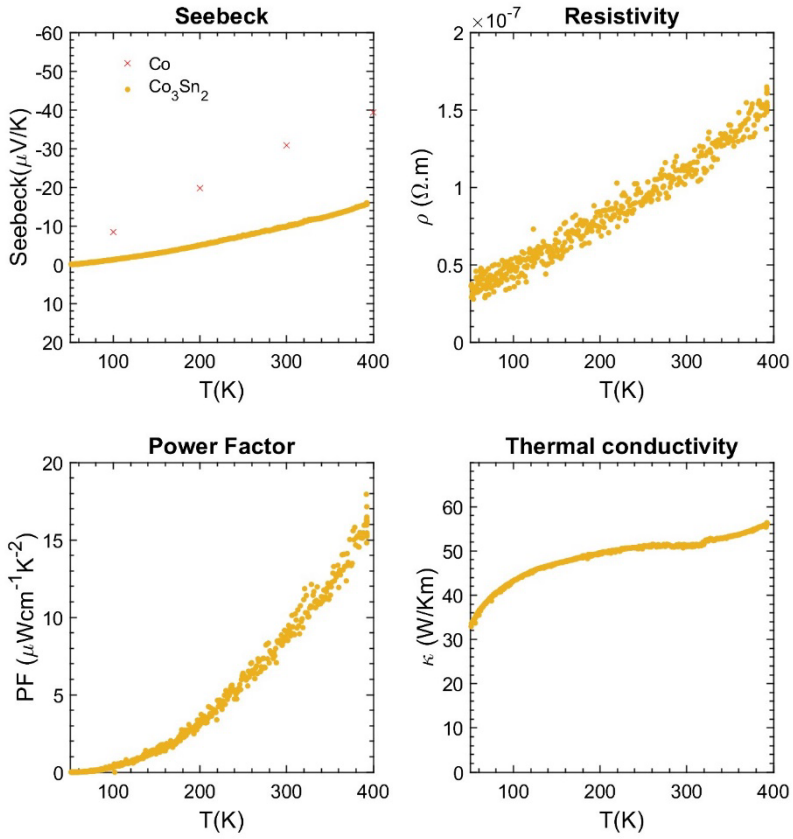

Figure 4-22 (a) Seebeck coefficient, (b) resistivity, (c) power factor, (d) thermal conductivity of Co_3Sn_2 and Co reference (red crosses).

4.2.4 Silver Selenide

Ag_2Se has been considered as a good candidate for room-temperature thermoelectric applications because of the combination of low thermal conductivity, high Seebeck coefficient and high electrical conductivity [137,138]. A semiconductor-superionic phase transition at 407K provides the Ag_2Se system a new way to further improve its thermoelectric properties [139]. Previous works have shown that by varying silver and selenium fractions, ZT values near 1.0 could be reached [137,138,140]. However, there are a limited number of papers that show improvements via solid solution or doping. Therefore,

we chose Ag_2Se as our first material system to work on and started to synthesize Ag_2Se via ball-milling, which has been proved by previous work [141].

Ag_2Se Synthesis

In total 8 grams of pure Ag (powder, ≥99.9% trace metals basis) and Se powders (powder, −100 mesh, 99.99% trace metals basis) are weighed based on mass percentage calculated according the stoichiometry. They are mixed and loaded into a stainless jar. The jar is sealed in the glove box to keep the mixture staying in the protective atmosphere. The jar is then mounted on a high energy ball mill to ball mill the powder at 1200 rpm for 6 hours. The ball-milled powder is taken out of the jar after cooling down to room temperature and hand milled into fine powder for hot press. The hot press is performed at 330 ºC, 56Mpa for 10 minutes with argon gas filling. A disk-shaped solid sample with a 0.95 relative density is obtained after hot press.

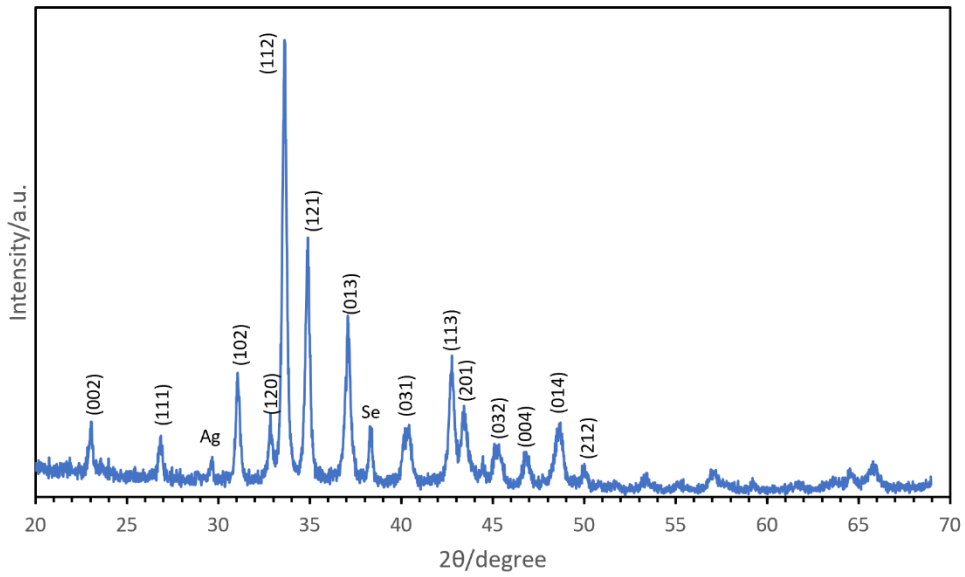

Figure 4-23 XRD result of synthesized then hot pressed Ag_2Se sample.

Characterization

X-ray diffraction analysis is performed on both the powder after ball milling and the solid sample after hot press using an Empyrean multipurpose X-ray diffractometer. The data is analyzed using Malvern Panalytical's HighScore Plus. The results confirmed that Ag_2Se is synthesized after ball milling and survived after hot press. A minor peak of Se is observed in the result of ball-milled powder. And minor peaks of Ag and Se are found in the result of hot-pressed sample, which indicates that decomposition could have happened in the hot press process.

Transport Properties

The transport properties are measured in a PPMS Versalab system from Quantum Design. Five samples were prepared (Ag_2Se, $Ag_2Se_{1.01}$, $Ag_2Se_{1.02}$, annealed $Ag_2Se_{1.02}$, $Ag_{1.9}Cu_{0.1}Se$, and $Ag_{1.9}Cu_{0.1}Se0.9S_{0.1}$). The room temperature (300K) properties are listed in the Table 4-1 below. Comparing with reference[140], The Seebeck coefficients and resistivities of all our samples are lower whereas the thermal conductivities are higher, resulting in much lower ZT values from all our samples. The results indicate that in the samples made in our process, the carrier concentrations are higher than the reference. The nature of our synthesis process makes controlling the compositions and tuning the carrier concentrations difficult. Because of this persistent problem, and inconsistency in literature data, we decided not to pursue this sample any further after the project and funding came to an end.

Table 4-1 Ag_2Se Samples performance and references

	S (μV/K)	ρ (uΩ-m)	$S^2\rho$ ($mWcm^{-1}K^{-2}$)	κ(W/K-m)	ZT
Ag_2Se	-70.07	4.53	1.10	1.97	0.17
$Ag_2Se_{1.01}$	-78.08	4.52	1.35	2.09	0.20
$Ag_2Se_{1.02}$	-57.26	3.27	1.00	1.90	0.16
$Ag_2Se_{1.02}$ annealed	-52.51	2.89	0.95	1.91	0.15
$Ag_{1.9}Cu_{0.1}Se$	-46.44	2.26	0.93	3.11	0.09

$Ag_{1.9}Cu_{0.1}Se_{0.9}S_{0.1}$	-33.80	2.89	0.40	2.59	0.05
Ag_2Se [140]	-127.68	7.31	2.23	1.18	0.55
$Ag_2Se_{1.01}$ [140]	-144.65	6.86	3.07	1.00	0.91
$Ag_2Se_{1.02}$ [140]	-162.42	9.43	2.80	0.93	0.87

4.3 Summary and Prospects

The band structure from first-principle calculation from the topological database is used as a tentative guide for screening Yb-based intermetallic compounds. The results suggest that the discrepancy of the modeling results and experiments. The $YbZn_{11}$ intermetallic compounds suffer from the unfavorable position of the DOS peak to the Fermi level and the limited methods to tune the Fermi level. Future studies on intermetallic compounds for high power factor and high effective thermal conductivity should be based on a more accurately calculated band structure with a more strictly positioned sharp slope of DOS at Fermi level. A more effective way of screening the materials with desired band structure should be developed utilizing methods like data mining and machine learning.

5. Summary

This dissertation investigates the potential of metallic thermoelectric materials for active cooling applications, with the goal of addressing critical challenges in thermal management. In contrast to traditional semiconducting thermoelectrics, metallic materials possess high electrical and thermal conductivities, positioning them as promising candidates for enhancing effective thermal conductivity (κ_{eff}). The research focuses on binary alloys of transition metals and ytterbium-based intermetallic compounds, evaluating and optimizing their power factor and effective thermal conductivity performance. Additionally, the study explores the integration of these alloy materials with advanced manufacturing technologies to further enhance their capabilities in thermal management applications.

For binary alloys, results on cobalt, nickel, and chromium-based alloys were presented. First, I studied the use of Directed Energy Deposition (DED), which enabled low-cost, scalable fabrication of Cu-Ni alloys from industrial powders and supported complex geometries that minimize thermal contact resistance for efficient heat transfer. The DED-processed samples achieved thermoelectric power factors comparable to those reported for high-purity Cu-Ni alloys. Meanwhile, the ball-milled and hot-pressed (BM-HP) samples made from industrial-level powder reach a peak power factor of 35 $\mu W/cm \cdot K^2$ at room temperature. The κ_{eff} of the BM-HP sample, with a 1K temperature difference, rises from 172 W/m·K at room temperature to 403 W/m·K at 390K. Although DED samples showed some inhomogeneity and anisotropic performance, their overall thermoelectric performance aligned closely with mechanically alloyed samples, showing the feasibility of using additive manufacturing for metallic thermoelectric alloys suitable for industrial applications. However, the mechanism of thermopower improvement due to the selenium

addition remains unclear and the optimization of the DED parameter and process for high effective thermal conductivity need to be investigated in the future.

Then the thermoelectric performance of arc-melted Ni-Fe alloys containing 45-70 atomic percent nickel was evaluated from 50K to 400K, with $Ni_{55}Fe_{45}$ and $Ni_{60}Fe_{40}$ alloys exhibiting an optimal peak power factor of 120 $\mu W/cm \cdot K^2$ at 200K. The best-performing $Ni_{60}Fe_{40}$ and $Ni_{70}Fe_{30}$ alloys achieved effective thermal conductivities exceeding 600 W/m·K at 400K, surpassing both pure copper and Cu-Ni alloys under similar conditions. SEM/ EDS characterization of the Ni-Fe microstructure provided insights into grain size and elemental distribution of the arc-melted samples. The study also reported an anomalous Seebeck coefficient dependence on composition at intermediate temperatures, initially attributed to local concentration fluctuations, a hypothesis that EDS analysis disproved. These findings highlight the high power factor potential of Ni-Fe alloys and underscore the need for further exploration of factors such as grain size, magnetic domains, and defects to maximize performance for active cooling applications.

Another strategy to search for high power factor intermetallic compounds starts with looking for a sharp density of state slope near the Fermi level in the band structure calculation. Ytterbium-zinc and ytterbium-silver intermetallic compounds were investigated. $YbZn_{11}$-based intermetallic compounds were synthesized and analyzed for thermoelectric properties for the first time, with structural integrity confirmed by XRD and SEM. While Seebeck coefficients were initially low, Al substitution successfully improved them by an order of magnitude without compromising electrical or thermal conductivity. However, the maximum power factor achieved was modest. First-principles calculations suggested an ideal Gaussian-shaped DOS for thermoelectric performance in $YbZn_{11}$, but

misalignment of the Fermi level limited optimization, with further adjustments constrained by the solubility limits of Al, Sn, Ag, and zinc deficiency. Future work should focus on exploring additional dopants and alloying to fine-tune the Fermi level and enhance the Seebeck coefficient for improved thermoelectric performance.

This thesis should bring up interest in metallic TE materials for thermoelectric active cooling applications. With their intrinsic high electrical and thermal conductivity, the κ_{eff} of the metallics TE materials can be significant when the thermopower (absolute Seebeck coefficient) is large. This can be achieved via alloying and/or forming intermetallic compounds. Further studies are needed in the field of metallic TE materials that have been ignored by the thermoelectric community for a long time. From an experimentalist's point of view, the high Seebeck values reported in metallic materials, especially alloys, should be revisited to explore the possibility of optimization for high effective thermal conductivity. And the basic mechanisms that lead to high Seebeck, high power factor and therefore high effective thermal conductivity in specific material should be investigated more thoroughly. Combining with the theoretical modeling and calculation, the methodologies for evaluating and systemically improving the performance of metallic materials for active cooling should be developed just like the works that have been done for the high ZT thermoelectrics. Thermoelectric active cooling has the potential to solve the urgent thermal management challenges. I hope my work can be a stepping-stone, a catalyst, and a gateway for a new horizon of research in metallic and thermoelectric materials.

Reference

1. Zhang, Z., Wang, X. & Yan, Y. A review of the state-of-the-art in electronic cooling. *e-Prime - Advances in Electrical Engineering, Electronics and Energy* **1**, 100009 (2021).

2. Sohel Murshed, S. M. & Nieto de Castro, C. A. A critical review of traditional and emerging techniques and fluids for electronics cooling. *Renewable and Sustainable Energy Reviews* **78**, 821–833 (2017).

3. Shiao, H. C., Chua, D., Lin, H. P., Slane, S. & Salomon, M. Low temperature electrolytes for Li-ion PVDF cells. *J Power Sources* **87**, 167–173 (2000).

4. Stuart, T. A. & Hande, A. HEV battery heating using AC currents. *J Power Sources* **129**, 368–378 (2004).

5. Mahan, G. D. Good Thermoelectrics. in *Solid State Physics* vol. 51 81–157 (Academic Press, 1998).

6. Irkhin, V. Y. & Irkhin, Y. P. *Electronic Structure, Correlation Effects and Physical Properties of d-and f-Metals and Their Compounds*. (Cambridge Int Science Publishing, 2007).

7. Pei, Y., Wang, H. & Snyder, G. J. Band Engineering of Thermoelectric Materials. *Advanced Materials* **24**, 6125–6135 (2012).

8. Chen, Z., Zhang, X. & Pei, Y. Manipulation of Phonon Transport in Thermoelectrics. *Advanced Materials* **30**, 1705617 (2018).

9. Snyder, G. J. & Toberer, E. S. Complex thermoelectric materials. *Nature Materials 2008 7:2* **7**, 105–114 (2008).

10. Zhu, T. *et al.* Compromise and Synergy in High-Efficiency Thermoelectric Materials. *Advanced Materials* **29**, 1605884 (2017).

11. Zebarjadi, M., Esfarjani, K., Dresselhaus, M. S., Ren, Z. F. & Chen, G. Perspectives on thermoelectrics: from fundamentals to device applications. *Energy Environ Sci* **5**, 5147–5162 (2012).

12. Mehdizadeh Dehkordi, A., Zebarjadi, M., He, J. & Tritt, T. M. Thermoelectric power factor: Enhancement mechanisms and strategies for higher performance thermoelectric materials. *Materials Science and Engineering: R: Reports* **97**, 1–22 (2015).

13. Nolas, G. S., Poon, J. & Kanatzidis, M. Recent Developments in Bulk Thermoelectric Materials. *MRS Bull* **31**, 199–205 (2006).

14. Wei, J. *et al.* Review of current high-ZT thermoelectric materials. *Journal of Materials Science 2020 55:27* **55**, 12642–12704 (2020).

15. Goldsmid, H. J. *Applications of Thermoelectricity*. (Methuen and John Wiley, 1960).

16. Heikes, R. R. & Ure, R. W. *Thermoelectricity: Science and Engineering*. (1961).

17. Tritt, T. *Recent Trends in Thermoelectric Materials Research, Part Two*. (Academic Press, 2000).

18. Lee, S. *et al.* Resonant bonding leads to low lattice thermal conductivity. *Nature Communications 2014 5:1* **5**, 1–8 (2014).

19. Morelli, D. T., Jovovic, V. & Heremans, J. P. Intrinsically minimal thermal conductivity in cubic I-V-VI2 semiconductors. *Phys Rev Lett* **101**, 035901 (2008).

20. Liu, W. *et al.* Convergence of Conduction Bands as a Means of Enhancing Thermoelectric Performance of n -Type Mg2Si1−xSnx Solid Solutions. *Phys Rev Lett* **108**, 166601 (2012).

21. Pei, Y., Wang, H., Gibbs, Z. M., LaLonde, A. D. & Snyder, G. J. Thermopower enhancement in Pb1−xMnxTe alloys and its effect on thermoelectric efficiency. *NPG Asia Mater* **4**, e28–e28 (2012).

22. Tang, Y. *et al.* Convergence of multi-valley bands as the electronic origin of high thermoelectric performance in CoSb3 skutterudites. *Nat Mater* **14**, 1223–1228 (2015).

23. Pei, Y. *et al.* Convergence of electronic bands for high performance bulk thermoelectrics. *Nature* **473**, 66–69 (2011).

24. Chen, Y. *et al.* Transport properties and valence band feature of high-performance (GeTe) 85(AgSbTe2) 15thermoelectric materials. *New J Phys* **16**, 013057 (2014).

25. Li, M. *et al.* Ultra-high thermoelectric performance in graphene incorporated Cu2Se: Role of mismatching phonon modes. *Nano Energy* **53**, 993–1002 (2018).

26. Zhong, B. *et al.* High superionic conduction arising from aligned large lamellae and large figure of merit in bulk Cu1.94Al0.02Se. *Appl Phys Lett* **105**, (2014).

27. Zhou, Z. *et al.* Compositing effects for high thermoelectric performance of Cu2Se-based materials. *Nature Communications 2023 14:1* **14**, 1–9 (2023).

28. Brown, D. R. *et al.* Phase transition enhanced thermoelectric figure-of-merit in copper chalcogenides. *APL Mater* **1**, (2013).

29. Yang, D. *et al.* Flexible power generators by Ag2Se thin films with record-high thermoelectric performance. *Nature Communications 2024 15:1* **15**, 1–11 (2024).

30. Zebarjadi, M., Liao, B., Esfarjani, K., Dresselhaus, M. & Chen, G. Enhancing the Thermoelectric Power Factor by Using Invisible Dopants. *Advanced Materials* **25**, 1577–1582 (2013).

31. Ibáñez, M. *et al.* High-performance thermoelectric nanocomposites from nanocrystal building blocks. *Nature Communications 2016 7:1* **7**, 1–7 (2016).

32. Zebarjadi, M. *et al.* Power factor enhancement by modulation doping in bulk nanocomposites. *Nano Lett* **11**, 2225–2230 (2011).

33. Lv, H. Y., Lu, W. J., Shao, D. F. & Sun, Y. P. Enhanced thermoelectric performance of phosphorene by strain-induced band convergence. *Phys Rev B Condens Matter Mater Phys* **90**, 085433 (2014).

34. Lou, X. *et al.* Lattice Strain Leads to High Thermoelectric Performance in Polycrystalline SnSe. *ACS Nano* **15**, 8204–8215 (2021).

35. Wu, Y. *et al.* Lattice Strain Advances Thermoelectrics. *Joule* **3**, 1276–1288 (2019).

36. Biswas, K. *et al.* Strained endotaxial nanostructures with high thermoelectric figure of merit. *Nature Chemistry 2010 3:2* **3**, 160–166 (2011).

37. Biswas, K. *et al.* High-performance bulk thermoelectrics with all-scale hierarchical architectures. *Nature 2012 489:7416* **489**, 414–418 (2012).

38. Poudel, B. *et al.* High-thermoelectric performance of nanostructured bismuth antimony telluride bulk alloys. *Science (1979)* **320**, 634–638 (2008).

39. Liu, H. *et al.* Ultrahigh Thermoelectric Performance by Electron and Phonon Critical Scattering in Cu2Se1-xIx. *Advanced Materials* **25**, 6607–6612 (2013).

40. Nunna, R. *et al.* Ultrahigh thermoelectric performance in Cu2Se-based hybrid materials with highly dispersed molecular CNTs. *Energy Environ Sci* **10**, 1928–1935 (2017).

41. Zhao, L. *et al.* Significant enhancement of figure-of-merit in carbon-reinforced Cu2Se nanocrystalline solids. *Nano Energy* **41**, 164–171 (2017).

42. Zhao, L. D. *et al.* Ultralow thermal conductivity and high thermoelectric figure of merit in SnSe crystals. *Nature 2014 508:7496* **508**, 373–377 (2014).

43. Wei, W. *et al.* Achieving High Thermoelectric Figure of Merit in Polycrystalline SnSe via Introducing Sn Vacancies. *J Am Chem Soc* **140**, 499–505 (2018).

44. Qin, B. *et al.* Realizing High Thermoelectric Performance in p-Type SnSe through Crystal Structure Modification. *J Am Chem Soc* **141**, 1141–1149 (2019).

45. Chang, C. *et al.* 3D charge and 2D phonon transports leading to high out-of-plane ZT in n-type SnSe crystals. *Science (1979)* **360**, 778–783 (2018).

46. Venkatasubramanian, R., Siivola, E., Colpitts, T. & O'Quinn, B. Thin-film thermoelectric devices with high room-temperature figures of merit. *Nature 2001 413:6856* **413**, 597–602 (2001).

47. Chen, Z. *et al.* Lattice Dislocations Enhancing Thermoelectric PbTe in Addition to Band Convergence. *Advanced Materials* **29**, 1606768 (2017).

48. Li, J. *et al.* Low-Symmetry Rhombohedral GeTe Thermoelectrics. *Joule* **2**, 976–987 (2018).

49. Zebarjadi, M. Electronic cooling using thermoelectric devices. *Appl Phys Lett* **106**, (2015).

50. Adams, M. J., Verosky, M., Zebarjadi, M. & Heremans, J. P. Active Peltier Coolers Based on Correlated and Magnon-Drag Metals. *Phys Rev Appl* **11**, 054008 (2019).

51. Foiles, C. L. *Electrical Resistivity, Thermoelectrical Power and Optical Properties*. *Electrical Resistivity, Thermoelectrical Power and Optical Properties* vol. 15b (Springer-Verlag, Berlin/Heidelberg, 1985).

52. Watzman, S. J. *et al.* Magnon-drag thermopower and Nernst coefficient in Fe, Co, and Ni. *Phys Rev B* **94**, 144407 (2016).

53. Garmroudi, F. *et al.* High thermoelectric performance in metallic NiAu alloys via interband scattering. *Sci Adv* **9**, (2023).

54. Selvan, K. V. & Mohamed Ali, M. S. Copper-Nickel and Copper-Cobalt Thermoelectric Generators: Power-Generating Optimization through Structural Geometrics. *IEEE Trans Electron Devices* **65**, 3394–3400 (2018).

55. Mao, J. *et al.* High thermoelectric power factor in Cu–Ni alloy originate from potential barrier scattering of twin boundaries. *Nano Energy* **17**, 279–289 (2015).

56. Wolf, M. *et al.* Cu-Ni-Based Alloys from Nanopowders as Potent Thermoelectric Materials for High-Power Output Applications. *Alloys 2022, Vol. 1, Pages 3-14* **1**, 3–14 (2022).

57. Maeda, T. & Somura, T. Variations of Thermoelectric Power of Ni–Fe Invar Alloys with Temperature and Magnetic Field. *https://doi.org/10.1143/JPSJ.44.148* **44**, 148–153 (2013).

58. Tanji, Y., Moriya, H. & Nakagawa, Y. Anomalous Concentration Dependence of Thermoelectric Power of Fe-Ni (fcc) Alloys at High Temperatures. *J Physical Soc Japan* **45**, 1244–1248 (1978).

59. Giannuzzi, A., Tomaschke, H. & Schröder, K. Absolute thermoelectric power and resistivity of Cr-V and Cr-Mn alloys. *Philosophical Magazine* **21**, 479–493 (1970).

60. Schröder, K., Yessik, M. J. & Baum, N. P. Thermoelectric Power and Electrical Resistance of Chromium-Iron Alloys from 125° to 625°K. *J Appl Phys* **37**, 1019–1021 (1966).

61. Boona, S. R. & Morelli, D. T. Structural, Magnetic, and Thermoelectric Properties of Some CePd3-Based Compounds. *J Electron Mater* **42**, 1592–1596 (2013).

62. Boona, S. R. & Morelli, D. T. Enhanced thermoelectric properties of CePd 3-xPt x. *Appl Phys Lett* **101**, 101909 (2012).

63. van Daal, H. J., van Aken, P. B. & Buschow, K. H. J. The seebeck coefficient of YbAl2 and YbAl3. *Phys Lett A* **49**, 246–248 (1974).

64. Nakanishi, Y. *et al.* Electrical and thermal transport properties of intermediate-valence YbAl3. *J Phys D Appl Phys* **35**, 2183 (2002).

65. Rowe, D. M., Kuznetsov, V. L., Kuznetsova, L. A. & Min, G. Electrical and thermal transport properties of intermediate-valence YbAl3. *J Phys D Appl Phys* **35**, 315 (2002).

66. Pott, R. *et al.* Magnetic Order and Other Phase Transitions in Mixed-Valent YbPd. *Phys Rev Lett* **54**, 481 (1985).

67. Jeong, T. & Kwon, Y. Electronic and magnetic properties of a heavy fermion compound YbPd. *Phys Lett A* **362**, 500–504 (2007).

68. Lee, S. J., Park, J. M., Canfield, P. C. & Lynch, D. W. Optical properties and electronic structures of single crystalline RAl3 (R=Sc, Yb, and Lu). *Phys Rev B* **67**, 075104 (2003).

69. Akira, H. & Akira, Y. Electronic Structure of CePd3. *J Physical Soc Japan* **56**, 3990–3996 (1987).

70. Svetlizky, D. *et al.* Directed energy deposition (DED) additive manufacturing: Physical characteristics, defects, challenges and applications. *Materials Today* **49**, 271–295 (2021).

71. Ahn, D. G. Directed Energy Deposition (DED) Process: State of the Art. *International Journal of Precision Engineering and Manufacturing-Green Technology 2021 8:2* **8**, 703–742 (2021).

72. Lu, K. Sintering of nanoceramics. *International Materials Reviews* **53**, 21–38 (2008).

73. LaLonde, A. D., Ikeda, T. & Snyder, G. J. Rapid consolidation of powdered materials by induction hot pressing. *Review of Scientific Instruments* **82**, 25104 (2011).

74. Ho, C. Y., Bogaard, R. H., Chi, T. C., Havill, T. N. & James, H. M. Thermoelectric power of selected metals and binary alloy systems. *Thermochim Acta* **218**, 29–56 (1993).

75. Leblanc, S., Yee, S. K., Scullin, M. L., Dames, C. & Goodson, K. E. Material and manufacturing cost considerations for thermoelectrics. *Renewable and Sustainable Energy Reviews* vol. 32 313–327 Preprint at https://doi.org/10.1016/j.rser.2013.12.030 (2014).

76. Yazawa, K. & Shakouri, A. Cost-efficiency trade-off and the design of thermoelectric power generators. *Environ Sci Technol* **45**, 7548–7553 (2011).

77. Bahrami, A., Schierning, G. & Nielsch, K. Waste Recycling in Thermoelectric Materials. *Advanced Energy Materials* vol. 10 Preprint at https://doi.org/10.1002/aenm.201904159 (2020).

78. Fan, X. *et al.* Evolution of thermoelectric performance for (Bi,Sb)2Te3 alloys from cutting waste powders to bulks with high figure of merit. *J Solid State Chem* **233**, 186–193 (2016).

79. Vogel, M. *et al.* Low profile heat pipe heat sink and green performance characterization for next generation CPU module thermal designs. in *Annual IEEE Semiconductor Thermal Measurement and Management Symposium* 145–150 (2010). doi:10.1109/STHERM.2010.5444301.

80. Zhang, J., Zhang, T., Prakash, S. & Jaluria, Y. Experimental and numerical study of transient electronic chip cooling by liquid flow in microchannel heat sinks. *Numeri Heat Transf A Appl* **65**, 627–643 (2014).

81. Zebarjadi, M. Heat Management in Thermoelectric Power Generators. *Sci Rep* **6**, (2016).

82. Du, Y. *et al.* Thermoelectric materials and devices fabricated by additive manufacturing. *Vacuum* **178**, 109384 (2020).

83. Gong, G. *et al.* Research status of laser additive manufacturing for metal: a review. *Journal of Materials Research and Technology* **15**, 855–884 (2021).

84. Ahn, D.-G. Directed Energy Deposition (DED) Process: State of the Art. *International Journal of Precision Engineering and Manufacturing-Green Technology* **8**, 703–742 (2021).

85. Jinoop, A., Paul, C. & Bindra, K. Laser-assisted directed energy deposition of nickel super alloys: A review. *Proceedings of the Institution of Mechanical Engineers, Part L: Journal of Materials: Design and Applications* **233**, 2376–2400 (2019).

86. Thompson, S. M., Bian, L., Shamsaei, N. & Yadollahi, A. An overview of Direct Laser Deposition for additive manufacturing; Part I: Transport phenomena, modeling and diagnostics. *Addit Manuf* **8**, 36–62 (2015).

87. Herzog, D., Seyda, V., Wycisk, E. & Emmelmann, C. Additive manufacturing of metals. *Acta Mater* **117**, 371–392 (2016).

88. Savitha, U., Srinivas, V., Reddy, G. J., Gokhale, A. A. & Sundararaman, M. Laser-Based Directed Energy Deposition of Functionally Graded Metal–Ceramic (NiCr–YSZ) System. *Transactions of the Indian National Academy of Engineering* **6**, 1111–1118 (2021).

89. Gibson, I., Rosen, D., Stucker, B. & Khorasani, M. Materials for Additive Manufacturing. in *Additive Manufacturing Technologies* 379–428 (Springer International Publishing, Cham, 2021). doi:10.1007/978-3-030-56127-7_14.

90. Guo, N. & Leu, M. C. Additive manufacturing: technology, applications and research needs. *Frontiers of Mechanical Engineering* **8**, 215–243 (2013).

91. Shamsaei, N., Yadollahi, A., Bian, L. & Thompson, S. M. An overview of Direct Laser Deposition for additive manufacturing; Part II: Mechanical behavior, process parameter optimization and control. *Addit Manuf* **8**, 12–35 (2015).

92. Emmelmann, C., Kranz, J., Herzog, D. & Wycisk, E. Laser Additive Manufacturing of Metals. in 143–162 (2013). doi:10.1007/978-3-642-41341-4_6.

93. Haynes, W. M. *CRC Handbook of Chemistry and Physics*. (CRC press, 2016).

94. Yao, P. *et al.* Fully hardware-implemented memristor convolutional neural network. *Nature 2020 577:7792* **577**, 641–646 (2020).

95. White, G. K. *Thermal Conductivity of Pure Metals and Alloys*. *Thermal Conductivity of Pure Metals and Alloys* vol. 15c (Springer-Verlag, Berlin/Heidelberg, 1991).

96. Rowe, D. M. *CRC Handbook of Thermoelectrics*. (CRC Press, 2018). doi:10.1201/9781420049718.

97. Mao, J. *et al.* High thermoelectric power factor in Cu-Ni alloy originate from potential barrier scattering of twin boundaries. *Nano Energy* **17**, 279–289 (2015).

98. Yang, C. W., Williams, D. B. & Goldstein, J. I. A revision of the Fe-Ni phase diagram at low temperatures (<400 °C). *Journal of Phase Equilibria* **17**, 522–531 (1996).

99. Xiong, W., Zhang, H., Vitos, L. & Selleby, M. Magnetic phase diagram of the Fe–Ni system. *Acta Mater* **59**, 521–530 (2011).

100. Howald, R. A. The thermodynamics of tetrataenite and awaruite: A review of the Fe-Ni phase diagram. *Metall Mater Trans A Phys Metall Mater Sci* **34 A**, 1759–1769 (2003).

101. Komabayashi, T., Hirose, K. & Ohishi, Y. In situ X-ray diffraction measurements of the fcc-hcp phase transition boundary of an Fe-Ni alloy in an internally heated diamond anvil cell. doi:10.1007/s00269-012-0490-3.

102. Xia, C. H., Wang, Y., Wang, J. J., Lu, X. G. & Zhang, L. Thermodynamic assessment of the Co–Fe–Ni system and diffusion study of its fcc phase. *J Alloys Compd* **853**, 157165 (2021).

103. Li, K., Fu, C.-C., Nastar, M. & Soisson, F. Predicting atomic diffusion in concentrated magnetic alloys: The case of paramagnetic Fe-Ni. *Phys Rev B* **107**, 94103 (2023).

104. Cacciamani, G. *et al.* Critical evaluation of the Fe–Ni, Fe–Ti and Fe–Ni–Ti alloy systems. *Intermetallics (Barking)* **14**, 1312–1325 (2006).

105. Ma, D., Wang, Z., Zhao, H., Chen, J. & Ke, F. First-principles study of the stability and electronic structure of Ni–Fe Alloy within three different space groups. *Ferroelectrics* **571**, 175–182 (2021).

106. Bag, P., Su, Y. C., Kuo, Y. K., Lai, Y. C. & Wu, S. K. Physical properties of face-centered cubic structured high-entropy alloys: Effects of NiCo, NiFe, and NiCoFe alloying with Mn, Cr, and Pd. *Phys Rev Mater* **5**, 085003 (2021).

107. Mokrousov, Y., Zhang, H., Freimuth, F., Farrellt, T. & Greig, D. The thermoelectric power of nickel and its alloys. *Journal of Physics C: Solid State Physics* **3**, 138 (1970).

108. Wijn, H. *3d, 4d and 5d Elements, Alloys and Compounds*. vol. 32A (Springer-Verlag, Berlin/Heidelberg, 1997).

109. Hayase, M., Shiga, M. & Nakamura, Y. Spontaneous volume magnetostriction and lattice constant of face-centered cubic Fe-Ni and Ni-Cu alloys. *J Physical Soc Japan* **34**, 925–931 (1973).

110. Sæther, S. *et al.* Phonon thermal transport in copper: The effect of size, crystal orientation, and grain boundaries. *AIP Adv* **12**, 65301 (2022).

111. Gall, D. Electron mean free path in elemental metals. *J Appl Phys* **119**, 85101 (2016).

112. Jain, A. & McGaughey, A. J. H. Thermal transport by phonons and electrons in aluminum, silver, and gold from first principles. *Phys Rev B* **93**, 081206 (2016).

113. Li, S. *et al.* Cost-efficient copper-nickel alloy for active cooling applications. *Int J Heat Mass Transf* **195**, 123181 (2022).

114. Elsukov, E. P. *et al.* Peculiarities of Mechanical Alloying of High-Concentration Fe–Cr Alloys. *Physics of Metals and Metallography* **119**, 153–160 (2018).

115. Zeier, W. G. *et al.* Engineering half-Heusler thermoelectric materials using Zintl chemistry. *Nature Reviews Materials 2016 1:6* **1**, 1–10 (2016).

116. Fu, C. *et al.* Realizing high figure of merit in heavy-band p-type half-Heusler thermoelectric materials. *Nature Communications 2015 6:1* **6**, 1–7 (2015).

117. Poon, G. J. Chapter 2 Electronic and thermoelectric properties of Half-Heusler alloys. *Semiconductors and Semimetals* **70**, 37–75 (2001).

118. Poon, G. J. Chapter 2 Electronic and thermoelectric properties of Half-Heusler alloys. *Semiconductors and Semimetals* **70**, 37–75 (2001).

119. Li, W., Ghosh, S., Liu, N. & Poudel, B. Half-Heusler thermoelectrics: Advances from materials fundamental to device engineering. *Joule* **8**, 1274–1311 (2024).

120. Mitra, M. *et al.* Conventional Half-Heusler alloys advance state-of-the-art thermoelectric properties. *Materials Today Physics* **28**, 100900 (2022).

121. Mott, N. F., Davis, E. A. & Weiser, K. Electronic Processes in Non-Crystalline Materials. *Phys Today* **25**, 55–55 (1972).

122. Zhou, J., Yang, R., Chen, G. & Dresselhaus, M. S. Optimal bandwidth for high efficiency thermoelectrics. *Phys Rev Lett* **107**, 226601 (2011).

123. Jeong, C., Kim, R. & Lundstrom, M. On the Best Bandstructure for Thermoelectric Performance. *J Appl Phys* **111**, 113707 (2011).

124. Mahan, G. D. & Sofo, J. O. The Best Thermoelectric. *Proceedings of the National Academy of Sciences* **93**, 7436–7439 (1996).

125. Laube, E. Strukturen von neuen SE-Verbindungen, 1. Mitt. *Monatsh Chem* **97**, 722–732 (1966).

126. Zhu, Z. & Pelton, A. D. Critical assessment and optimization of phase diagrams and thermodynamic properties of RE–Zn systems – Part II – Y–Zn, Eu–Zn, Gd–Zn, Tb–Zn, Dy–Zn, Ho–Zn, Er–Zn, Tm–Zn, Yb–Zn and Lu–Zn. *J Alloys Compd* **641**, 261–271 (2015).

127. Akbar, F., Čurlík, I., Reiffers, M. & Giovannini, M. Phase equilibria and crystal structures in the ytterbium–copper–zinc system. *J Alloys Compd* **976**, 173195 (2024).

128. Sakamoto, I. *et al.* De Haas-van Alphen effect in ytterbium and uranium compounds. *J Alloys Compd* **275–277**, 505–509 (1998).

129. Topological Materials Database. https://www.topologicalquantumchemistry.com/#/.

130. Bradlyn, B. *et al.* Topological quantum chemistry. *Nature* **547**, 298–305 (2017).

131. Vergniory, M. G. *et al.* All topological bands of all nonmagnetic stoichiometric materials. *Science (1979)* **376**, (2022).

132. Vergniory, M. G. *et al.* A complete catalogue of high-quality topological materials. *Nature* **566**, 480–485 (2019).

133. Giannozzi, P. *et al.* QUANTUM ESPRESSO: a modular and open-source software project for quantum simulations of materials. *J Phys Condens Matter* **21**, 395502 (2009).

134. Perdew, J. P., Burke, K. & Ernzerhof, M. Generalized Gradient Approximation Made Simple. *Phys Rev Lett* **77**, 3865–3868 (1996).

135. Topsakal, M. & Wentzcovitch, R. M. Accurate projected augmented wave (PAW) datasets for rare-earth elements (RE = La–Lu). *Comput Mater Sci* **95**, 263–270 (2014).

136. Madsen, G. K. H. & Singh, D. J. BoltzTraP. A code for calculating band-structure dependent quantities. *Comput Phys Commun* **175**, 67–71 (2006).

137. Ferhat, M. & Nagao, J. Thermoelectric and transport properties of β-Ag2Se compounds. *J Appl Phys* **88**, 813–816 (2000).

138. Day, T. *et al.* Evaluating the potential for high thermoelectric efficiency of silver selenide. *J Mater Chem C Mater* **1**, 7568–7573 (2013).

139. Xiao, C. *et al.* Superionic phase transition in silver chalcogenide nanocrystals realizing optimized thermoelectric performance. *J Am Chem Soc* **134**, 4287–4293 (2012).

140. Jood, P., Chetty, R. & Ohta, M. Structural stability enables high thermoelectric performance in room temperature Ag 2 Se. *J Mater Chem A Mater* **8**, 13024–13037 (2020).

141. Lee, C., Park, Y. H. & Hashimoto, H. Effect of nonstoichiometry on the thermoelectric properties of a Ag 2Se alloy prepared by a mechanical alloying process. *J Appl Phys* **101**, (2007).